Droplet Interface Bilayers for the Study of Membrane Proteins

William L. Hwang

MASTER OF SCIENCE BY RESEARCH

Subject: Chemistry

University of Oxford
St. John's College

May 2008

Dedication

To Katie N. Lee, the love of my life, and to my parents, Phillip Q. Hwang and Yuan-Yuan L. Hwang, for their unwavering love and support.

Declaration

The work described in this thesis was carried out in the Chemistry Research Laboratory at the University of Oxford between October 2006 and May 2008 in the laboratory of Professor Hagan Bayley. All of the work described within this thesis is my own unless otherwise stated in the text. This work has not been submitted previously for any other degree at the University of Oxford or any other university.

William L. Hwang

May 2008

Acknowledgments

I am grateful to Professor Hagan Bayley for taking me into his lab and providing me with the encouragement and guidance I needed to succeed. I am thankful to Dr. Matthew A. Holden for being a wonderful mentor and friend. He was always willing to help me whenever I needed assistance. I am indebted to Dr. Amy Mason, Dr. Steven Cheley, Qiuhong Li, and Ellina Mikhailova for lending me their biochemical expertise and producing many of the proteins I used in my research. The interdisciplinary nature of my work enabled me to collaborate with numerous scientists, which was a terrific learning experience. These collaborations were as follows: Chapter 2 – Dr. Steven White of Oxford Nanolabs, Chapter 3 – Dr. Min Chen and Dr. Bríd Cronin, and Chapter 5 – Dr. Dvir Rotem, Dr. Haichen Wu, Dr. Giovanni Maglia, and Dr. Andrew Heron. I appreciate all of the members of the Hagan Bayley and Mark Wallace groups for their friendship and making my experience in Oxford a wonderful one that I will always look back on fondly.

This work was funded by a Royal Society-Wolfson Research Merit Award, the Medical Research Council, and the National Institutes of Health. I want to thank the Rhodes Trust for giving me the opportunity to study in Oxford and supporting me during my tenure here. I am particularly thankful to Sir Colin Lucas, Catherine King, Mary Eaton, Sheila Partridge, Gosha Daroch, Martin Gubb, Bob Wyllie, Colin Page, John Gee, Neil

Wigfield, and Neil Sumner of the Rhodes House for working hard to ensure that my time in Oxford was productive and enjoyable. I also want to thank St. John's College for allowing me to join their vibrant community of scholars.

I am grateful to my parents, Phillip Q. Hwang and Yuan-Yuan L. Hwang, for being the best parents in the world. Their nurturing instilled in me a strong sense of what it means to be part of a global community and the impact that one person can make. I would like to thank all of my teachers and mentors, past and present, without whom I would not have the opportunities I have today. And last but not least, this work was only possible because of the patience of my fiancée, Katie N. Lee, who spent countless late nights in the lab with me.

Abbreviations

α	steady-state net current through double DIB network when one blocker is bound to a pore in bilayer B
α'	steady-state net current through double DIB network when no blockers are bound to pores in bilayer B
α''	steady-state net current through double DIB network when an additional pore inserts
αHL	wild-type α-hemolysin
β	initial current deviation from α immediately after a binding event
β'	initial current deviation from α' immediately after an dissociation event
β''	initial current deviation from α'' immediately after a pore insertion
C_A	capacitance of bilayer A
C_B	capacitance of bilayer B
DDAB	dimethyldioctadecylammonium bromide
DIB	droplet interface bilayer
DPhPC	1,2-diphytanoyl-*sn*-glycero-3-phosphocholine
DPPG	1,2-dipalmitoyl-*sn*-glycero-3-[phospho-*rac*-(1-glycerol)] (sodium salt)
γ	inverse of exponential decay time constant for binding event
γ'	inverse of exponential decay time constant for dissociation event
γ''	inverse of exponential decay time constant for pore insertion event
$I_{block}(t)$	net current through double DIB network as a function of time immediately following binding of blocker
$I_{unblock}(t)$	net current through double DIB network as a function of time immediately following dissociation of blocker
$I_{insert}(t)$	net current through double DIB network as a function of time immediately following insertion of a pore
IVTT	*in vitro* transcription and translation
Kcv	potassium channel from chlorella virus PBCV-1
MM	Montal-Mueller
OmpG	outer membrane protein G from *E. coli*
R	resistance of single αHL pore; value depends on orientation of pore
R^*	additional resistance provided by a single blocker molecule when it binds to an αHL pore in bilayer B

R_A	net resistance of bilayer A
R_A^-	net resistance of bilayer A prior to insertion of one additional pore
R_B^-	net resistance of bilayer B except the one pore that interacts with the blocker
R_B	net resistance of bilayer B with no pores blocked
R_B^*	net resistance of bilayer B with one pore blocked
SPICE	simulation program with integrated circuit emphasis
TRIMEB	heptakis(2,3,6-tri-O-methyl)-β-cyclodextrin
V(t)	electrical potential of middle droplet in double DIB network as a function of time
V_{cc}	electrical potential applied to the double DIB network

Abstract

Aqueous droplets submerged in an oil-lipid mixture become enclosed by a lipid monolayer. The droplets can be connected to form robust networks of droplet interface bilayers (DIBs) with functions such as a biobattery and a light sensor. The discovery and characterization of an engineered nanopore with diode-like properties is enabling the construction of DIB networks capable of biochemical computing. Moreover, DIB networks might be used as model systems for the study of membrane-based biological phenomena. We develop and experimentally validate an electrical modeling approach for DIB networks. Electrical circuit simulations will be important in guiding the development of increasingly complex DIB networks.

In cell membranes, the lipid compositions of the inner and outer leaflets differ. Therefore, a robust model system that enables single-channel electrical recording with asymmetric bilayers would be very useful. Towards this end, we incorporate lipid vesicles of different compositions into aqueous droplets and immerse them in an oil bath to form asymmetric DIBs (a-DIBs). Both α-helical and β-barrel membrane proteins insert readily into a-DIBs, and their activity can be measured by single-channel electrical recording. We show that the gating behavior of outer membrane protein G (OmpG) from *Escherichia coli* differs depending on the side of insertion in an asymmetric DIB

with a positively charged leaflet opposing a negatively charged leaflet. The a-DIB system provides a general platform for studying the effects of bilayer leaflet composition on the behavior of ion channels and pores.

Even with the small volumes (~100 nL) that can be used to form DIBs, the separation between two adjacent bilayers in a DIB network is typically still hundreds of microns. In contrast, dual-membrane spanning proteins require the bilayer separation to be much smaller; for example, the bilayer separation for gap junctions must be less than 5 nm. We designed a double bilayer system that consists of two monolayer-coated aqueous spheres brought into contact with each side of a water film submerged in an oil-lipid solution. The spheres could be brought close enough together such that they physically deflected without rupturing the double bilayer. Future work on quantifying the bilayer separation and studying dual-membrane spanning proteins with the double bilayer platform is planned.

Contents

Chapter 1

Introduction[1]

The lipid bilayers that compose cell membranes are relatively impermeable to ions. Thus, ion transport across membranes is mediated by membrane proteins such as ion channels. Ion channels are found in the membranes of all bacterial, plant, and animal cells and are critical in biological processes ranging from the regulation of blood pressure to nerve and muscle excitation (Ashcroft, 2000). It is therefore not surprising that defects in ion channels can have profound physiological consequences, leading to a vast array of diseases, including cystic fibrosis and cardiac arrhythmias. Furthermore, many therapeutic drugs mediate their effects by interacting with ion channels and the basis for deleterious drug side effects frequently involve inadvertent blockade of ion channels such as the hERG (human *ether-a-go-go*-related gene) K^+ channel (Sanguinetti & Tristani-Firouzi, 2006).

There is tremendous interest in the biomedical and pharmaceutical communities for high-throughput *in vitro* methods of studying and screening ion channels (Gonzalez

[1] A recent review of droplet interface bilayer technologies: BAYLEY, H., CRONIN, B., HERON, A. J., HOLDEN, M. A., HWANG, W. L., SYEDA, R., THOMPSON, J. R. & WALLACE, M. I. (2008). Droplet interface bilayers. In prep.

et al., 1999). The reconstitution of channels into Montal-Mueller (MM) planar bilayers separating two aqueous compartments is one of the most common techniques for electrophysiological study of ion channels at the single-channel level (Fig. 1.1) (Ashley, 1995; Miller, 1986; Montal & Mueller, 1972). However, planar bilayers are delicate, cumbersome to work with, and have a relatively short lifetime, which hinders progress in this area.

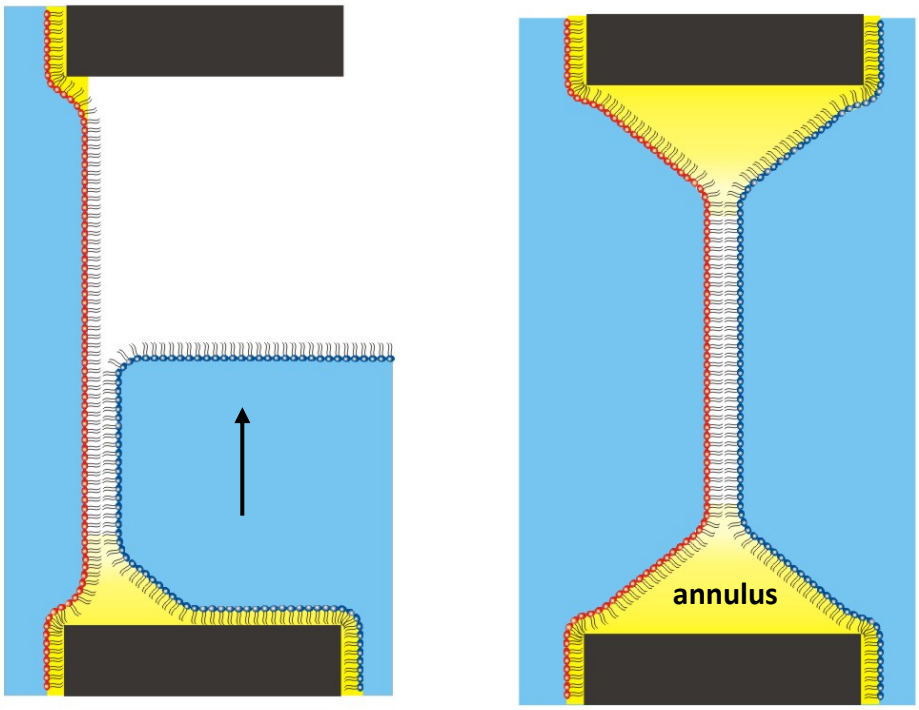

Figure 1.1 Planar Bilayer Formation across an Aperture. Diagrams illustrate the cross-section of an aperture in Teflon™ separating two aqueous compartments. Lipids in pentane are spread at the air/water interface on each side to form two Langmuir-Blodgett monolayers. A complete membrane is formed across the aperture when the monolayers are raised sequentially. Courtesy of Dr. Matthew Holden.

An alternative to the planar bilayer method has recently been developed: our lab and others have shown that a lipid bilayer will spontaneously form at the interface between lipid monolayer-coated aqueous droplets in an oil-lipid solution (Funakoshi et al., 2006; Holden et al., 2007; Hwang et al., 2007). In this technique, two aqueous droplets are submerged in an oil-lipid mixture (Fig. 1.2 *A*). After the droplets become

encased by lipid monolayers, they are brought into contact to form a droplet interface bilayer (DIB; Fig. 1.2 *A*). Linear and branched chains of droplets can be arranged to form large DIB networks (Fig. 1.2 *B*). The incorporation of ion channels and pores into DIBs enables measurement of ion currents through one or more interfaces via electrodes inserted into the droplets. In our experience, the electrical properties of channels and pores in planar bilayers and DIBs are indistinguishable, but a careful check of this should be made whenever a new protein is used in the DIB platform (Bayley et al., 2008). Functional networks are created through the inclusion of membrane proteins with specific properties. For example, a three-droplet "bio-battery" network can be designed by coupling an ionic gradient with α-hemolysin (αHL) pores engineered to be moderately anion-selective (Holden et al., 2007). Bacteriorhodopsin, a light-activated proton pump, can be incorporated into the membranes of DIB networks to create light-sensitive devices.

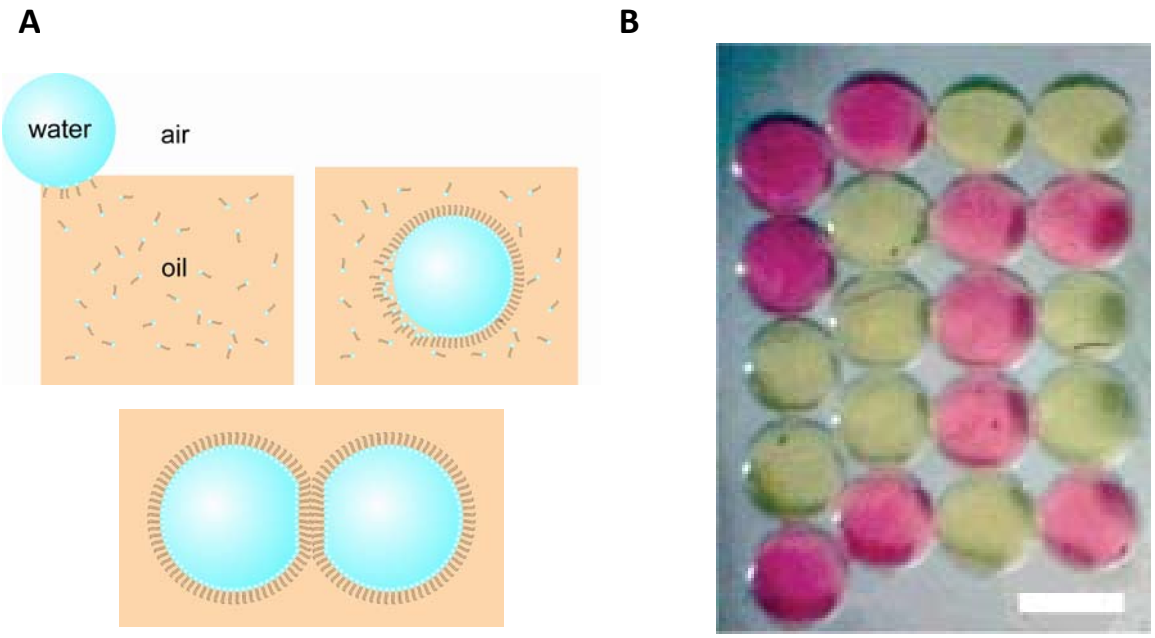

Figure 1.2 Droplet Interface Bilayer Formation. *(A)* Aqueous droplets are deposited into an oil-lipid solution (e.g., phosphocholines in hexadecane). A monolayer will spontaneously assemble at the oil-water interface. Lipid monolayer-coated droplets are brought together to form a droplet interface bilayer. *(B)* Twenty-droplet (200 nL) DIB network arranged on a Perspex surface submerged in 10 mM 1,2-

diphytanoyl-*sn*-glycero-3-phosphocholine in hexadecane. Pink droplets contain 0.6 μM tetramethylrhodamine and yellow droplets contain 0.2 μM Alexa488 linked to dextran in 10 mM MOPS, 1 M KCl, pH 7.0 buffer. There is a bilayer at every droplet-droplet interface. Scale bar is 700 μm. Courtesy of Dr. Matthew Holden.

DIBs can be separated and reformed multiple times by disconnecting and reconnecting droplets. In fact, a single droplet containing a membrane protein of interest can be scanned along a series of droplets containing various analytes as a low volume, rapid screening approach for membrane proteins without cross-contamination (Holden et al., 2007). We have recently demonstrated the ability to perform *in vitro* transcription and translation inside droplets, which enables simultaneous expression and screening of ion channels in droplet interface bilayers (Syeda et al., 2008) and obviates the need for tedious protein purification. Furthermore, the properties of a DIB network can be altered by excising and replacing individual droplets with droplets of different compositions.

Droplet interface bilayers (DIBs) are stable for days to weeks even with a constant applied potential and exhibit much greater mechanical stability relative to planar bilayers (Holden et al., 2007; Hwang et al., 2008; Hwang et al., 2007). In addition, DIBs, like planar bilayers, can withstand applied potentials of greater than 150 mV. Although the physical basis for this stability has yet to be precisely determined, one significant difference between DIBs and MM planar bilayers lies in the interfacial tension along the bilayers. The net interfacial tension along the plane of a MM bilayer can be described by

$$\gamma_{MM} = \gamma_{\phi} + \gamma_{\theta} \tag{1.1}$$

where ϕ is the contact angle between the bilayer and annulus, θ is the contact angle between the annulus and supporting aperture, γ_{ϕ} is the bilayer-annulus interfacial

tension component, and γ_θ is the annulus-support interfacial tension component (Fig. 1.3) (White, 1972).

On the other hand, since DIBs lack an annulus-supporting aperture region (θ), the interfacial tension is reduced to

$$\gamma_{DIB} = \gamma_\phi \tag{1.2}$$

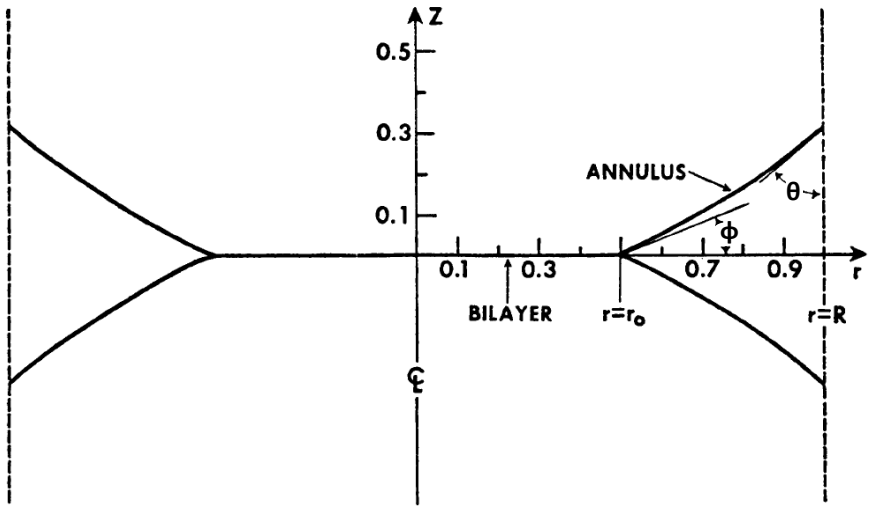

Figure 1.3 Cross-sectional View of Planar Bilayer for Interfacial Tension Analysis. Important parameters are illustrated and the dashed lines demarcate the aperture boundaries. ϕ and θ are the contact angles between the bilayer/annulus and annulus/aperture respectively. For DIBs, θ is not relevant. Adapted from (White, 1972).

In Chapter 2, we characterize the electrical behavior of droplet interface bilayer networks with experimental analysis and modeling. In Chapter 3, we develop a new technique to form asymmetric droplet interface bilayers and demonstrate the potential of this method to investigate the behavior of pores and channels in asymmetric bilayers. In Chapter 4, we develop a technique to create two droplet interface bilayers in close proximity, which may enable the study of dual-membrane spanning proteins such as gap junctions. In Chapter 5, we demonstrate how nanopores and DIB networks can be exploited for molecular logic and computing applications.

Chapter 2

Electrical Behavior of Droplet Interface Bilayer Networks[2]

2.1. Introduction

Droplets in a droplet interface bilayer (DIB) network can act as artificial "protocells" that communicate through bilayer-incorporated proteins. Artificial protocells have been designed to perform biological functions ranging from gene transcription (Fischer et al., 2002; Luisi et al., 2006; Noireaux et al., 2005) and protein synthesis (Pietrini & Luisi, 2004) to energy production and storage (Bennett et al., 2002; Bhosale et al., 2006; Luo et al., 2005). Functional networks assembled from such protocells show promise as a platform for modeling and studying membrane-based phenomena in biological systems. However, further study on the electrical properties of such networks is needed.

[2] Adapted from HWANG, W. L., HOLDEN, M. A., WHITE, S. & BAYLEY, H. (2007). Electrical behavior of droplet interface bilayer networks: experimental analysis and modeling. Journal of the American Chemical Society, 129, 11854-11864.

In this chapter, we investigate DIB networks containing the wild-type α-hemolysin (αHL), a heptameric, 14-strand β-barrel, transmembrane pore from *Staphylococcus aureus* (Song et al., 1996). αHL inserts efficiently into DIBs (Holden et al., 2007; Hwang et al., 2007), is well-characterized (Song et al., 1996), and can be engineered to have diverse functions (Bayley & Jayasinghe, 2004). Moreover, αHL pores adopt a known orientation in a bilayer (Gouaux, 1998), which means that the location of protein domains can be controlled by the arrangement of droplets. We show that DIB networks exhibit electrical phenomena that are not observed in single bilayers, which need further exploration. As the complexity of DIB networks increases, understanding and predicting their electrical behavior becomes more difficult. Thus, progress in the development of biologically relevant DIB networks requires a method to model and simulate their electrical properties. Such models can help explain and predict the behavior of DIB networks, as well as guide further experimentation.

The elements of a DIB network can be considered to be components of an electrical circuit in which bilayers serve as capacitors and incorporated αHL pores serve as resistors. We apply this modeling technique to thoroughly investigate a simple three-droplet network. Experimental measurements, theoretical analysis, and electrical circuit simulations of the current through the three-droplet network are in agreement, which validates our electrical circuit models. The intrinsic modularity and scalability of DIB networks should enable straightforward extension of the analysis presented in this chapter to larger and more complex networks.

2.2. Results and Discussion

2.2.1. Droplet Interface Bilayer Networks

The experimental platform used to create droplet interface bilayer (DIB) networks consists of a Perspex chamber micromachined with an array of divots on the bottom surface (Fig. 2.1). The chamber was filled with 10 mM 1,2-diphytanoyl-*sn*-glycero-3-phosphocholine in hexadecane. Aqueous droplets (200 nL) were submerged in the oil-lipid mixture and encased with lipid monolayers prior to network assembly (Fig. 2.1). Electrodes were inserted into selected network droplets and connected to a patch-clamp amplifier to enable electrical measurements.

The construction of complex DIB networks that last for several days is simple and repeatable. For example, we created a twenty-six droplet "O-U" network in which all DIBs are interconnected by αHL pores (Fig. 2.2 *A*). The electrical behavior of the network can be monitored by inserting Ag/AgCl electrodes into any two droplets (Fig. 2.2 *A* and *B*). It is possible to move the measurement electrodes to different parts of a network, allowing a complex network to be probed in sections or as a whole.

The behavior of DIB networks can be modified by extracting and inserting droplets of different compositions. For example, when the droplet between the "O" and "U" was replaced with a droplet containing both αHL and a reversible pore blocker, heptakis(2,3,6-tri-O-methyl)-β-cyclodextrin (TRIMEB; Fig. 2.2 *C*), blocking events in the current trace are evident (Fig. 2.2 *D*).

When TRIMEB binds to or dissociates from an αHL pore in a single membrane system (Fig. 2.3 *A*), the current change is instantaneous because the voltage across the bilayer is constant (Fig. 2.3 *B*). This is manifested in the current trace as a square step. Moreover, all current blockade events have the same magnitude and shape.

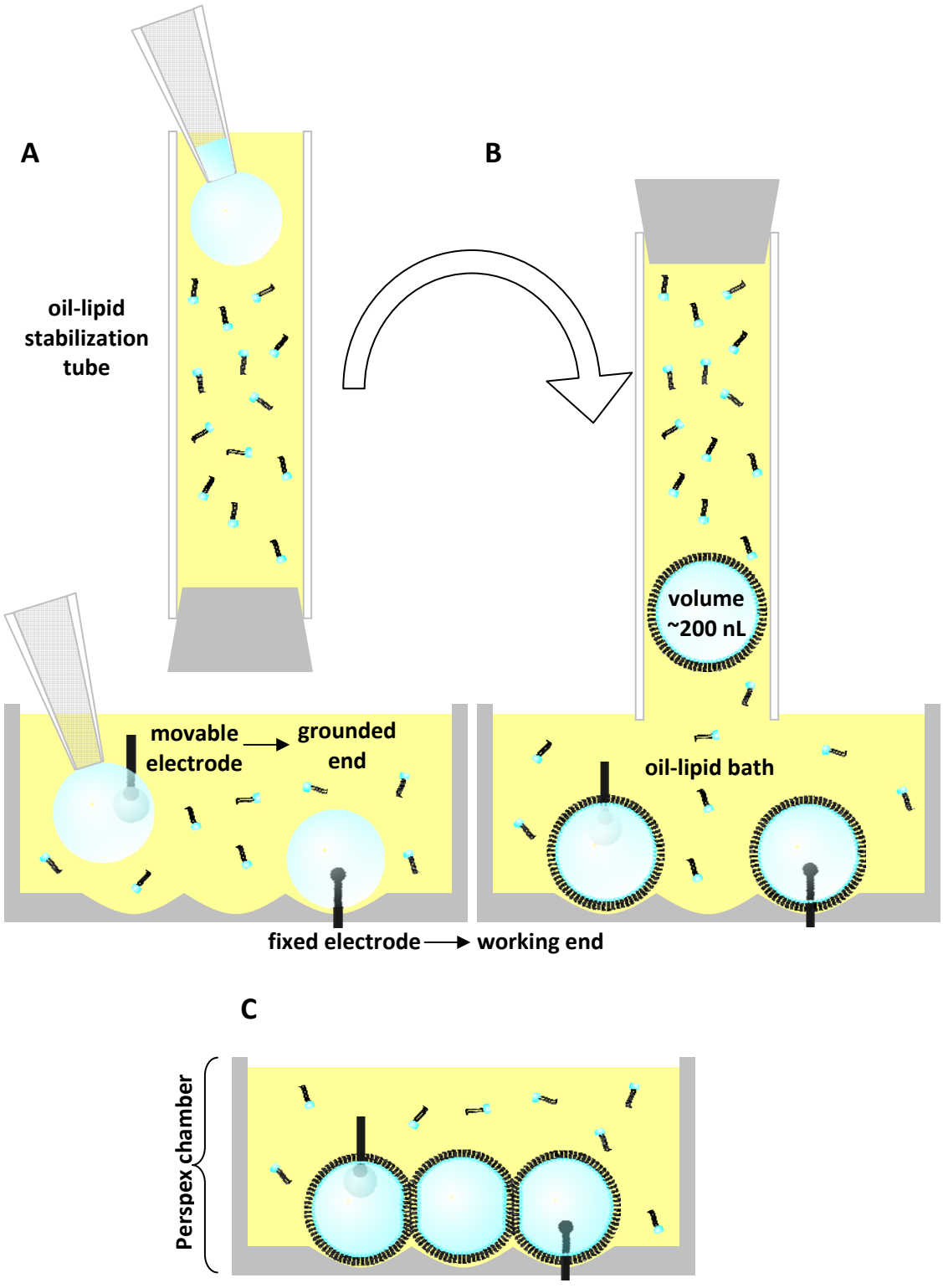

Figure 2.1 Construction of Droplet Interface Bilayer Networks. Schematic is not to scale. (*A*) A Perspex chamber (10 x 10 x 4 mm) was micromachined to include an array of 1 mm diameter divots on the bottom surface with 700 µm center-to-center spacing. The tips of the Ag/AgCl electrodes were coated with 5% w/v low melt agarose. Droplets (200 nL) were directly attached to electrodes with a hand-held pipette and became coated with lipid monolayers after incubation in the oil-lipid bath for thirty minutes. Free droplets were pipetted into an oil-lipid stabilization tube (20 cm section of 1.59 mm I.D. tubing) and coated with a lipid monolayer by allowing the droplets to make several passes along the length of the tube. (*B*) Free droplets were deposited by submerging the end of the oil-lipid stabilization tube in the oil-lipid bath. (*C*) A pipette tip was used to move free droplets into position to form bilayers with other droplets.

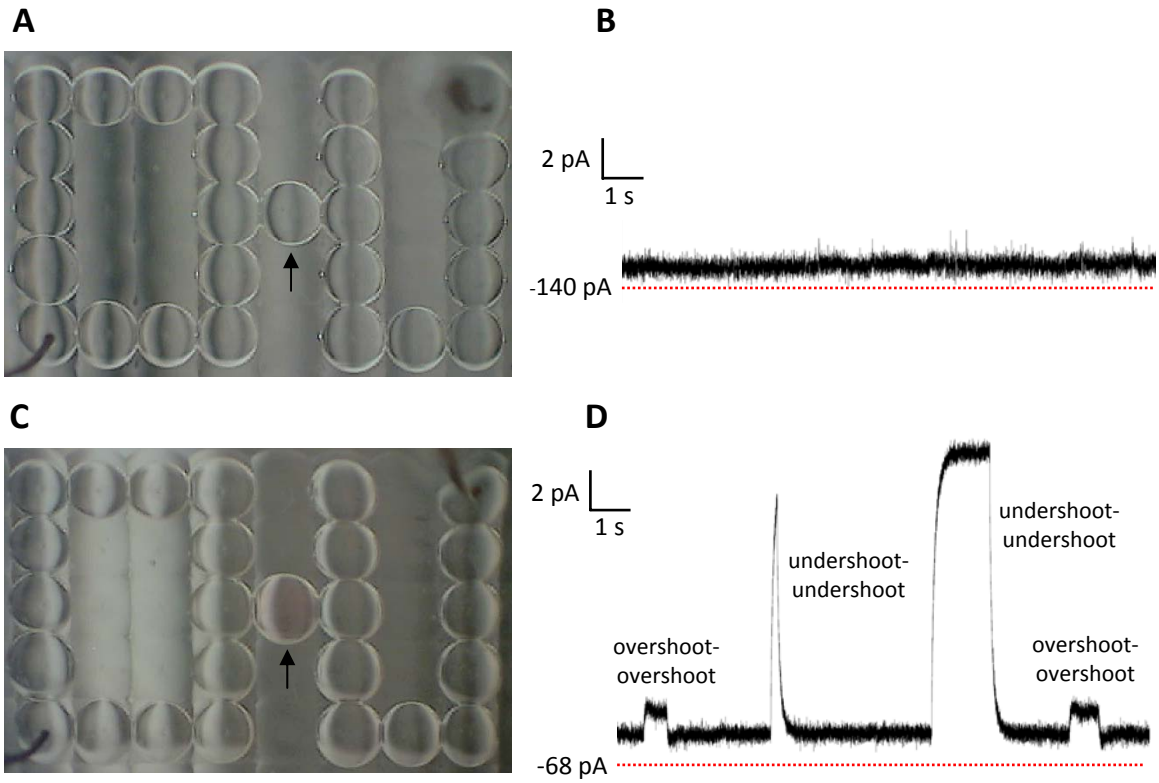

Figure 2.2 "O-U" Droplet Interface Bilayer Network. (*A*) Twenty-six droplet DIB network in the form of an "O-U." Each 200 nL droplet contains 120 ng/mL αHL heptamer in buffer (10 mM MOPS, 1 M KCl, pH 7.0). Pores were incorporated into the bilayers at each droplet interface. Two Ag/AgCl electrodes connected to micromanipulators are inserted into droplets on the bottom left and top right corners of the network and wired to the patch-clamp amplifier to enable electrical recordings. Removal and insertion of these electrodes into other droplets is straightforward. (*B*) Current trace with an applied potential of -50 mV shortly after network formation. No blocking events are observed as expected. (*C*) A central droplet (arrow) is removed and replaced with a 200 nL droplet containing 55 ng/mL αHL heptamer, 23 μM TRIMEB, and a small amount of tetramethylrhodamine (pink) in buffer. (*D*) Current trace with an applied potential of -50 mV shortly after the central droplet was replaced. Distinct types of blocking events are clearly observed: smaller blocking events that exhibit an "overshoot" of steady-state currents upon TRIMEB binding and dissociation (overshoot-overshoot) and larger blocking events that exhibit an "undershoot" of steady-state currents upon TRIMEB binding and dissociation (undershoot-undershoot).

In contrast, when TRIMEB binds or dissociates from an αHL pore in networks of two or more bilayers, the overall network current does not change to its new steady-state value instantaneously because the constant applied voltage is gradually redistributed among the bilayers in the network (Fig. 2.2 *D*). Furthermore, although the binding and dissociation of a TRIMEB molecule with an αHL pore is always the same physically and chemically, the effect on the network current depends on several factors, including bilayer areas, and pore location, quantity, distribution, and orientation. For

example, when the central droplet of the "O-U" network contained TRIMEB (Fig. 2.2 *C*), the resulting current trace exhibited two types of blocking events (Fig. 2.2 *D*): (1) small amplitude events that exhibit an "overshoot" of the new steady-state currents when TRIMEB binds and dissociates from a pore, which we term "overshoot binding-overshoot dissociation," or "overshoot-overshoot" blocking events, and (2) large amplitude events that exhibit an "undershoot" of the new steady-state currents when TRIMEB binds and dissociates from a pore, which we term "undershoot binding-undershoot dissociation," or "undershoot-undershoot" blocking events.

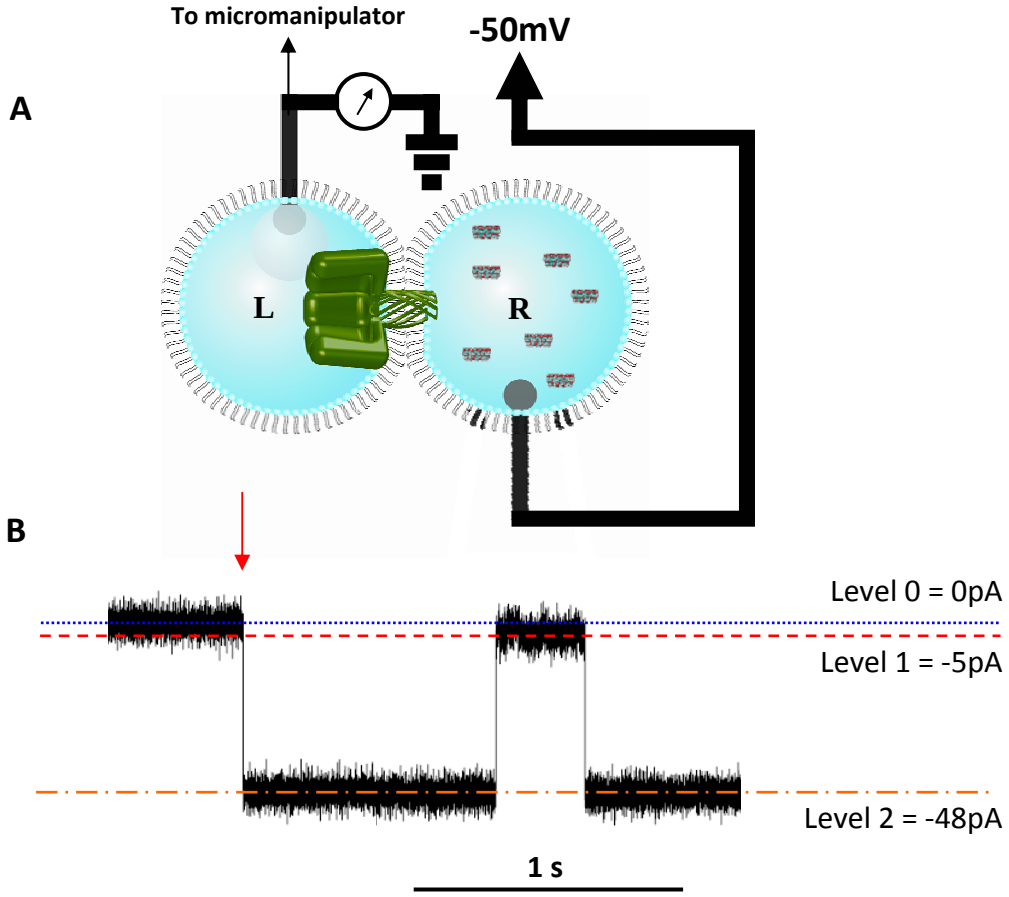

Figure 2.3 Single DIB Experiments and Analysis. (*A*) Setup for single DIB experiment. Droplet L contains 1.7 ng/mL αHL heptamer and the right droplet contains 10 µM TRIMEB, both dissolved in buffer (10 mM MOPS, 1 M KCl, pH 7.0). The left droplet is attached to an agarose ball on the tip of an Ag/AgCl electrode, which is in turn connected to a micromanipulator. The right droplet is attached to a surface Ag/AgCl electrode. The potential is applied to Droplet R and Droplet L is grounded. The pores insert with their cap domain in the L droplet and the β-barrel in the bilayer. (*B*) Experimental current trace of a single αHL pore in a DIB with an applied potential of -50 mV. The arrow indicates the insertion of the pore. One non-covalent blocking event by TRIMEB is shown. Levels 1 and 2 indicate the states in which the pore is partially blocked by TRIMEB and the unblocked pore, respectively.

Insights into the basis of DIB network behavior can be obtained from electrical circuit modeling. To demonstrate and validate our modeling approach, we compare experimental observations, electrical circuit simulation, and theoretical analysis of a simple three-droplet, double DIB network (Fig. 2.4 *A*) that can be viewed as a modular component of a more complex network (Fig. 2.2). The simulation methods demonstrated can be applied to study other DIB networks as well.

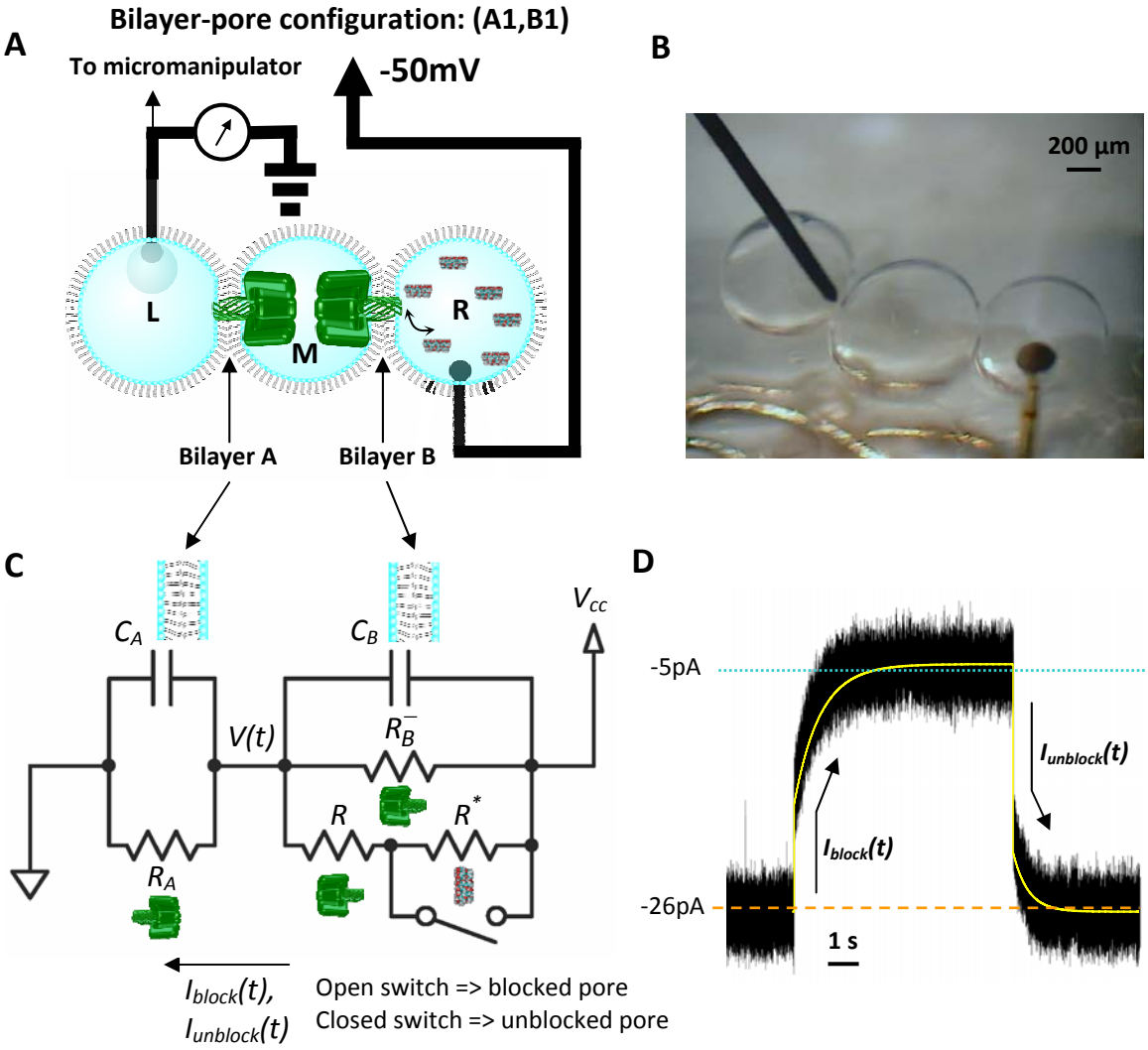

Figure 2.4 Double DIB Experiments and Analysis. (*A*) Setup for double DIB experiment. Droplet L contains buffer (10 mM MOPS, 1 M KCl, pH 7.0), M contains 1.7 ng/mL αHL heptamer in buffer, and R contains 10 µM TRIMEB in buffer. The potential is applied to Droplet R and Droplet L is grounded. The current is measured from Droplet R to Droplet L. The pores insert into the two membranes with opposing orientations as shown. The bilayer-pore configuration illustrated is denoted (A1,B1). (*B*) Image of double DIB experimental setup with one moveable electrode and one fixed electrode. (*C*) Circuit schematic of double DIB system for analysis of blocking events in any bilayer-pore configuration. We assume that only one pore in bilayer B is blocked at a time. C_A is the capacitance and R_A is the net resistance of bilayer A (all

pores in bilayer A combined). C_B is the capacitance of bilayer B, R_B^- is the net resistance of bilayer B excluding one pore (all pores in bilayer B combined except one that interacts with blocker), R represents a single pore in bilayer B that interacts with the blocker, and R^* represents the blocker that interacts with pore R. Opening the switch simulates the binding of the blocker to the pore, and closing the switch simulates the dissociation of the blocker from the pore. If there is only one pore in bilayer B, we simply set R_B^- to an infinite resistance. (*D*) Experimental current trace of a TRIMEB transient blocking event when the double DIB network is in bilayer-pore configuration (A1,B1). The applied voltage is -50 mV. Overlaid plot of theoretical current vs. time (i.e., $I_{block}(t)$ and $I_{unblock}(t)$) during a TRIMEB blocking event for bilayer-pore configuration (A1,B1). The following parameter values are assigned (see text for details): R_A = 0.9 GΩ, R = 1 GΩ, R_B^- = ∞ (open), R^* = 9 GΩ, C_A = 350 pF, and C_B = 500 pF.

2.2.2. Double DIB Network Experiments

We constructed a double DIB network with the L-droplet containing buffer (10 mM MOPS, 1 M KCl, pH 7.0), the M-droplet containing 1.7 ng/mL αHL heptamer in buffer, and the R-droplet containing 10 µM TRIMEB in buffer (Fig. 2.4 *A* and *B*). The notation (A*n*,B*m*) denotes the bilayer-pore configuration, where *n* and *m* are the number of αHL pores in bilayer A (L-M) and bilayer B (M-R), respectively (Fig. 2.4 *A*). For example, the bilayer-pore configuration (A3,B4) indicates that there are three pores in bilayer A and four pores in bilayer B.

Double DIB experiments (n > 25) were conducted with -50 mV applied to droplet R and droplet L grounded, which yielded negative current from droplet R to droplet L (Fig. 2.4 *A*). Unlike experiments with a single bilayer (Fig. 2.3) (Holden & Bayley, 2005; Holden et al., 2006), the current traces of blocking events in the double DIB network exhibit curvature (Fig. 2.4 *D*).

2.2.3. Net Current during Blocking Events in the Double DIB Network

In our experiments, current was observed only after there was at least one pore in each membrane: (A1,B1). This bilayer-pore configuration was easily recognized because it exhibits approximately half the current expected through a single pore. When TRIMEB binds to a single pore in bilayer B of the double DIB network in (A1,B1), there is

an initial drop in current, followed by exponential decay towards the blocked steady-state current level (Fig. 2.4 *D*). TRIMEB dissociation is characterized by a sudden increase in current, followed by exponential decay towards the unblocked steady-state current level. We later describe a method for determining more complex bilayer-pore configurations in the section entitled "Spatial and Temporal Localization of Pore Insertions."

The analytical results that follow can be generalized to any blocker by modifying the blocker resistance in the model. The current through one αHL pore in a single-bilayer, two-droplet system at a voltage of -50 mV applied from β barrel to cap domain was -48 pA (1 M KCl; Fig. 2.3 *B*), which is comparable to previous work (Holden & Bayley, 2005; Holden et al., 2006). The reversible TRIMEB binding reduced the pore current by ~90% (Fig. 2.3 *B*). Based on this behavior, we create an electrical model in which each αHL pore is a resistor in parallel with a capacitor representing the bilayer (Fig. 2.4 *C*). The approximate resistance of a single αHL pore is (-50 mV)/(-48 pA) ≈ 1 GΩ (Fig. 2.3 *B*). The blocker is modeled as a resistor in series with αHL and the reversible binding is represented by a switch (Fig. 2.4 *C*). Since TRIMEB blocks ~90% of the current through αHL, we assign the blocker-pore complex a net resistance of 10 GΩ (i.e., pore: 1 GΩ, blocker: 9 GΩ). The capacitance of typical DIBs was ~300 pF and could be reliably tuned between 150 and 600 pF by moving the droplets away from each other or pushing them closer together by adjusting the movable electrode(s). This observation is consistent with previously reported capacitance values for lipid bilayers (Fettipla et al., 1971; Montal & Mueller, 1972) on the order of 10 fF/μm^2. The resistance of bilayers without inserted pores is on the order of 1 TΩ and can therefore be omitted from the model.

Since only droplet M contains protein (Fig. 2.4 *A*), and αHL pores insert into membranes with their β-barrel domain (Valeva et al., 1997), the cap domains of proteins inserting into both bilayers will remain in droplet M. Thus, the αHL pores in bilayers A and B will have opposing orientations. Using 1 M KCl, 10 mM MOPS, pH 7.0, we found that $I_{+50mV}/I_{-50mV} \approx 1.1$, which is comparable to previous results under similar conditions (Miles et al., 2001). In other words, αHL conducts ~1.1 times more current at 50 mV applied potential when the current moves in the direction of β barrel to cap domain relative to the opposite polarity. Thus, to account for the rectification properties of αHL, we assign pores in bilayer A, $R_{bilayer\,A} = \frac{50\text{mV}}{(1.1 \times 48\text{pA})} \approx 0.9 G\Omega$, and pores in bilayer B, $R_{bilayer\,B} = \frac{-50\text{mV}}{-48\text{pA}} \approx 1 G\Omega$.

We derive analytical expressions for $I_{block}(t)$ and $I_{unblock}(t)$, the net current through the network as a function of time following binding and dissociation events, respectively (Fig. 2.4 *C*). We define the following electrical model parameters such that the analysis applies to any bilayer-pore configuration (Fig. 2.4 *C*). C_A and C_B represent bilayers A and B, respectively. V_{cc} is the applied voltage. All of the pores in bilayer A are combined into an equivalent resistor, R_A, which represents the net resistance of bilayer A (Fig. 2.4 *C*). Since a relatively low blocker concentration of 10 μM was used, we assume for simplicity that only one pore in bilayer B can be blocked at any given time. All of the pores in bilayer B except the one pore that interacts with the blocker is combined into equivalent resistor R_B^- (Fig. 2 *C*). *R* represents the single pore that interacts with the blocker molecules and R^* represents a single blocker molecule that binds to *R*. In reality, different pores in bilayer B are blocked at different times, but from a modeling

perspective, this is not an issue because the resistances of all pores in bilayer B are assumed to be the same. Opening the switch simulates a blocker binding event whereas closing the switch simulates a blocker dissociation event (Fig. 2.4 *C*).

Let

R_B = net resistance of bilayer B with all pores unblocked

R_B^* = net resistance of bilayer B with one pore blocked

$$R_B = R_B^- \,||\, R = \frac{RR_B^-}{R + R_B^-} \qquad [\![E \,||\, F \equiv \text{the parallel combination of resistances } E \text{ and } F]\!]$$

$$R_B^* = R_B^- \,||\, \left(R + R^*\right) = \frac{\left(R + R^*\right)R_B^-}{\left(R + R^*\right) + R_B^-}$$

Note that if there is only one pore in bilayer B, we set $R_B^- = \infty$, $R_B = R$, and $R_B^* = R + R^*$.

We first analyze the binding events. For $t < 0$, we assume that the switch is *closed* (Fig. 2.4 *C*, pore unblocked). Both capacitors will effectively be open circuits at $t = 0$. Hence, all of the current flows through the resistors, and the initial voltage at the middle node, $V(t)$, is $V(t=0) = \left(\frac{R_A}{R_A + R_B}\right) V_{cc}$.

At $t = 0$, the switch opens to simulate the non-covalent binding of a blocker. We apply Kirchhoff's Current Law at the middle node to obtain

$$\frac{V_{cc} - V(t)}{R_B^*} + C_B \frac{d\left(V_{cc} - V(t)\right)}{dt} = \frac{V(t)}{R_A} + C_A \frac{dV(t)}{dt}$$

rearranging,

$$\frac{dV(t)}{dt} + \frac{R_A + R_B^*}{R_A R_B^* \left(C_A + C_B\right)} V(t) = \frac{V_{cc}}{R_B^* \left(C_A + C_B\right)}$$

$$\frac{dV(t)}{dt} + \gamma V(t) = \theta$$

where $\gamma = \frac{R_A + R_B^*}{R_A R_B^* \left(C_A + C_B\right)}$, $\theta = \frac{V_{cc}}{R_B^* \left(C_A + C_B\right)}$

multiplying through by $\exp(\gamma t)$,

$$\frac{dV(t)}{dt}\exp(\gamma t)+V(t)\gamma\exp(\gamma t)=\theta\exp(\gamma t)$$

recognizing that the left side of the equation can be expressed as the derivative of a product, and integrating both sides with respect to time,

$$\int\frac{d}{dt}\left(V(t)\exp(\gamma t)\right)dt=\int\theta\exp(\gamma t)dt$$
$$V(t)\exp(\gamma t)=\frac{\theta}{\gamma}\exp(\gamma t)+K$$
$$V(t)=\frac{\theta}{\gamma}+K\exp(-\gamma t)$$

applying the initial condition,

$$V(t=0)=\frac{R_A}{R_A+R_B}V_{cc}=\frac{\theta}{\gamma}+K$$
$$K=\left[\frac{R_A}{R_A+R_B}-\frac{R_A}{R_A+R_B^*}\right]V_{cc}$$

yields the solution to the first order homogeneous differential equation:

$$V(t)=\left[\frac{R_A}{R_A+R_B^*}\right]V_{cc}+\left[\frac{R_A}{R_A+R_B}-\frac{R_A}{R_A+R_B^*}\right]V_{cc}\exp\left(-\frac{R_A+R_B^*}{R_AR_B^*(C_A+C_B)}t\right)$$

After a binding event, the current through the network as a function of time is given by

$$I_{block}(t)=\frac{V(t)}{R_A}+C_A\frac{dV(t)}{dt}=\frac{V_{cc}-V(t)}{R_B^*}-C_B\frac{dV(t)}{dt}$$

$$I_{block}(t) = \alpha + \beta \exp(-\gamma t)$$

where

$$\alpha = \frac{V_{cc}}{R_A + R_B^*}$$

$$\beta = \frac{R_B^* - R_B}{R_B^*(R_A + R_B)(R_A + R_B^*)(C_A + C_B)} V_{cc}\left[R_B^* C_B - R_A C_A\right] \tag{2.1}$$

$$\gamma = \frac{R_A + R_B^*}{R_A R_B^*(C_A + C_B)}$$

The same approach was used to derive expressions for the current through the network after a dissociation event:

$$\frac{dV(t)}{dt} + \frac{R_A + R_B}{R_A R_B (C_A + C_B)} V(t) = \frac{V_{cc}}{R_B (C_A + C_B)},$$

$$V(0) = \frac{R_A}{R_A + R_B^*} V_{cc}, \text{ and}$$

$$I_{unblock}(t) = \alpha' + \beta' \exp(-\gamma' t)$$

where

$$\alpha' = \frac{V_{cc}}{R_A + R_B}$$

$$\beta' = \frac{R_B^* - R_B}{R_B (R_A + R_B)(R_A + R_B^*)(C_A + C_B)} V_{cc}\left[R_A C_A - R_B C_B\right] \tag{2.2}$$

$$\gamma' = \frac{R_A + R_B}{R_A R_B (C_A + C_B)}$$

where $I_{unblock}(t)$ is the total current through the network as a function of time following dissociation. We have chosen t = 0 as the start of the dissociation event to simplify the expressions.

To compare this analysis with the experimental trace of a (A1,B1) blocking event (Fig. 2.4 *D*), we assigned the following parameter values (Fig. 2.4 *C*): R_A = 0.9 GΩ, R_B = 1

GΩ (R = 1 GΩ, R_B^- = ∞), R_B^* = 10 GΩ (R^* = 9 GΩ). The experimental setup does not enable straightforward determination of the capacitance of each bilayer, only the net capacitance. However, it is possible to infer the bilayer capacitances by adjusting them in the model until the theoretical or simulated trace matches the experimental trace, while making sure that the net capacitance is in agreement with experimental measurements. Applying this strategy, we found that C_A ≈ 350 pF and C_B ≈ 500 pF (Fig. 2.4 *C*). The theoretical current vs. time trace of a TRIMEB blocking event (Fig. 2.4 *D*, overlay created with Microsoft Excel) is similar to the experimental trace (Fig. 2.4 *D*).

2.2.4. Characteristics of Blocking Events in the Double DIB Network

The binding and dissociation current expressions in Eqs. 2.1 and 2.2 exhibit initial steps to $\alpha+\beta$ and $\alpha'+\beta'$, respectively, followed by an exponential decay towards steady-state current levels given by α and α', respectively. Depending on the signs of β and β', there are three possible types of behavior in the network current for both binding and dissociation: (1) "undershoot," (2) "exact," and (3) "overshoot." We define these terms as follows: the initial step in current (1) falls short of, i.e., undershoots, the new current level such that the step and decay occur in the same direction (Fig. 2.5 *A, C* and *D*), (2) steps to the new steady-state current level exactly such that there is no subsequent decay phase, and (3) goes beyond, i.e., overshoots, the new steady-state current level such that the step and decay occur in opposite directions (Fig. 2.5 *E, G* and *H*). Mathematically, the conditions for these three types of behavior are given by

$V_{cc} < 0$, so $\alpha, \alpha' < 0$

Undershoot:	$\beta < 0$ requires that $R_A C_A < R_B^* C_B$	$[\![\text{binding}]\!]$
	$\beta' > 0$ requires that $R_A C_A < R_B C_B$	$[\![\text{dissociation}]\!]$
Exact:	$\beta = 0$ requires that $R_A C_A = R_B^* C_B$	$[\![\text{binding}]\!]$
	$\beta' = 0$ requires that $R_A C_A = R_B C_B$	$[\![\text{dissociation}]\!]$
Overshoot:	$\beta > 0$ requires that $R_A C_A > R_B^* C_B$	$[\![\text{binding}]\!]$
	$\beta' < 0$ requires that $R_A C_A > R_B C_B$	$[\![\text{dissociation}]\!]$

(2.3)

After the blocker binds, the potential across bilayer A decreases as C_A discharges, while the potential across bilayer B increases as C_B charges (Fig. 2.4 *C*). When the blocker dissociates, the reverse occurs. The *RC* time constant of each bilayer governs the rate at which it can charge or discharge. Thus, the net current will behave differently upon binding or dissociation depending on the relative magnitudes of the *RC* constants for the two bilayers as shown in Eq. 2.3. The binding and dissociation cases are not symmetrical because the *RC* constant for binding includes the blocker resistance (i.e., R_B^*) whereas that for dissociation does not (i.e., R_B).

For simplicity, the rest of this section pertains to experiments where we set $C_A \approx C_B$, which allows us to neglect the capacitances present in Eq. 2.3. At a given steady-state unblocked current level, only one type of blocking event is observed. For example, Eq. 2.3 dictates that undershoot binding-undershoot dissociation, or undershoot-undershoot type blocking events occur when $R_A < R_B$. For example, bilayer-pore configuration (A2,B1) yields undershoot-undershoot blocking events (Fig. 2.5 *A, B,* and *C*). Using SPICE (Simulation Program with Integrated Circuit Emphasis) to perform a time domain analysis of the equivalent circuit yields a similar trace (Fig. 2.5 *D*). On the other hand, overshoot-overshoot type blocking events occur when $R_A > R_B^*$ (Fig. 2.5 *E*). For bilayer-pore configuration (A2,B4) (Fig. 2.5 *F*), the experimental results (Fig. 2.5 *G*) and

simulation results (Fig. 2.5 *H*) are again similar. Notice that these two types of current blocking events are the same as those seen in the "O-U" network (Fig. 2.2). When $R_B^* > R_A > R_B$, e.g., (A2,B3), undershoot-overshoot blocking events are the result. Furthermore, the theoretical analysis predicts that it is not possible to observe overshoot-undershoot blocking events because $R_B < R_B^*$ by definition.

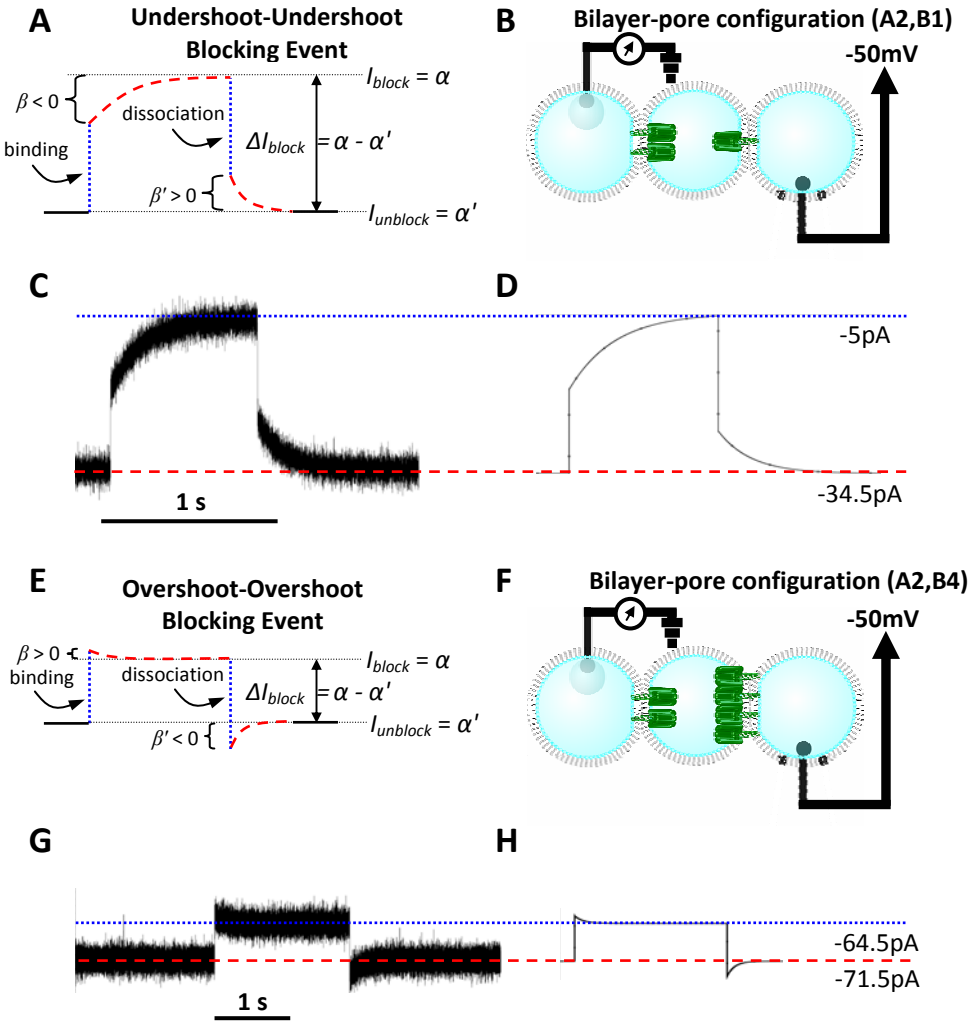

Figure 2.5 Types of Blocking Events in a Double DIB Network. (*A*) Diagram of undershoot-undershoot blocking event. Both the binding and dissociation consist of an undershoot phase (relative to the new steady state current level) and an exponential decay phase. (*B*) Schematic of double DIB system in (A2,B1) bilayer-pore configuration. (*C*) Experimental current trace, and (*D*) simulated current trace of a TRIMEB undershoot-undershoot blocking event for bilayer-pore configuration (A2,B1). C_A = C_B = 300 pF. (*E*) Diagram of overshoot-overshoot blocking event. Both the binding and dissociation consist of an overshoot phase (relative to the new steady state current level) and an exponential decay phase. (*F*) Schematic of double DIB system in (A2,B4) bilayer-pore configuration. (*G*) Experimental current trace, and (*H*) simulated current trace of a TRIMEB overshoot-overshoot blocking event for bilayer-pore configuration (A2,B4). C_A = C_B = 300 pF.

In actuality, DIBs also have series resistance from the buffer solution, which will have some effect on the resulting network current. The SPICE simulations show that changing the series resistance for each bilayer up to 100 kΩ has no significant effect on the results.

In agreement with the experimental data, the simulated magnitude (i.e., $\Delta\alpha = \alpha - \alpha'$) of undershoot-undershoot blocking events (Fig. 2.5 *D*) is generally larger than that of the overshoot-overshoot events (Fig. 2.5 *H*). The network tends towards undershoot-undershoot type events as pores are added to bilayer A and overshoot-overshoot type events as pores are added bilayer B. The overshoot-overshoot blocking events are smaller because the blocking of a pore in membrane B becomes less significant when there are other open pores in the same membrane.

2.2.5. Generalizing Observed Experimental Trends using Mathematical Analysis

An important advantage that theoretical analysis offers is the ability to verify or refute the generalizability of observed experimental trends. For example, we observed that the initial step in current upon binding is smaller than that of dissociation (Fig. 2.5 *C*, *D*, *G* and *H*). To determine whether this observation is true in general, we express it mathematically as

$$\left|(\alpha+\beta)-\alpha'\right| \stackrel{?}{<} \left|\alpha-(\alpha'+\beta')\right|$$

which simplifies to

$$\left\{\begin{array}{l}\beta \stackrel{?}{<} -\beta',\ V_{cc}<0\\ \beta \stackrel{?}{>} -\beta',\ V_{cc}>0\end{array}\right\}$$

$$\beta = \frac{V_{cc}R^*C_B}{(R_A+R_B)(C_A+C_B)(R_A+R_B+R^*)} - \frac{V_{cc}R^*R_AC_A}{(R_B+R^*)(R_A+R_B)(C_A+C_B)(R_A+R_B+R^*)}$$

$$\beta' = \frac{V_{cc}R^*R_AC_A}{R_B(R_A+R_B)(C_A+C_B)(R_A+R_B+R^*)} - \frac{V_{cc}R^*C_B}{(R_A+R_B)(C_A+C_B)(R_A+R_B+R^*)}$$

$$\text{let } \chi = \frac{R_B^*-R_B}{(R_A+R_B)(R_A+R_B^*)(C_A+C_B)}C_BV_{cc}$$

$$\varepsilon = \frac{R_B^*-R_B}{R_B^*(R_A+R_B)(R_A+R_B^*)(C_A+C_B)}R_AC_AV_{cc}$$

$$\varepsilon' = \frac{R_B^*-R_B}{R_B(R_A+R_B)(R_A+R_B^*)(C_A+C_B)}R_AC_AV_{cc}$$

$$\text{then } \beta = \chi - \varepsilon \text{ and } -\beta' = \chi - \varepsilon'.$$

$$\text{if } V_{cc} < 0,$$
$$\varepsilon, \varepsilon' < 0; \varepsilon > \varepsilon' \Rightarrow \beta < -\beta'.$$
$$\text{if } V_{cc} > 0,$$
$$\varepsilon, \varepsilon' > 0; \varepsilon < \varepsilon' \Rightarrow \beta > -\beta'.$$

$$\therefore \left|(\alpha+\beta)-\alpha'\right| < \left|\alpha-(\alpha'+\beta')\right|$$

In other words, we have shown that $|\beta| > |\beta'|$ for undershoot-undershoot events and $|\beta| < |\beta'|$ for overshoot-overshoot events. The only other cases to consider are undershoot-exact, undershoot-overshoot, and exact-overshoot events, which by definition will exhibit larger dissociation current steps than binding current steps. Thus, we conclude that the initial current step associated with binding is indeed smaller than that of dissociation for all bilayer-pore configurations.

It was also experimentally observed that the decay rate for binding events is smaller than that of dissociation events. To determine if this is true in general, we note that Eqs. 2.1 and 2.2 tell us that the decay rates for binding and dissociation events are governed by γ and γ', respectively.

$$\frac{\gamma}{\gamma'} = \frac{R_A R_B + R_B R_B^*}{R_A R_B^* + R_B R_B^*}$$

since $R_B < R_B^*, \frac{\gamma}{\gamma'} < 1$

$\therefore \gamma < \gamma'$.

Thus, the exponential decay rate for dissociation is greater than that of binding in all cases.

2.2.6. Separation of Current into Components during Blocking Events

One of the most useful features of SPICE simulations is the ability to probe the voltage at any node and the current through any element in the network as a function of time. Experimentally, this would be equivalent to plugging the electrodes into different droplets in the network. However, such an action would be undesirable with the present setup because it would fundamentally change the circuit since the same electrodes provide the voltage-clamp and measurement capabilities.

As required by Kirchhoff's Current Law and shown in Eqs. 2.1 and 2.2, the sum of the capacitive current (I_{C_A}) and the pore current (I_{R_A}) for bilayer A (Fig. 2.6, *left column*) must equal the net current through the entire network (Fig. 2.6, *middle column*). This must also be the case for bilayer B (Fig. 2.6, *right column*). This fundamental property can be verified with SPICE simulations for all types of blocking events, including undershoot-undershoot (Fig. 2.6 *A*) and overshoot-overshoot (Fig. 2.6 *B*). Notice that the capacitive currents are opposite in direction and equal in magnitude when $C_A = C_B$ (Fig. 2.6). Moreover, the pore current through bilayer A is continuous whereas that through bilayer B is discontinuous (Fig. 2.6).

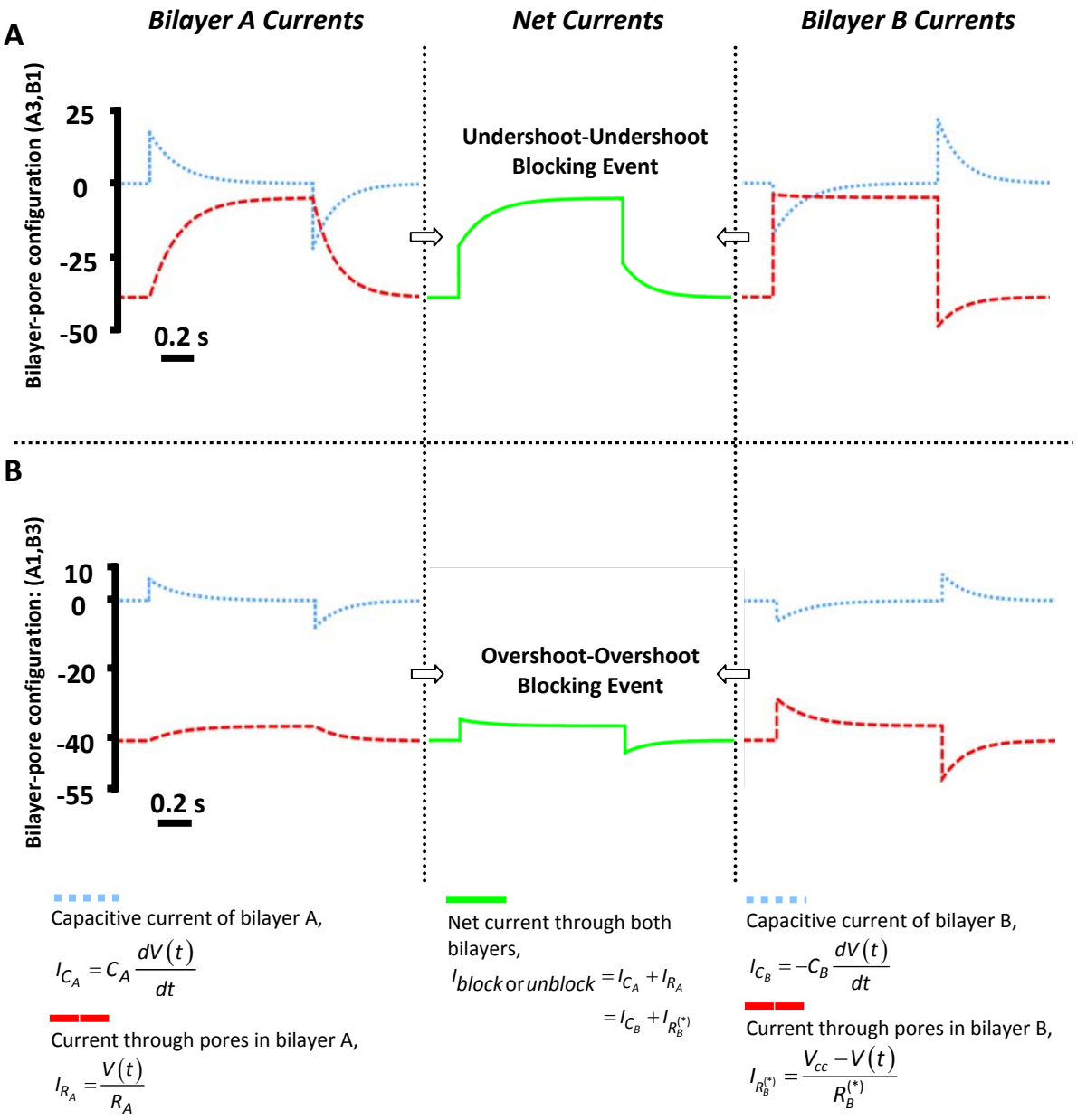

Figure 2.6 Separation of Current during Blocking Events into Components. SPICE was used to simulate a one second TRIMEB blocking event. The bilayer capacitances are C_A = C_B = 300 pF. The resistance of each pore in bilayer A is 0.9 GΩ and in bilayer B is 1 GΩ. The effective resistance of the blocker is 9 GΩ. The net current (solid lines, middle column) through the double DIB network can be separated into a capacitive current (dotted lines) and pore current (dashed lines) for each bilayer (bilayer A: left column, bilayer B: right column). By Kirchhoff's Current Law, the sum of the pore current and capacitive current for bilayer A and that for bilayer B both equal the net current through the network. Upon blocker binding, bilayer A discharges, bilayer B charges, and the pore currents for both bilayers decrease. Upon dissociation, bilayer A charges, bilayer B discharges, and the pore currents for both bilayers increase. (*A*) Bilayer-pore configuration (A3,B1) yields an undershoot-undershoot blocking event. (*B*) Bilayer-pore configuration (A1,B3) yields an overshoot-overshoot blocking event.

2.2.7. Effects of Bilayer Capacitance on Blocking Event Characteristics

Unlike the case with planar bilayers, it is possible to change the capacitance of DIBs during an experiment. A dual movable electrode setup (Fig. 2.7 *A*) enabled us to modulate the capacitance of one bilayer with minimal perturbation of the other. The experimental and simulated TRIMEB blocking events seen in bilayer-pore configuration (A9,B8) displayed undershoot-undershoot characteristics (Fig. 2.7 *B* and *C*). The capacitance of both bilayers was ~400 pF. The capacitance of bilayer B was then reduced by moving the corresponding electrode to the right (Fig. 2.7 *A*, arrow). Bilayer B gradually shrank over the span of 90 seconds and the characteristics of blocking events changed accordingly while the bilayer-pore configuration remained (A9,B8). Immediately prior to bilayer B separation, the blocking events began displaying overshoot-overshoot characteristics (Fig. 2.7 *D* and *E*) as predicted by Eq. 2.3. These results demonstrate that bilayer resistances and capacitances are both important in determining the characteristics of blocking events and that a physical change to the DIB network can alter the overall electrical behavior.

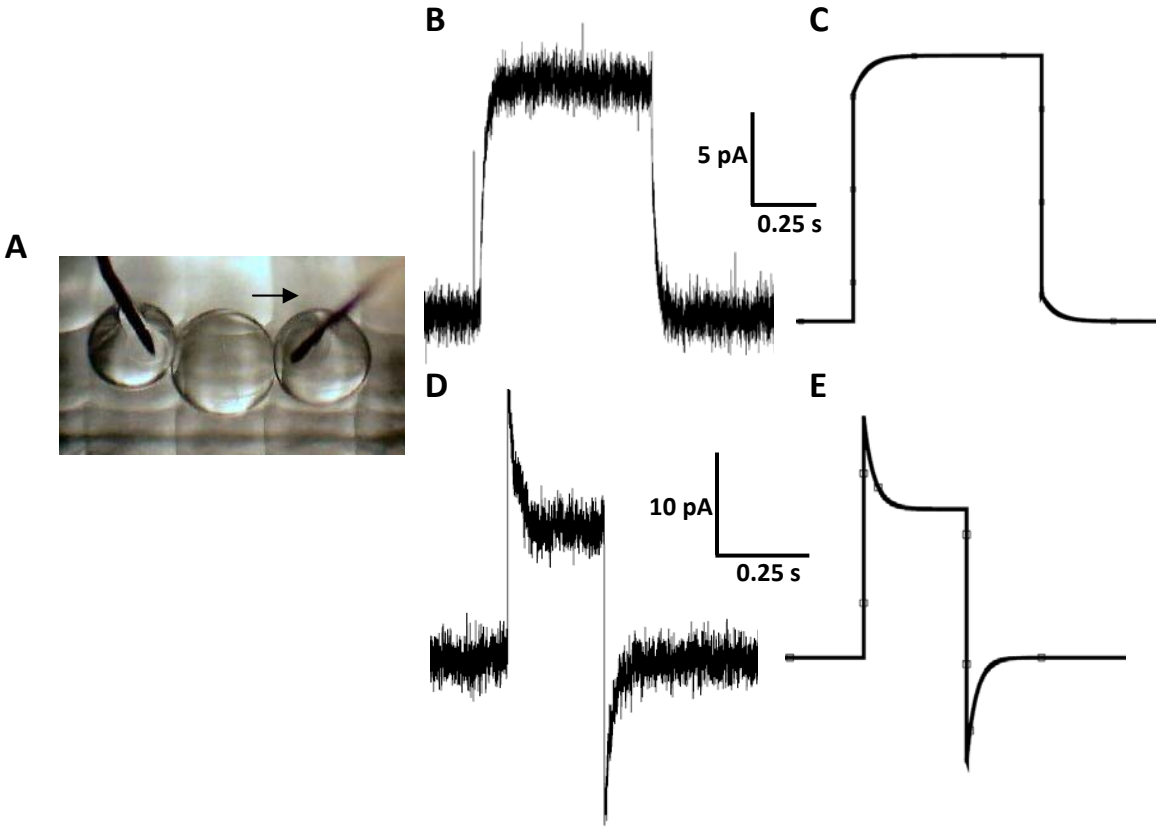

Figure 2.7 Effects of Bilayer Capacitance on Blocking Event Characteristics. (*A*) Double DIB setup with two movable electrodes. Left droplet contains buffer (10 mM MOPS, 1 M KCl, pH 7.0), middle droplet contains 1.7 ng/mL αHL heptamer in buffer, and right droplet contains 10 μM TRIMEB in buffer. The potential (-50 mV) is applied to the right droplet and the left droplet is grounded. (*B*) Experimental current trace of blocking event in bilayer-pore configuration (A9,B8). (*C*) Simulated current trace of blocking event in bilayer-pore configuration (A9,B8) with C_A = 400 pF and C_B = 400 pF. (*D*) Bilayer B (droplets M and R) was reduced in size by moving the right electrode to the right as indicated by the arrow in part *A*. Over 90 seconds, bilayer B gradually shrank until droplets M and R separated. The experimental current trace of a blocking event in bilayer-pore configuration (A9,B8) immediately before bilayer B separated is shown. (*E*) Simulated current trace of blocking event in bilayer-pore configuration (A9,B8) with C_A = 400 pF and C_B = 25 pF.

2.2.8. Net Current during Pore Insertions in the Double DIB Network

Unlike the single DIB case, where the insertion of each additional pore is characterized by a current step of the same magnitude (Fig. 2.8 *A*), current steps are variable in the double DIB network (Fig. 2.8 *B*). We simulated pore insertions in double DIB networks with an analysis similar to that presented for blocking events. To model a pore insertion into bilayer A, we add a resistor, *R*, in parallel with the net bilayer resistance, R_A^-, at t = 0 by closing the switch (Fig. 2.8 *C*). The net resistance of bilayer A

after pore insertion is $R_A = R \,||\, R_A^- = \frac{R R_A^-}{R + R_A^-}$. The net resistance of bilayer B is R_B, and the capacitances of bilayers A and B are C_A and C_B, respectively. Since the switch was open for $t < 0$, the initial condition is $V(t=0) = \left(\frac{R_A^-}{R_A^- + R_B} \right) V_{cc}$.

Applying Kirchhoff's Current Law to the middle node,

$$\frac{V_{cc} - V(t)}{R_B} + C_B \frac{d\left(V_{cc} - V(t)\right)}{dt} = \frac{V(t)}{R_A} + C_A \frac{dV(t)}{dt}$$

The solution for *V(t)* is

$$V(t) = \left[\frac{R_A}{R_A + R_B} \right] V_{cc} + \left[\frac{R_A^-}{R_A^- + R_B} - \frac{R_A}{R_A + R_B} \right] V_{cc} \exp\left(-\frac{R_A + R_B}{R_A R_B \left(C_A + C_B\right)} t \right).$$

The current through the network as a function of time is given by

$$I_{insert}(t) = \alpha'' + \beta'' \exp(-\gamma'' t)$$

where

$$\alpha'' = \frac{V_{cc}}{R_A + R_B} = \alpha' \qquad (2.4)$$

$$\beta'' = \frac{\left(R_A C_A - R_B C_B\right)\left(R_A - R_A^-\right)}{R_A \left(R_A + R_B\right)\left(R_A^- + R_B\right)\left(C_A + C_B\right)} V_{cc}$$

$$\gamma'' = \frac{R_A + R_B}{R_A R_B \left(C_A + C_B\right)} = \gamma'$$

Note that the steady-state current after a pore insertion (α'') is the same as that after dissociation of a blocker (α') when both events occur with the same final bilayer-pore configuration.

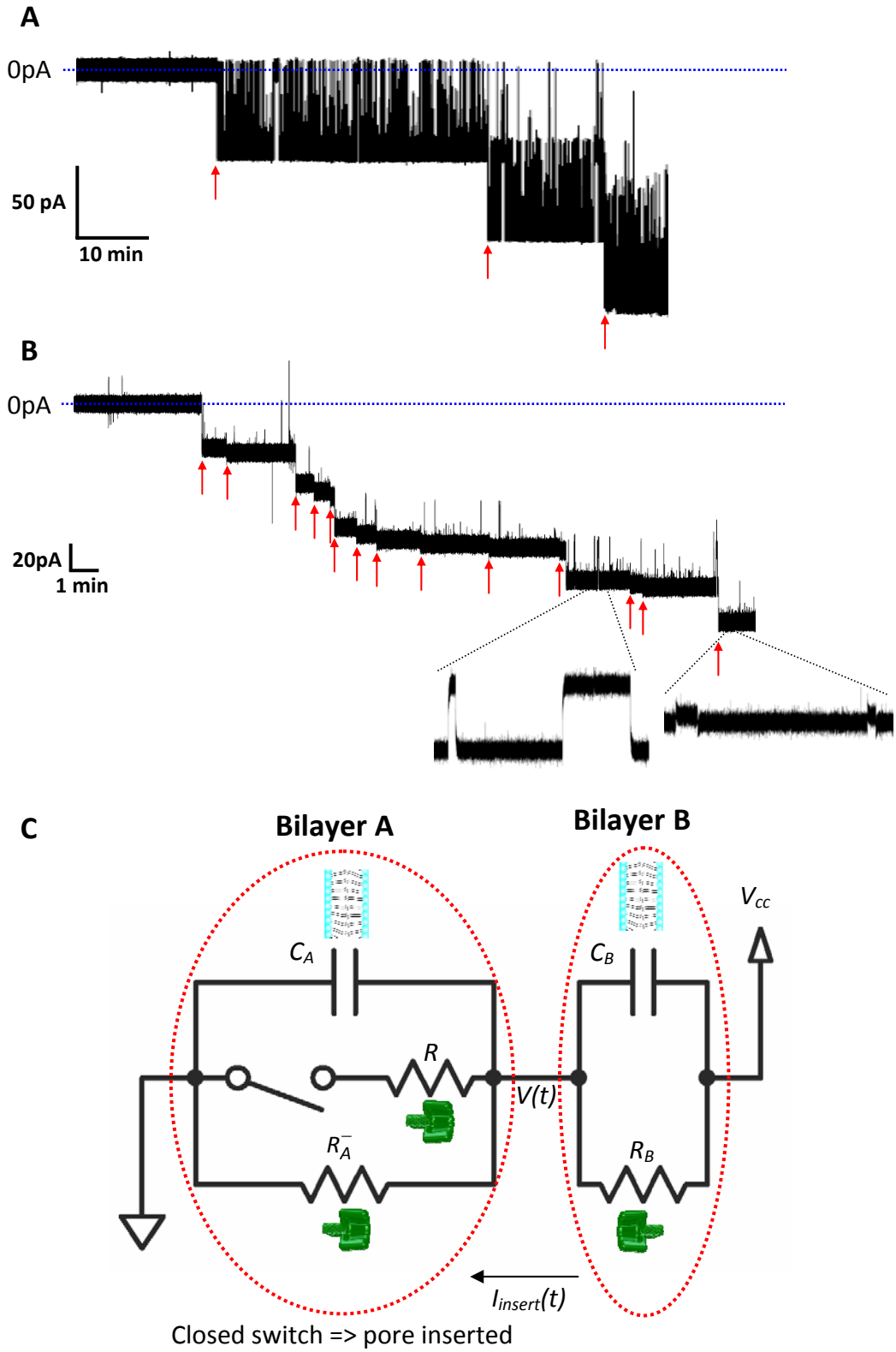

Figure 2.8 Pore Insertions in Single DIB and Double DIB Experiments. (*A*) Experimental current trace during pore insertions in a single DIB system with TRIMEB blocking events. Droplet contents are described in Figure 2.3. The current steps and blocking events are uniform in size. Pore insertions are marked with arrows. (*B*) Experimental current trace during pore insertions in a double DIB system with TRIMEB blocking events. Droplet contents are described in Figure 2.4. The current steps and blocking events exhibit a range of sizes. Two regions of the trace illustrating different types of blocking events are expanded for clarity. (*C*) Circuit schematic of double DIB system for analysis of pore insertions. C_A is the capacitance of bilayer A.

R_A^- is the net resistance of bilayer A before pore insertion. C_B is the capacitance and R_B is the net resistance of bilayer B. A new pore, R, is inserted into bilayer A by closing the switch.

2.2.9. Characteristics of Pore Insertions in the Double DIB Network

Depending on the sign of β'', there are three possible types of behavior in the network current upon insertion of an additional pore (Fig. 2.9 *B*): (1) "undershoot," (2) "exact," and (3) "overshoot." These terms are defined as before. Mathematically, the conditions for these three types of behavior are given by

$$\begin{aligned} &V_{cc} < 0, \text{ so } \alpha'' < 0 \\ &\text{Undershoot: } \beta'' > 0 \text{ requires that } \left(R_A C_A - R_B C_B\right)\left(R_A - R_A^-\right) < 0 \\ &\text{Exact: } \quad \beta'' = 0 \text{ requires that } \left(R_A C_A - R_B C_B\right)\left(R_A - R_A^-\right) = 0 \\ &\text{Overshoot: } \beta'' < 0 \text{ requires that } \left(R_A C_A - R_B C_B\right)\left(R_A - R_A^-\right) > 0 \end{aligned} \tag{2.5}$$

The above conditions can be generalized to the situation where the new pore inserts into bilayer B by replacing all "A" subscripts with "B" and vice versa. Note that R takes on a different value depending on which bilayer the pore inserts into because of the rectification properties of αHL (Miles et al., 2001).

2.2.10. Spatial and Temporal Localization of Pore Insertions

Although pores and channels in droplets will continue to insert into DIBs for some time after network creation, the approximate number of pores and channels in a given DIB can be controlled by adjusting the dilution of the protein. By analyzing three key features of current traces obtained from double DIB experiments, we can determine when and where each new pore inserts during an experiment (Fig. 2.9 *A*). First, because of the rectification properties of αHL, the steady-state unblocked current level (α') given by Eq. 2.2 indicates the bilayer-pore configuration, although it is theoretically possible for more than one bilayer-pore configuration to have the same α'. Second, the nature of the current increase induced by a pore insertion will depend on the bilayer-pore

configurations before and after the insertion event as shown by Eq. 2.4. Third, the characteristics of blocking events also indicate the bilayer-pore configuration.

We demonstrate spatial and temporal localization of pore insertions in a single experiment (Fig. 2.9 *A*). The first current step of α' ≈ -34.5 pA shows that the configuration of pores is (A2,B1). This current step corresponds to pore insertion into bilayer B. If the configuration is (A1,B2) instead, then α' ≈ -36 pA. The difference in steady-state current between (A2,B1) and (A1,B2) is a result of the rectification properties of αHL. Further confirmation comes from examining a blocking event at this current level. The large (~30 pA) undershoot-undershoot blocking event establishes the bilayer-pore configuration is (A2,B1). If the configuration is (A1,B2) instead, Eq. 2.3 reveals that we would observe undershoot-overshoot blocking events because $R_B < R_A < R_B^*$. Thus, we conclude that the first transition observed in the current trace must be (A2,B0) => (A2,B1).

For the second pore insertion, both the new unblocked steady-state current level of -38.5 pA and the characteristics of the blocking events suggest that the bilayer-pore configuration is (A3,B1) and not (A2,B2). However, in this case, the most direct method of determining where the pore inserted is to examine the characteristics of the pore insertion itself. An overshoot-type pore insertion event is observed (Fig. 2.9); if the insertion occurred in bilayer B instead, an undershoot-type pore insertion event would be expected. Therefore, the second transition is (A2,B1) => (A3,B1). The same method can be applied to the third pore insertion (Fig. 2.9) to yield (A3,B1) => (A3,B2).

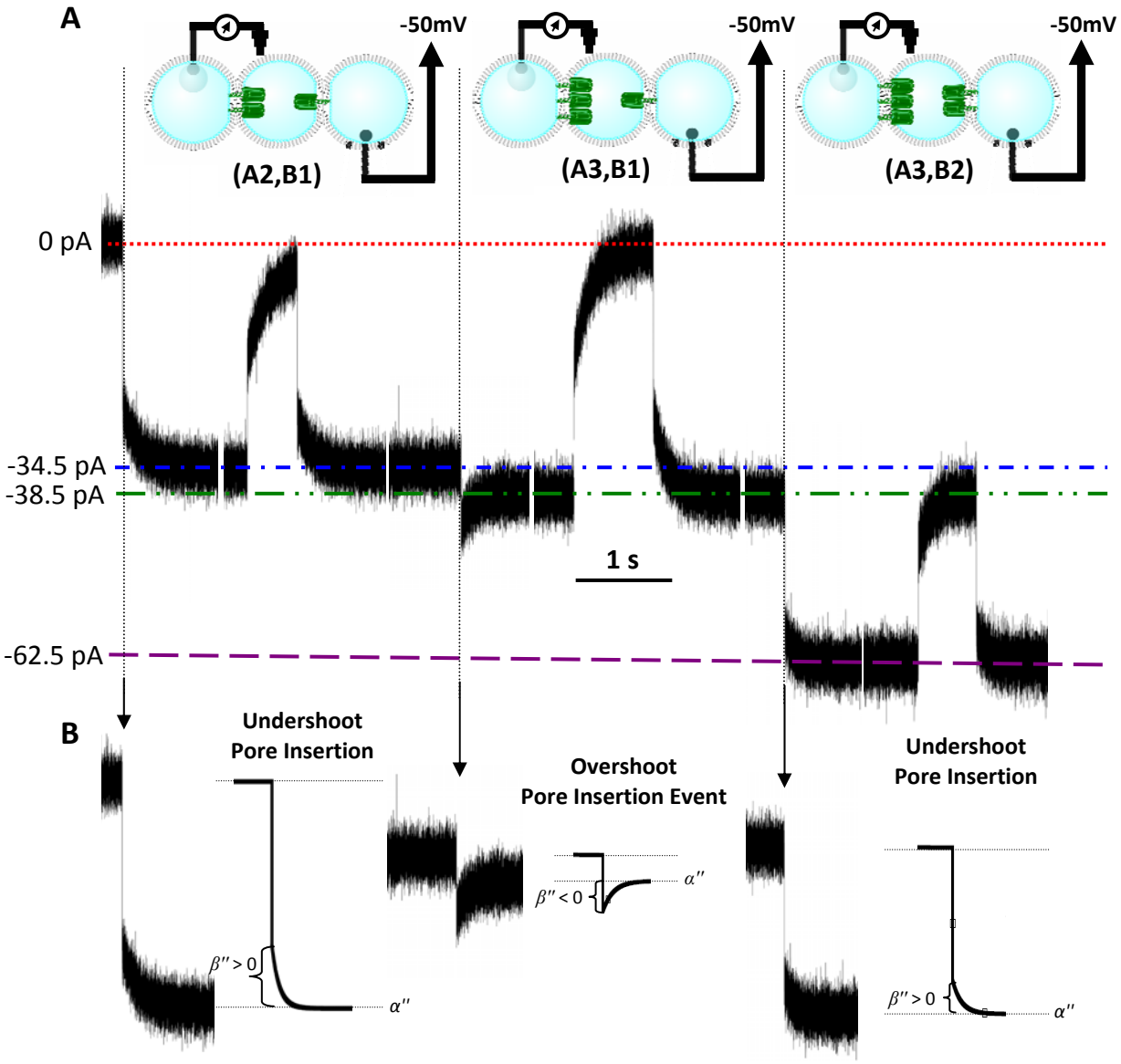

Figure 2.9 Spatial and Temporal Localization of Pore Insertions. (*A*) Current trace from one double DIB experiment illustrating (A2,B0) => (A2,B1) => (A3,B1) => (A3,B2) pore insertions. Droplet contents are described in Figure 2.4. The trace is presented as six segments separated by gaps to save space. Only one blocking event at each current level is shown. Horizontal lines indicate the current levels for 0 pA and (A2,B1), (A3,B1), and (A3,B2), respectively. Pore insertions are indicated by vertical dotted lines. (*B*) Simulated current traces of (A2,B0) => (A2,B1), (A2,B1) => (A3,B1), and (A3,B1) => (A3,B2) pore insertions juxtaposed with corresponding segments of the experimental traces. C_A = C_B = 300 pF. R = 0.9 GΩ for insertions into bilayer A and R = 1 GΩ for insertions into bilayer B.

2.3. Conclusion

The electrical behavior of a network of bilayers with incorporated pores differs dramatically from that of single bilayer systems (Fig. 2.2). For example, in DIB networks, the same physical and chemical interaction of a reversible pore blocker such as TRIMEB with an αHL pore can have distinctly different effects on the network current depending on several factors such as bilayer-pore configuration and bilayer areas. To investigate the basis for these differences, we used electrical circuit analysis and SPICE simulations to analyze protein pore insertion and blockade in a simple three-droplet, two-bilayer network. Our analysis provides explicit mathematical relationships that specify the conditions under which each type of pore blocking or insertion event is expected to occur. In fact, our analysis of the three-droplet network enables us to understand the electrical phenomena seen in more complex networks, such as the "O-U" system (compare Fig. 2.2 *D* with Fig. 2.5).

The experimental methods do not directly enable the determination of how many pores are in each of the two membranes since the electrodes are separated by two bilayers. However, we showed that SPICE simulation offers a rapid method of exploring pore distributions between the two bilayers. The synergy of experiment, theory, and simulation enabled the determination of when and where each successive pore inserts. We have shown that the events at one interface (e.g., current blockades) can provide information about phenomena (e.g., pore insertions) at another bilayer in the network.

Pores and channels that exhibit a variety of conductance, ion selectivity, rectification, gating, and blocker interaction properties provide a toolbox for developing more elaborate DIB networks. Genetically engineered αHL pores can be tailored to

provide a range of specific functions, including specific blocker affinities, ion selectivities, rectification, and reactivity (Bayley & Cremer, 2001; Bayley & Jayasinghe, 2004; Gu et al., 1999; Gu et al., 2001a; Gu et al., 2001b; Gu et al., 2000). As networks become more complex, simulations will be critical for predicting and understanding network behavior. Therefore, the present analysis of a simple DIB network will be instrumental in the development of larger, functional networks. Complex networks can be treated as modular arrangements of simpler systems, such as the three droplet network.

The ability to form networks of "protocells" that communicate through membrane proteins forms a basis for the development of an artificial platform for studying multicellular biological systems (Basu et al., 2004; Chen et al., 2005). For example, electrically propagating systems, such as the heart, might be mimicked by DIB networks containing channels found in cardiac tissue. This may allow us to simulate and study the properties and mechanisms of electrical impulse propagation, as well as the fundamental underpinnings of pathological behavior (Kleber & Rudy, 2004).

2.4. Methodology

2.4.1. DIB Network Platform

A 10 x 10 x 4 mm Perspex chamber was micromachined with an array of divots on the bottom surface (1 mm diameter, 700 μm center-to-center spacing; Fig. 2.1). Ag/AgCl electrodes were inserted through holes (200 μm diameter) drilled on the bottom side of the divots. The chamber was sealed with UV curable glue. These fixed surface electrodes were wired together to the working end of a patch clamp headstage (Axopatch 200B, Axon Instruments, Union City, CA).

Another Ag/AgCl electrode was attached to a micromanipulator (NMN-21, Narishige, London, UK). It was rendered hydrophilic by coating with 5% w/v low melt

agarose in buffer (10 mM MOPS, 1 M KCl, titrated to pH 7.0 with KOH). This movable electrode was connected to the grounded end of the patch clamp headstage (Fig. 2.1). In some experiments, two movable electrodes were used to enable independent control of two droplet positions.

Positive current flow is defined as cations moving from the working end towards the grounded end of the headstage and anions flowing in the opposite direction.

2.4.2. DIB Networks

The Perspex chamber was filled with an oil-lipid solution consisting of 10 mM 1,2-diphytanoyl-sn-glycero-3-phosphocholine (DPhPC, Avanti Polar Lipids, Alabaster, AL) in hexadecane (Sigma Aldrich, Dorset, UK) (Fig. 2.1 *A*). We employed two methods to coat aqueous droplets (200 nL; P2 Gilson Pipetman, Anachem, Bedfordshire, UK) with lipid monolayers. In the first, droplets attached directly to agarose-coated Ag/AgCl electrodes were incubated in the oil-lipid bath for thirty minutes (Fig. 2.1 *B*). In the second, we filled a 20 cm section of 1.59 mm I.D. tubing with the oil-lipid solution and closed one end (Fig. 2.1 *A*). Droplets were injected into the open end and allowed to fall towards the closed end. The tube was then inverted and the open end was placed into the oil-lipid bath to enable the monolayer-encased droplets to fall onto the bottom of the micromachined chamber (Fig. 2.1 *B*). Insertion and removal of Ag/AgCl electrodes in these tube-stabilized droplets was straightforward.

Robust bilayers were spontaneously formed when droplets were brought into contact (Fig. 2.1 *C*). Networks of droplet interface bilayers (DIBs) were created by joining multiple droplets in linear and branched geometries. The capacitance of single or multiple bilayers was determined by applying a triangular voltage wave with a function generator (Iso-Tech GFG-8216A, Merseyside, UK).

2.4.3. Proteins and Reagents

Wild-type α-hemolysin heptamers (αHL) were prepared with two methods. In the first, *in vitro* transcription and translation was performed, followed by oligomerization on erythrocyte membranes. After separation by sodium dodecyl sulfate polyacrylamide gel electrophoresis, the heptamer band was excised from the gel and the protein was extracted (Cheley et al., 1997). In the second, wild-type αHL monomer from *Staphylococcus aureus* Wood strain 46 (American Type Culture Collection) was purified by a method described previously (Cheley et al., 1997). Heptamer formation was induced by treating purified monomer with deoxycholate at room temperature as detailed elsewhere (Bhakdi et al., 1981).[3]

The purified αHL heptamers were diluted to a concentration of between 1 and 120 ng/mL in the buffer used to form the aqueous droplets (10 mM MOPS, 1M KCl, pH 7.0). After dilution, any detergent that remained from gel purification did not affect the stability of the DIBs.

Heptakis(2,3,6-tri-O-methyl)-β-cyclodextrin (TRIMEB, CycloLab, Budapest, Hungary) exhibits transient, non-covalent interactions with αHL pores. This molecule was used to produce reversible current blocks.

2.4.4. Electrical Recordings

The electrodes were connected to a patch-clamp amplifier (Axopatch 200B). The Perspex chamber and amplifying headstage were enclosed in a metal box, which served as a Faraday cage. Currents were filtered with a low-pass Bessel filter (80 dB/decade) with a corner frequency between 500 Hz and 2 kHz and digitized with a DigiData 1320 A/D converter (Axon Instruments) at a sampling frequency of 10 kHz.

[3] Performed by Qiuhong Li.

2.4.5. Imaging

Images were taken with a Proscope digital USB microscope (Scalar Corporation, Baton Rouge, LA) attached to the eyepiece of a 40x stereomicroscope (StereoZoom5, Leica, Milton Keynes, UK).

2.4.6. Electrical Circuit Simulations

Simulation of electrical circuits was performed using SPICE (Simulation Program with Integrated Circuit Emphasis; PSpice 9.2 Lite Edition, Orcad, San Jose, CA).

Chapter 3

Asymmetric Droplet Interface Bilayers[4]

3.1. Introduction

The lipid compositions of the inner and outer leaflets of cell membranes differ (Devaux & Morris, 2004; Opdenkamp, 1979; Verkleij & Post, 2000). For example, in the outer membrane of Gram-negative bacteria, the outer leaflet is largely composed of lipopolysaccharides whereas the inner leaflet only includes phospholipids (Wiese et al., 1996). In the plasma membranes of eukaryotic cells, phosphatidylcholine and sphingomyelin predominate in the outer leaflet while aminophospholipids are primarily in the cytosolic leaflet (Devaux & Morris, 2004). The asymmetry of biological membranes is maintained by ATP-dependent processes, suggesting that it is critical to normal cell physiology (Pomorski et al., 2001). When these processes fail, the subsequent change in the chemical composition of the cell surface can lead to significant consequences. Rapid loss of bilayer asymmetry is observed with aging of erythrocytes (Diaz et al., 1996), maturation of sperm cells (Nolan et al., 1995), apoptosis (Fadok et al., 1992), and

[4] Adapted from HWANG, W. L., CHEN, M., CRONIN, B., HOLDEN, M. A. & BAYLEY, H. (2008). Asymmetric droplet interface bilayers. Journal of the American Chemical Society, 130(18), 5878-5879.

metabolic inhibition or ischemia of myocardial cells (Musters et al., 1993; Post et al., 1993). The appearance of phosphatidylserine (PS) on the outer leaflet of a cell membrane is often a sign of injury or apoptosis (Balasubramanian & Schroit, 2003; Fadok et al., 1992) and aids phagocytes in recognizing and ingesting the affected cell (Schroit et al., 1985). Moreover, cancer cells and vascular endothelial cells in tumors also display PS (Utsugi et al., 1991; Zwaal et al., 2005), which may be useful for targeted therapeutics. Other studies have suggested that the difference in bilayer asymmetry between prokaryotic and eukaryotic membranes is vital to the function of endogenous antimicrobial factors that selectively rupture bacterial membranes (Sato & Felix, 2006).

The biological prevalence and importance of asymmetric lipid bilayers has galvanized the exploitation of model systems, such as planar bilayers (Hagge et al., 2002; Krasilnikov et al., 1997; Sherwood & Montal, 1975; Wiese et al., 1996), supported bilayers (Crane et al., 2005; Katagiri et al., 2004; Wacklin & Thomas, 2007), and vesicles (McIntyre & Sleight, 1991; Pautot et al., 2003), to investigate the effects of bilayer asymmetry on the function of membrane proteins. However, the study of pores and ion channels by single-channel electrical recording using these systems is difficult. Electrical recording in supported bilayers requires access to the tiny ionic reservoir beneath the bilayer, which is quickly depleted when a constant potential is applied. Planar bilayers are useful for single-channel recording, but they are delicate and short-lived. Furthermore, once a planar bilayer breaks, the lipids mix and asymmetry is lost. Such experiments must be restarted, rendering the use of asymmetric planar bilayers tedious.

3.2. Results and Discussion

3.2.1. Formation of Asymmetric Droplet Interface Bilayers

The "lipid-out" DIB technique described in Chapters 1 and 2 uses lipids dissolved in the external oil bath, which means that all droplets are surrounded by an identical monolayer. In this chapter, we extend the DIB method by moving the lipids from the oil phase into the aqueous phase as vesicles (lipid-in DIBs, Fig. 3.1 *B*). The vesicles fuse at the oil-water interface to form a monolayer. Advantages of lipid-in DIBs over lipid-out DIBs include reduced experimental cost, since lipids are not included in the bulk oil phase, and a broader range of bilayer compositions, since a greater number of lipids can form vesicles than are soluble in oil. Moreover, by creating droplets with different vesicle compositions, droplets in the same bath can be encased by different monolayers, enabling the formation of asymmetric bilayers (Figs. 3.1 *B* and *C*).

Asymmetric droplet interface bilayers (a-DIBs) are stable for days to weeks and can be separated and reformed repeatedly. We formed an a-DIB between two 200 nL droplets: one contained vesicles with 10 mol% dimethyldioctadecylammonium bromide (DDAB, positively-charged) in 1,2-diphytanoyl-*sn*-glycero-3-phosphocholine (DPhPC, neutral) and the other contained vesicles with 10 mol% 1,2-dipalmitoyl-*sn*-glycero-3-[phosphor-*rac*-(1-glycerol)] (sodium salt) (DPPG, negatively-charged) in DPhPC. An applied potential of +100 mV was applied across the bilayer. The bilayer survived for more than 26 hours, and was only separated when the apparatus was needed for other experiments (Fig. 3.2). The area/capacitance of DIBs can be modulated easily (Fig. 3.2) (Hwang et al., 2007), which is advantageous for single-channel studies: initially, the bilayer area can be made large to maximize the chance of protein insertion, and then reduced to minimize the probability of further incorporation (Heron et al., 2007).

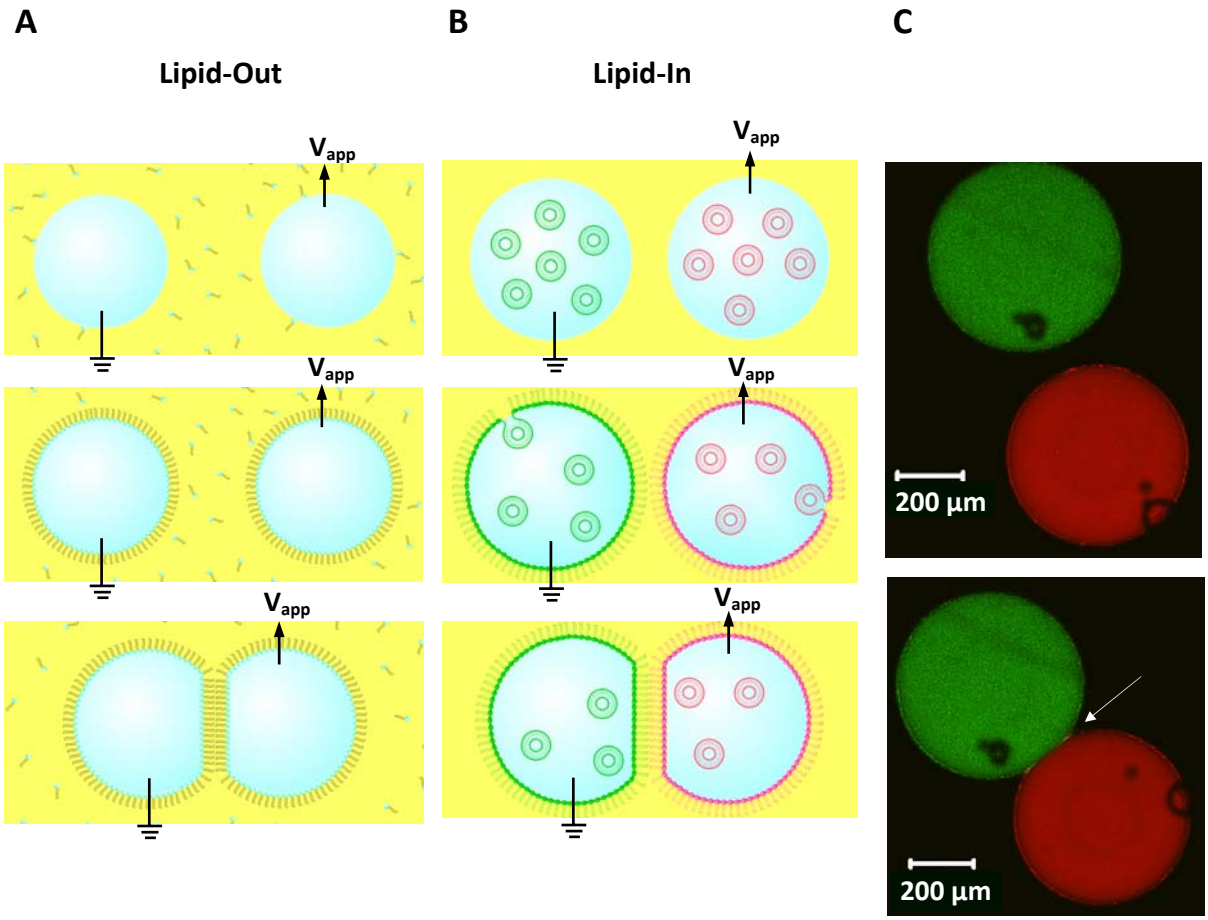

Figure 3.1 Lipid-out and Lipid-in Droplet Interface Bilayer Formation. *(A)* Symmetric lipid-out DIB formation (previously described (Holden et al., 2007; Hwang et al., 2007); not used in this paper). *Top:* Two aqueous droplets are deposited in a lipid-hexadecane solution. *(B)* Asymmetric lipid-in DIB formation. *Top:* Two types of aqueous droplets containing lipid vesicles of different compositions are deposited in a hexadecane reservoir. *(A and B) Middle:* A monolayer spontaneously forms at the oil-water interface. *Bottom*: Monolayer-encased droplets are brought together to form a stable bilayer. *(C)* Scanning confocal fluorescence *z*-slices of two droplets containing fluorescently-tagged lipids (Supporting Information). The top-left droplet contains 2 mM DPhPC vesicles doped with 2 mol% 1,2-dioleoyl-*sn*-glycero-3-phosphoethanolamine-N-(carboxyfluorescein) and the bottom-right droplet contains 2 mM DPhPC vesicles doped with 1 mol% 1,2-dipalmitoyl-*sn*-glycero-3-phosphoethanolamine-N-(lissamine rhodamine B sulfonyl). An asymmetric DIB (arrow) forms when the droplets are brought into contact.

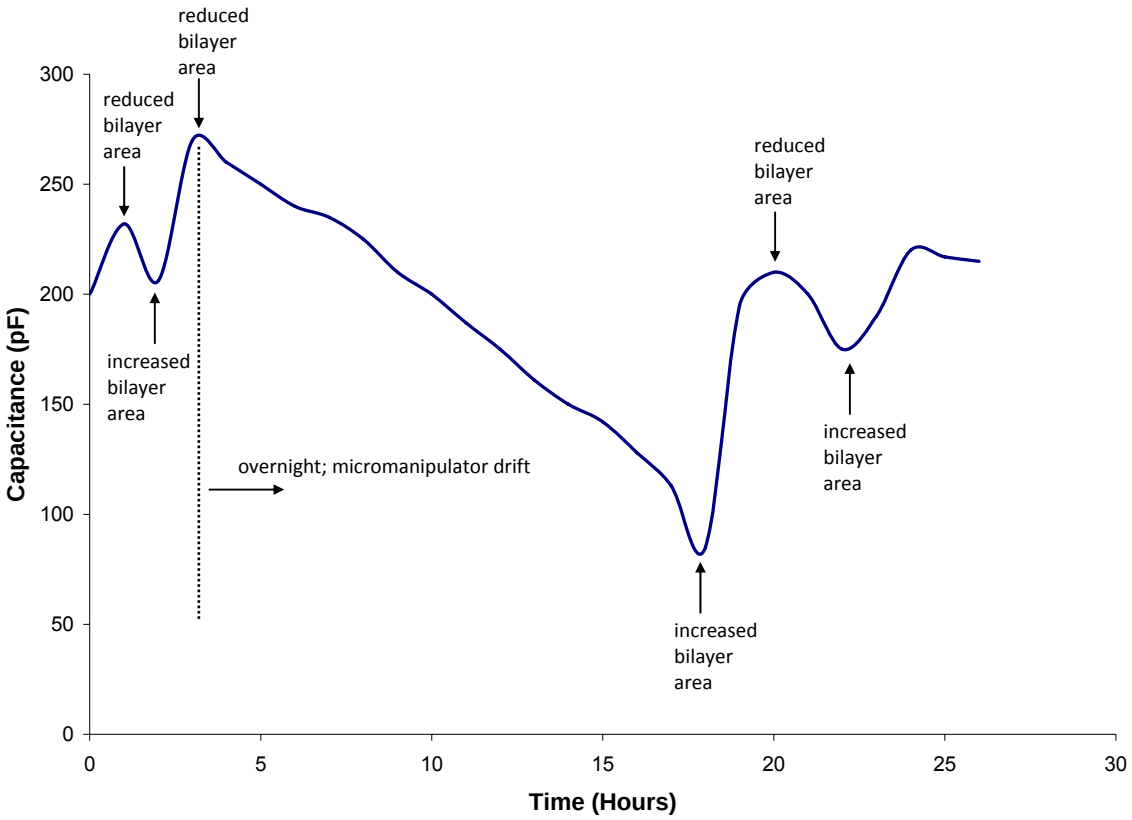

Figure 3.2 Asymmetric Droplet Interface Bilayer Survival. The capacitance over time of an asymmetric droplet interface bilayer with a positively-charged leaflet and negatively-charged leaflet. The applied voltage was +100 mV. The bilayer capacitance was modulated with micromanipulators during the experiment as indicated. The experiment concluded after 26 hours not because of bilayer rupture, but because the apparatus was needed for another experiment.

3.2.2. Lipid Asymmetry in a-DIBs

Cell membrane asymmetry is maintained by a combination of activities: (1) *flip*, an energy-dependent movement of phospholipids from the outer leaflet to inner leaflet, (2) *flop*, an energy-dependent movement of phospholipids from the inner leaflet to outer leaflet, and (3) *scramble*, a calcium-dependent, energy-independent, nonspecific randomization of lipids across the bilayer. Although the dynamic movement of lipids between membrane leaflets is well-established, the mechanisms and agents that promote and regulate flip-flop remain unclear (Daleke, 2007; Kol et al., 2004; Pomorski & Menon, 2006). Asymmetric DIBs that model the composition of natural bilayers may

be coupled with simple confocal fluorescence assays or radiolabeled lipids to study proteins that have been implicated in flip-flop mechanisms. The ability to separate and independently study the constituent leaflets of DIBs enables more accurate measurements of lipid transfer as a function of time.

We formed asymmetric droplet interface bilayers between droplets with fluorescently-tagged lipids and droplets with no fluorescently-tagged lipids (Fig. 3.3). We separated these droplet pairs after varying amounts of time up to 24 hours. We were unable to detect transfer of fluorescence across the bilayer and onto the untagged, recipient droplet, suggesting that bilayer asymmetry is maintained long enough to study the effects of bilayer composition on ion channel behavior. This is further confirmed by the differences in protein behavior observed in asymmetric bilayers as described in Section 3.2.3. After one week however, transfer of fluorescence was observed (Fig. 3.4).

Studies employing fluorescent or spin-labeled lipid probes have revealed that spontaneous transmembrane flip-flop of phospholipids is slow, with a half-life on the order of hours to days (Boon & Smith, 2002; Devaux et al., 2002), which supports our observations. However, the bulky fluorescent tags will affect flip-flop rates, and we are currently exploring the use of smaller nitro-benzoxadiazol (NBD) tail-labeled lipids. The smaller fluorescent tags on these lipids should provide a more accurate picture of intrinsic lipid flip-flop. It is important to note that the intrinsic rate of flip-flop for several phosphocholines was recently measured by sum-frequency vibrational spectroscopy and their half-lives were found to be on the order of minutes to hours over a wide range of temperatures (Liu & Conboy, 2005). Moreover, the addition of a fluorescent group reduced the rate of flip-flop by an order of magnitude. Further studies on the persistence of bilayer asymmetry are necessary.

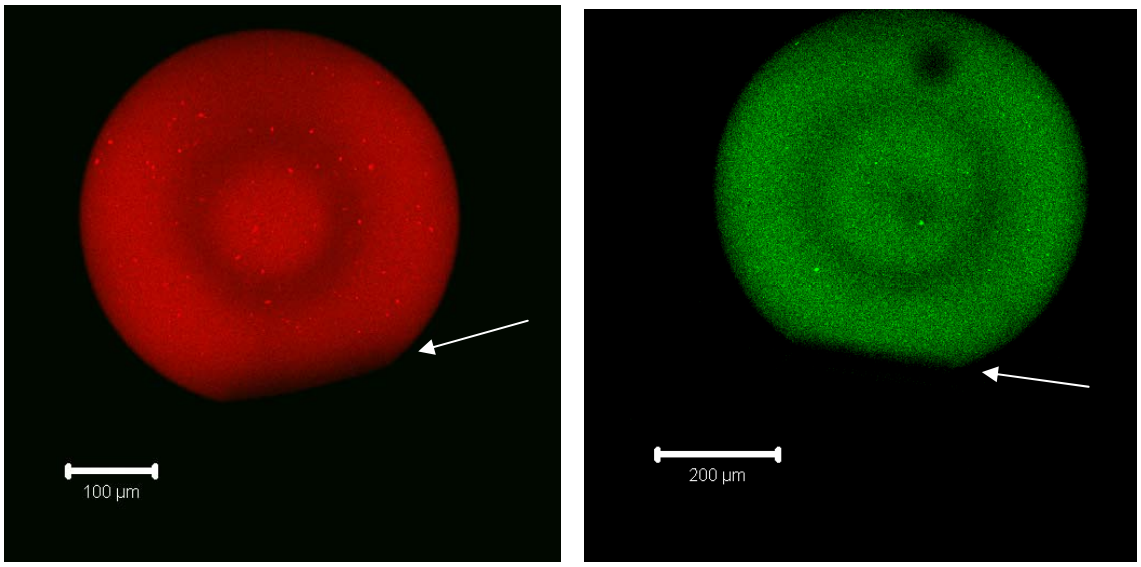

Figure 3.3 Transfer of Fluorescently-Labeled Lipids across a-DIBs over 24 Hours. Scanning confocal fluorescence images (*z*-projections) of 100 nL droplets 24 hours after bilayer formation. Droplets are submerged in hexadecane. *Left:* The top droplet contains 2 mM DPhPC vesicles doped with 1 mol% 1,2-dipalmitoyl-*sn*-glycero-3-phosphoethanolamine-N-(lissamine rhodamine B sulfonyl) and the bottom droplet (dark) contains 2 mM DPhPC vesicles only. The arrow indicates the bilayer. *Right*: The top droplet contains 2 mM DPhPC vesicles doped with 2% 1,2-dioleoyl-*sn*-glycero-3-phosphoethanolamine-N-(carboxyfluorescein) and the bottom droplet (dark) contains 2 mM DPhPC vesicles only. The arrow indicates the bilayer.

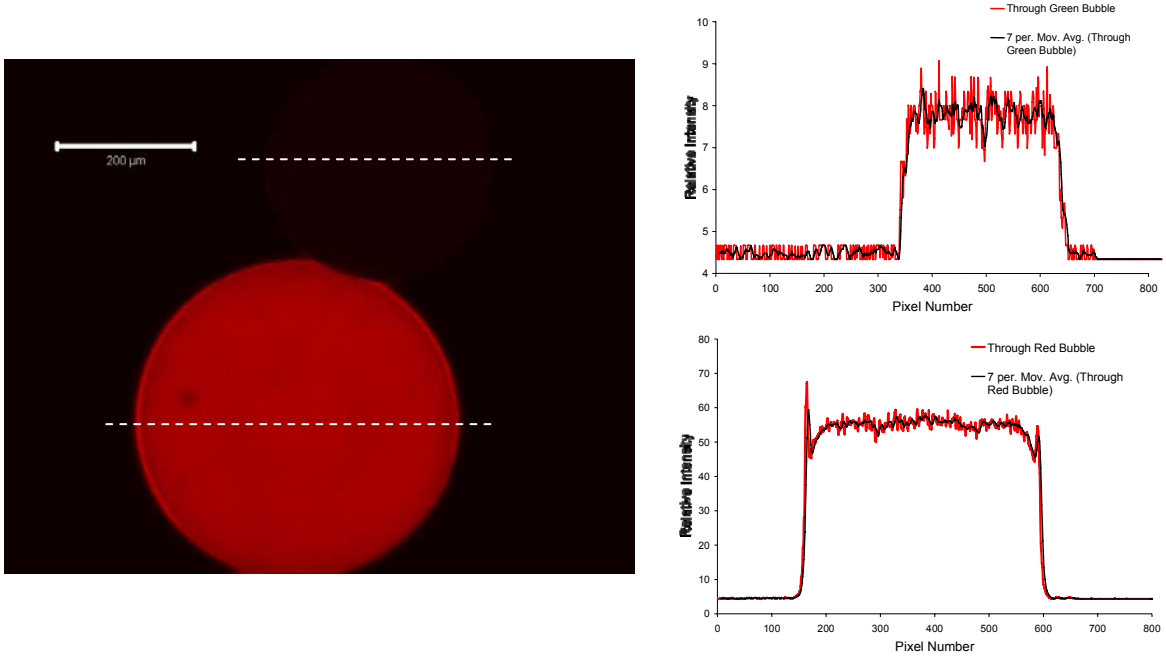

Figure 3.4 Transfer of Fluorescently-Labeled Lipids across a-DIBs over 1 Week. *Left:* Initially, the top "recipient" droplet contained 2 mM DPhPC vesicles doped with 2% 1,2-dioleoyl-*sn*-glycero-3-phosphoethanolamine-N-(carboxyfluorescein) and the bottom "donor" droplet contained 2 mM DPhPC vesicles doped with 1 mol% 1,2-dipalmitoyl-*sn*-glycero-3-phosphoethanolamine-N-(lissamine rhodamine B sulfonyl). Droplets are submerged in hexadecane. This scanning confocal fluorescence image (*z*-projection) was taken one week after DIB formation. Transfer of red fluorescence is apparent. *Right:* Plots of relative intensity (543 nm laser only) along a single line through each droplet. Note that the *y*-axis scales are different.

While some studies support the idea that specific, identifiable proteins are responsible for facilitating ATP-independent phospholipid flip-flop (Vehring et al., 2007), others argue that lipid transbilayer migration is not governed by proteins directly, but rather by membrane defects introduced by transmembrane helices (Kol et al., 2002). In support of the latter view, Anglin et al. used sum-frequency vibrational spectroscopy to show that gramicidin A, a non-ribosomal, pore-forming peptide, increases phosphocholine flip-flop rates by up to ten times (Anglin et al., 2007). We have begun our own studies on how transmembrane helices affect lipid flip-flop rates using a-DIBs composed of NBD-labeled lipids (Fig. 3.5). Future work will involve determination of how various membrane elements influence flip-flop rates, investigation of temperature effects, and careful controls to account for lipid transfer through the oil bath rather than the bilayer.

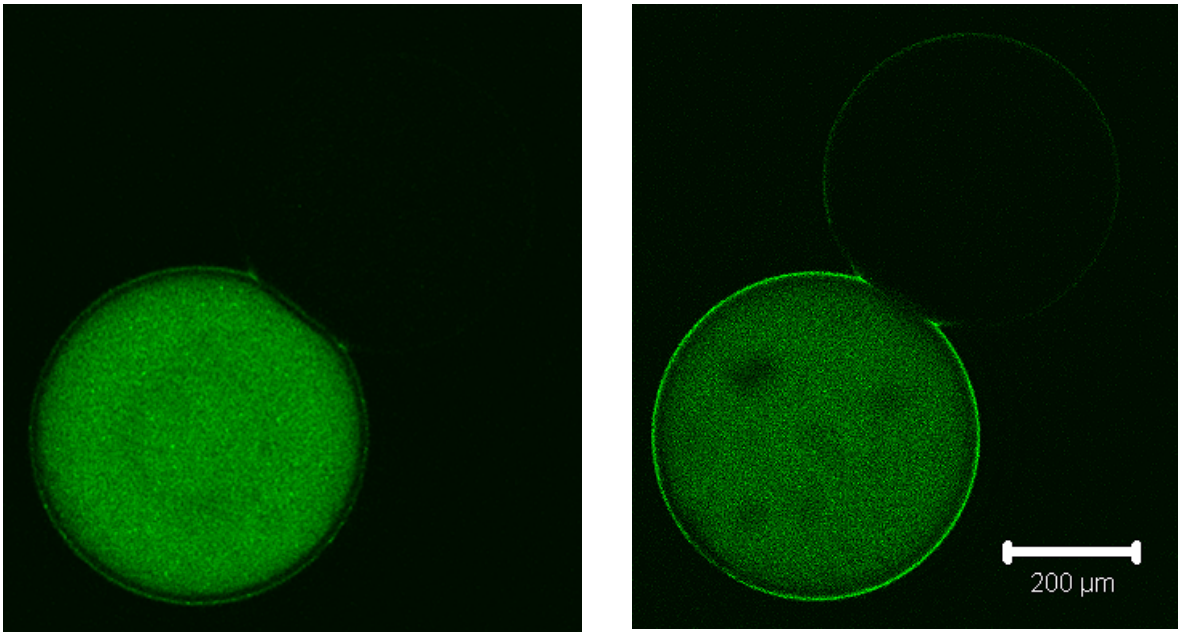

Figure 3.5 Transfer of NBD-Labeled Lipids across a-DIBs with Gramicidin A in Membranes. Scanning confocal fluorescence images (*z*-slices) of 100 nL droplets immediately after bilayer formation (*Left*) and after 20 hours (*Right*). Bottom-left droplet contains 2 mM DPhPC vesicles doped with 2 mol% 1-palmitoyl-2-{12-[(7-nitro-2-1,3-benzoxadiazol-4-yl)amino]dodecanoyl)-*sn*-glycero-3-phosphocholine. Top-right droplet (dark) contains 2 mM DPhPC vesicles. Both droplets contain 10 µg/mL gramicidin A in methanol. Droplets are submerged in hexadecane. Transfer of fluorescence to the surface of the recipient droplet is evident.

3.2.3. Behavior of Ion Channels in a-DIBs

Asymmetric DIBs provide an optimal platform for studying the behavior of transmembrane pores and channels with respect to bilayer leaflet composition. Both α-helical and β-barrel membrane proteins have been successfully reconstituted in a-DIBs.

3.2.3.1. Outer Membrane Protein G from *Escherichia coli*

Outer membrane protein G (OmpG) is a monomeric porin from *Escherichia coli*; the structure of OmpG has recently been elucidated by X-ray diffraction and NMR spectroscopy (Liang & Tamm, 2007; Subbarao & van den Berg, 2006; Yildiz et al., 2006). The 14 strands in OmpG's β-barrel are connected by negatively-charged loops on the extracellular side and short turns on the periplasmic side. It was recently shown that movements of the extracellular loops cause the porin to spontaneously fluctuate among open, partially closed, and fully closed states, a behavior known as gating (Chen et al., 2008; Conlan & Bayley, 2003). Spontaneous gating activity can be quantified by using the mean gating probability (P_{gating}), which is defined as the time a pore spends in partially or fully closed states divided by the open pore time.

When OmpG was inserted into a lipid-in DIB composed of the neutral lipid 1,2-diphytanoyl-*sn*-glycero-3-phosphocholine (DPhPC), we found that the observed P_{gating} was the same as that in a planar bilayer (Montal & Mueller, 1972) with the same lipid composition (compare 0/0* and 0/0 in Fig. 3.6 *B*). This observation indicates that the presence of vesicles does not alter the gating behavior of the protein. The buffering conditions used in all experiments were 10 mM HEPES, 200 mM KCl, pH 7.0.

We studied the effect of charged asymmetric bilayers on the spontaneous gating behavior of OmpG by forming a-DIBs with vesicles composed of 10 mol% DDAB in DPhPC and 10 mol% DPPG in DPhPC. The charges of the bilayer leaflets will be denoted by

"X/Y," where "X" is the leaflet charge on the side of protein insertion and "Y" is the charge on the opposing leaflet. In a typical electrophysiology experiment with OmpG in a-DIBs, bilayer formation is followed by spontaneous insertion of the protein into the bilayer (Fig. 3.7). If desired, the bilayer size can then be minimized to reduce the probability of further insertion.

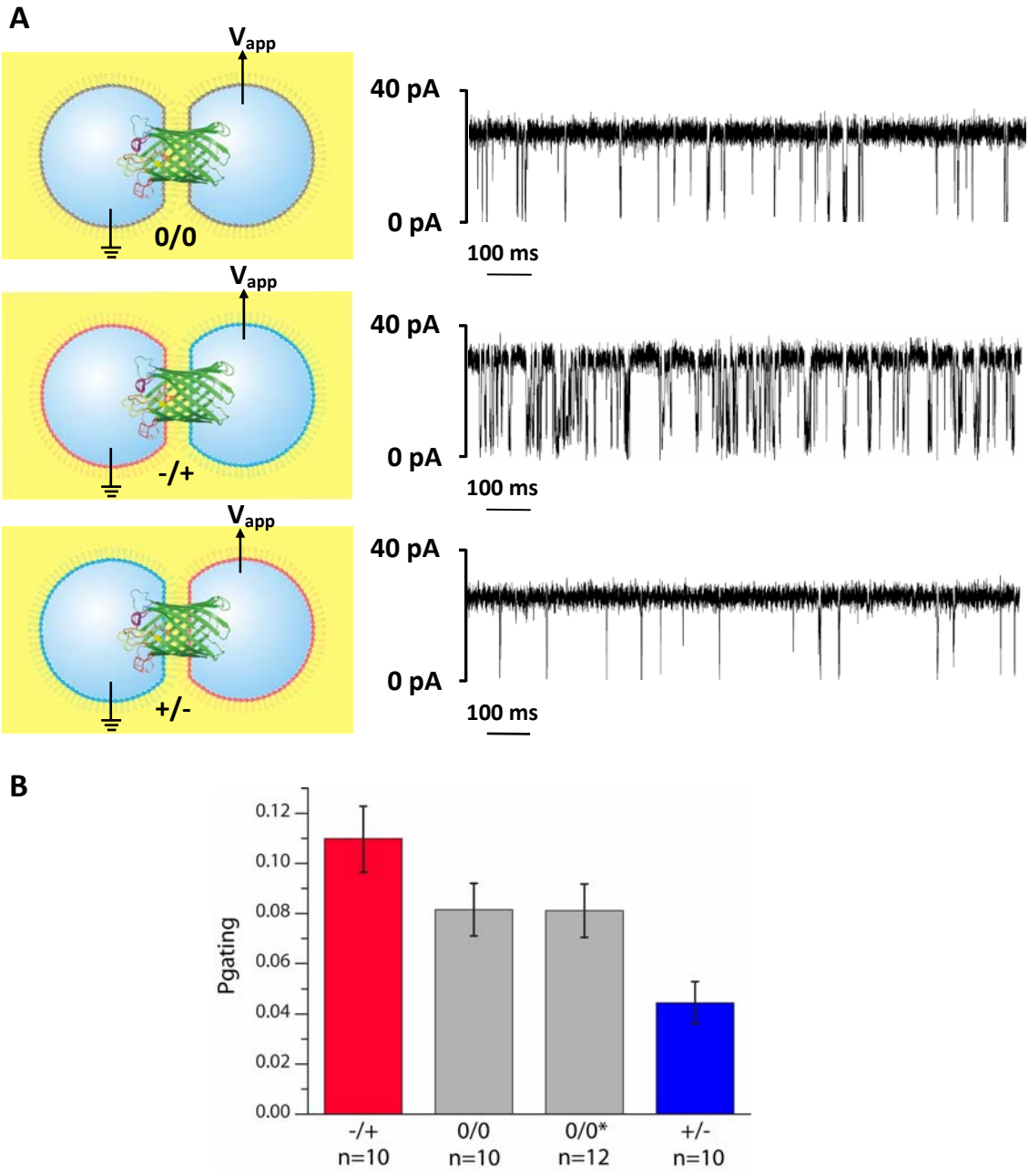

Figure 3.6 OmpG Behavior in Symmetric and Asymmetric Bilayers. *(A)* Current traces showing OmpG gating: *Top:* neutral DIB (0/0), *Middle:* insertion from the negative side of the asymmetric DIB (-/+), and *Bottom:* insertion from the positive side of the asymmetric DIB (+/-). A potential of +50 mV was applied.

The buffer used was 10 mM HEPES, 200 mM KCl, pH 7.0. Protein was in the grounded droplets. *(B)* Comparison of mean gating probabilities (P_{gating}) of OmpG in a symmetric neutral planar bilayer (0/0*), symmetric neutral lipid-in DIB (0/0), and asymmetric DIBs (-/+ and +/-). P_{gating} is defined as the ratio of the time a pore resides in partially or fully closed states to the open pore time. Error bars represent one standard error and are based on at least ten pores.

When OmpG inserted from the negative side of the asymmetric bilayer (-/+), the frequency of gating increased relative to the neutral bilayer (0/0) (Fig. 3.6, $P_{gating}^{-/+} > P_{gating}^{0/0}$, 95% confidence). On the other hand, when the protein inserted from the positive side of the a-DIB (+/-), the frequency of gating decreased relative to the neutral bilayer (0/0) (Fig. 3.6, $P_{gating}^{+/-} < P_{gating}^{0/0}$, 99% confidence). The insertion of OmpG from opposite sides of the charged a-DIB yielded significantly different gating behaviors (Fig. 3.6, $P_{gating}^{-/+} > P_{gating}^{+/-}$, > 99% confidence).

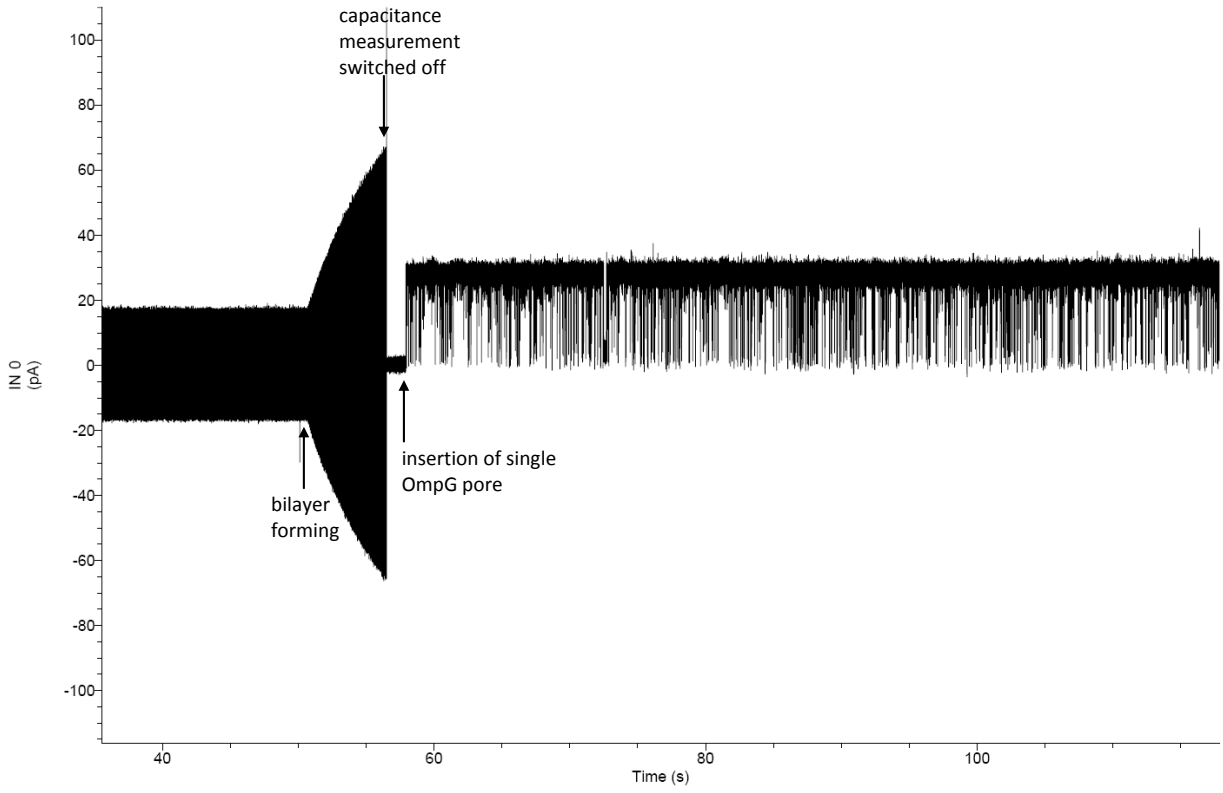

Figure 3.7 Electrophysiology Recording of OmpG in a Charged a-DIB. Formation of the a-DIB is followed by spontaneous pore insertion.

When the orientation of OmpG in the bilayer is such that the extracellular loops are on the side of insertion (grounded droplet), the open pore conductance level is quieter at positive potentials relative to that at negative potentials (Chen et al., 2008). We found that OmpG always inserted into DIBs with this orientation. This is unlike experiments using planar bilayers, where both pore orientations are observed. Therefore, our results suggest that the +/- bilayer interacts with the negatively-charged loops such that the positively-charged leaflet reduces gating. In contrast, the -/+ bilayer interacts with the negatively-charged loops such that the negatively-charged leaflet increases gating.

3.2.3.2. α-hemolysin from *Staphylococcus aureus*

α-hemolysin (αHL) is a heptameric, 14-strand β-barrel, transmembrane pore from *Staphylococcus aureus* (Song et al., 1996). Purified αHL heptamers were reconstituted in charged asymmetric bilayers consisting of a 5 mol% DDAB in DPhPC leaflet opposed to a 5 mol% DPPG in DPhPC leaflet. The buffering conditions were 10 mM HEPES, 200 mM KCl, pH 7.0 and the protein inserted from the electrically grounded side of the bilayer. At positive potentials, there were no significant differences in the current versus voltage characteristics of αHL among the bilayer types (0/0, +/-, -/+; Fig. 3.8). At negative potentials, both asymmetric bilayer types (-/+, +/-) reduced the current through αHL relative to the neutral bilayer (0/0). This effect increased with the magnitude of the applied potential.

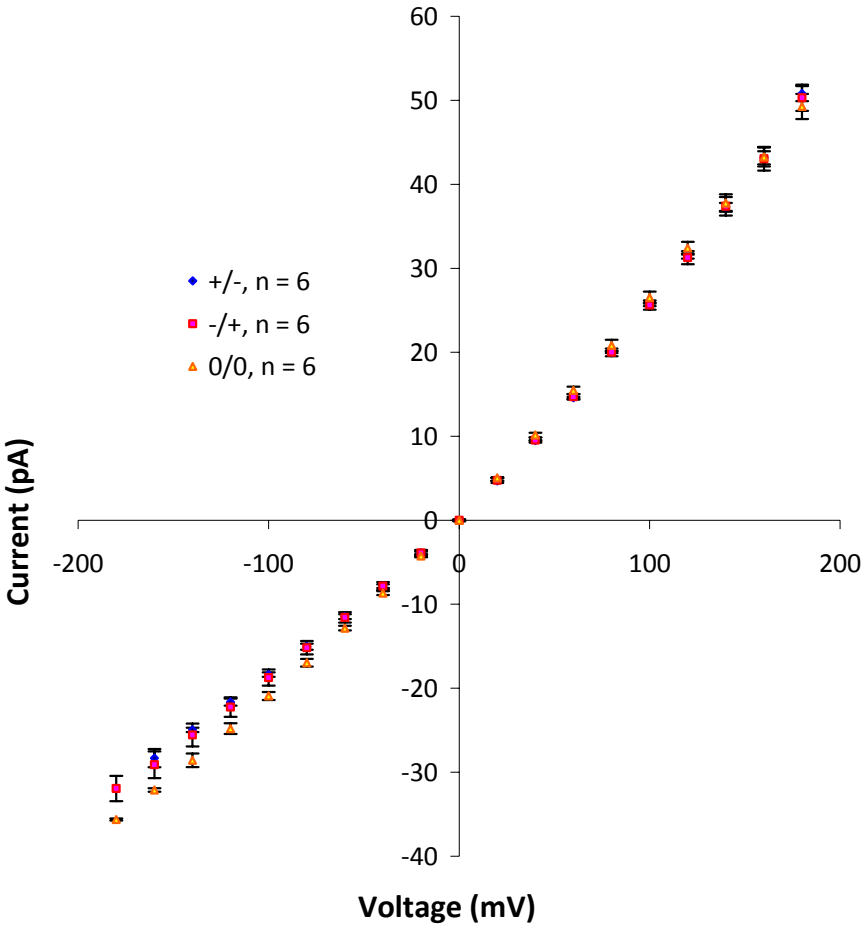

Figure 3.8 I-V Curves of αHL as Function of Bilayer Composition. αHL heptamer was reconstituted in a symmetric, neutral bilayer, and from either side of a charged a-DIB with a positively-charged leaflet and a negatively charged leaflet.

3.2.3.3. Kcv Potassium Channel from PBCV-1 Chlorella Virus

The chorella virus PBCV-1 was the first virus discovered to encode a functional potassium channel, Kcv (Gazzarrini et al., 2003). The α-helical Kcv tetramer is only 94 amino acids and includes a pore-region module that is typical of all known potassium channels. We reconstituted Kcv tetramers in charged a-DIBs with a positive leaflet (10 mol% DDAB in DPhPC) opposing a negative leaflet (10 mol% DPPG in DPhPC). The buffering conditions were 10 mM HEPES, 200 mM KCl, pH 7.0. Potassium channels transition between non-conducting and conducting states—a behavior known as gating (Fig. 3.9). We found that Kcv was able to insert from either side of the charged bilayer,

and exhibited significant negative rectification (Fig. 3.9; e.g., open conductance levels at negative potentials are less than that at corresponding positive potentials) (Hertel et al., 2006). At negative applied potentials (protein in electrically grounded droplet), the I-V characteristics of Kcv in charged a-DIBs (+/-, -/+) did not differ significantly from that in symmetric, neutral DIBs (0/0; Fig. 3.10). At positive potentials, the current through Kcv was higher in asymmetric bilayers (+/-, -/+) relative to the neutral bilayer (0/0), but more experiments are needed to confirm this observation.

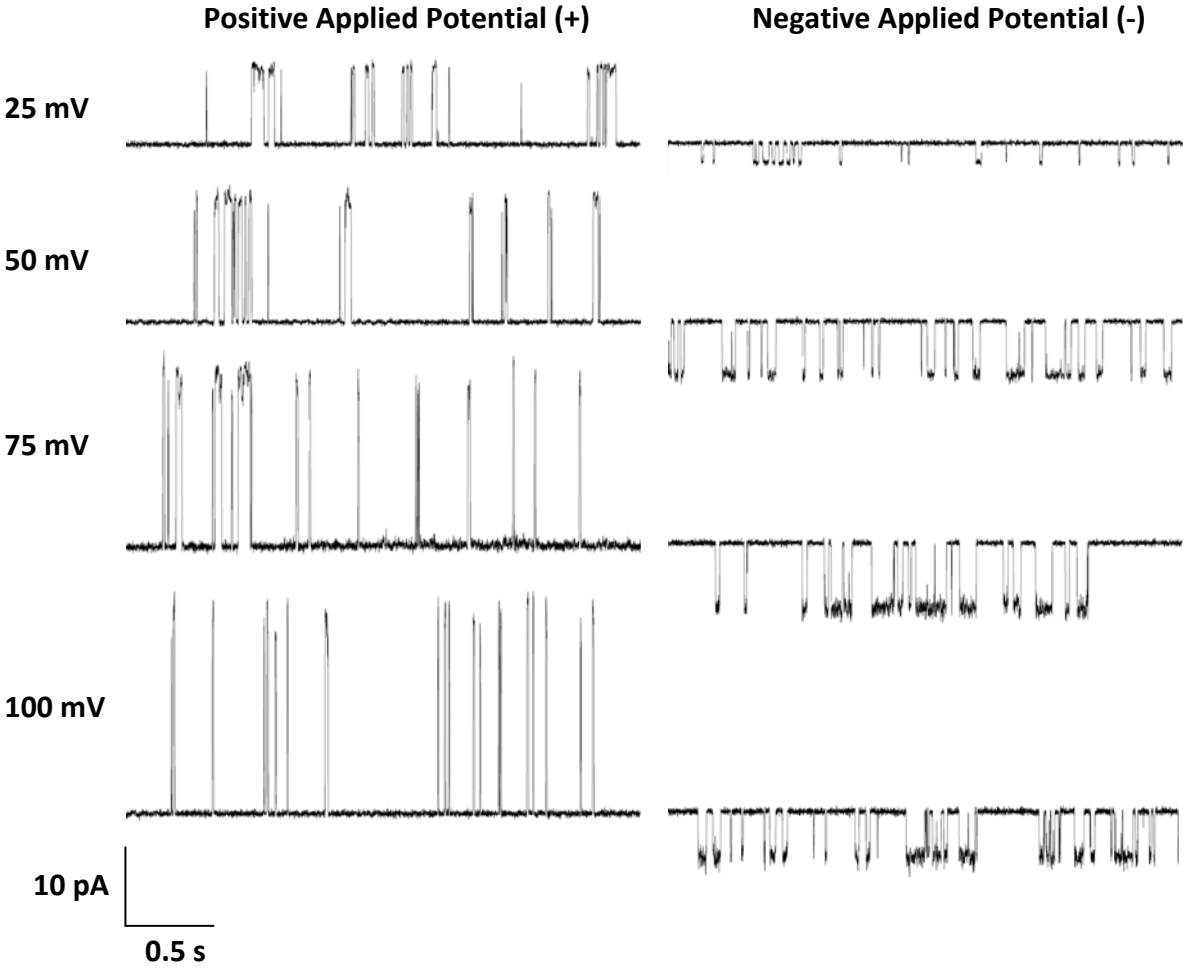

Figure 3.9 Kcv Gating Behavior as Function of Applied Voltage in +/- a-DIB. Kcv tetramer was reconstituted in a charged a-DIB with a positive leaflet (10 mol% DDAB in DPhPC) and negative leaflet (10 mol% DPPG in DPhPC). The protein was in the droplet containing DDAB and therefore inserted from the positive side of the bilayer. The protein-containing droplet was electrically grounded and the working potential was applied to the opposing droplet. Channel gating at -100, -75, -50, -25, +25, +50, +75, and +100 mV is illustrated.

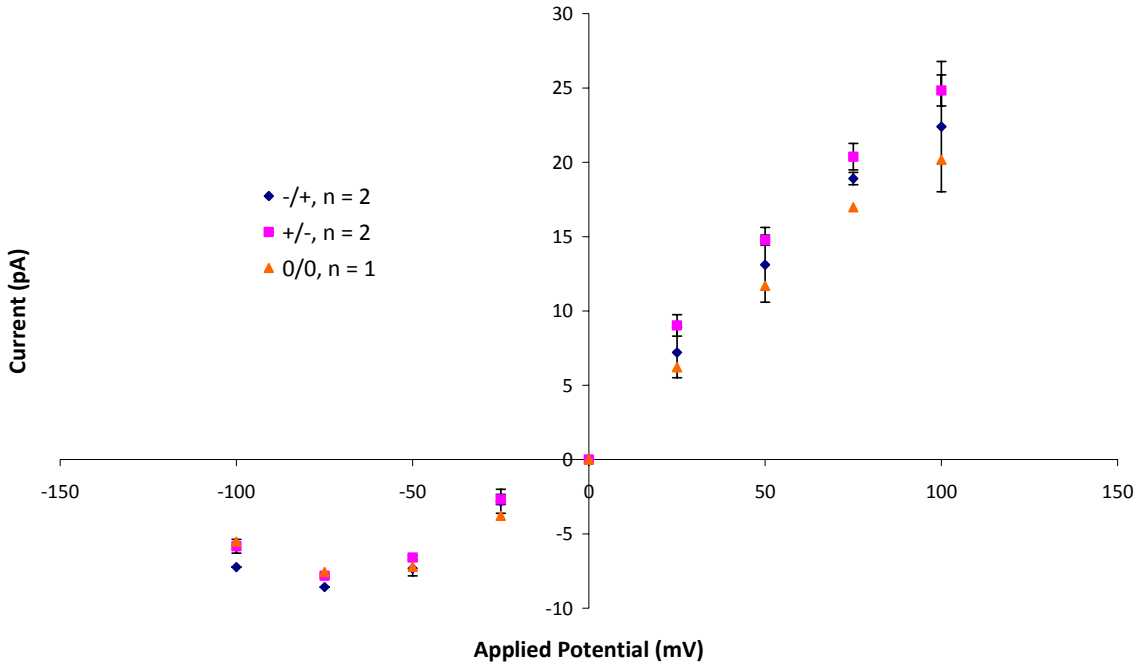

Figure 3.10 I-V Curves of Kcv as Function of Bilayer Composition. Kcv tetramer was reconstituted in a symmetric, neutral bilayer, and from either side of a charged a-DIB with a positively-charged leaflet and a negatively charged leaflet.

3.3. Methodology

3.3.1. Vesicle Preparation

Lipid mixtures were dissolved in pentane or chloroform (0.5 mL, 50 mg/mL), transferred to an 8 mL glass vial and dried under vacuum for two hours. The lipids used were 1,2-diphytanoyl-sn-glycero-3-phosphocholine (DPhPC, Avanti Polar Lipids, Alabaster, AL), with 1-10 mol% of an additional lipid, including fluorescent lipids such as 1,2-dioleoyl-*sn*-glycero-3-phosphoethanolamine-N-(carboxyfluorescein) and 1,2-dipalmitoyl-*sn*-glycero-3-phosphoethanolamine-N-(lissamine rhodamine B sulfonyl), and charged lipids such as dimethyldioctadecylammonium (bromide salt) (DDAB) and 1,2-dipalmitoyl-*sn*-glycero-3-[phospho-*rac*-(1-glycerol)] (sodium salt) (DPPG) (Avanti Polar Lipids). Buffer (10 mM HEPES, 200 mM KCl, pH 7.06; 5 mL) was added to the dried lipid mixture and vortexed for ten seconds. The solution was subjected to five freeze-thaw

cycles. The lipid-buffer suspension was then extruded (LIPEX™ Extruder, Northern Lipids, Burnaby, Canada) twice through 0.1 μm VCTP Isopore Membrane Filters (Millipore, Billerica, MA). The extruded sample was diluted with buffer to a volume of 12 mL, yielding a 2 mg/mL lipid solution. The vesicle solutions were divided into aliquots of 1 mL and stored at 4°C for up to one month.

3.3.2. Lipid-In Droplet Interface Bilayers

A Perspex chamber (700 μL) was filled with hexadecane oil (Sigma Aldrich, Dorset, UK). Two Ag/AgCl electrodes were attached to independent micromanipulators (NMN-21, Narishige) and the tips rendered hydrophilic by coating with 5% w/v low melt agarose in buffer (10 mM HEPES, 200 mM KCl, titrated to pH 7.0 with KOH). One electrode was connected to the grounded end of a patch clamp headstage (Axopatch 200B, Axon Instruments, Union City, CA) and the other was connected to the working end. Positive current flow is defined as cations moving from the working end towards the grounded end of the headstage and anions flowing in the opposite direction. The electrodes were submerged in the oil bath and droplets (200 nL) of the vesicle solution were attached directly to the electrodes using a pipette (P2 Gilson Pipetman, Anachem, Bedfordshire, UK). After an incubation period of five minutes, the droplets were brought into contact to form droplet interface bilayers (DIBs). The capacitance values of bilayers were determined by applying a triangular voltage wave with a function generator.

3.3.3. Scanning Confocal Fluorescence Imaging[5]

Droplet pairs were formed from vesicle solutions in a hexadecane reservoir on a glass coverslip and imaged using a Zeiss LSM 5 Exciter Laser scanning confocal microscope at 10x magnification. Carboxyfluorescein-tagged lipid (1,2-dioleoyl-*sn*-

[5] Performed in collaboration with Dr. Bríd Cronin.

glycero-3-phosphoethanolamine-N-(carboxyfluorescein), Avanti Polar Lipids) was imaged with 488 nm (Ar-ion) excitation, HFT 488/543/633 dichroic, and the resulting emission was collected through a band pass filter, 505-530 nm. Lissamine rhodamine-tagged lipid (1,2-dipalmitoyl-*sn*-glycero-3-phosphoethanolamine-N-(lissamine rhodamine B sulfonyl, Avanti Polar Lipids) was imaged by excitation with the 543 nm line of a HeNe laser, HFT 488/543/633 dichroic, and the resulting emission collected using a 560 nm long pass filter. The pinhole size was 78 μm for each channel.

3.3.4. Electrophysiology

The electrodes were connected to a patch-clamp amplifier (Axopatch 200B). The Perspex chamber and amplifying headstage were enclosed in a metal box, which served as a Faraday cage. Currents were filtered with a low-pass Bessel filter (80 dB/decade) with a corner frequency between 500 Hz and 2 kHz and digitized with a DigiData 1320 A/D converter (Axon Instruments) at a sampling frequency of 10-50 kHz.

In the OmpG experiments, we performed at least ten independent trials for each bilayer composition type. Fresh vesicle and protein solutions were prepared from stock solutions and a new bilayer was formed for each experiment. The protein was not directly incorporated into the vesicles, and was instead solubilized by surfactants and added to the vesicle solution immediately prior to droplet formation. Each independent recording of a single pore in the bilayer was at least five minutes in duration. During this period of time, the single pore was observed to gate continuously at an applied potential of +50 mV.

Spontaneous OmpG gating activity was quantified using Clampfit software (Version 9.2, Axon Instruments, Union City, CA). The region of interest in each recording was selected with cursors and a single-channel search was performed with Level 0 at the

bottom of the open conductance level and Level 1 set to 15 pA below Level 0. Levels were updated automatically to account for small movements in the open conductance level. Once the search was complete, P(open) event analysis was performed to obtain the desired P_{gating} parameter. For each recording, a minimum of 2500 events were analyzed.

3.3.5. Expression, Purification, and Refolding of Outer Membrane Protein G[6]

The pT7-OmpG (WT) plasmid was transformed into E. coli PC2889 cells [BL21(DE3)ΔlamB ompR] (Conlan et al., 2000). Cells were grown in LB medium (0.5 L) at 37 °C until the OD 600 reached 1.0. IPTG (0.5 mM, final concentration) was added and the cells were further cultured for three hours before harvesting. Pellets from the culture were resuspended in 50 mM Tris·HCl, pH 8.0, 200 μg/mL lysozyme and 1 mM EDTA (30 mL) and incubated at room temperature for 30 min. DNase I (5 μL, 2,000 U/μL) and 2 mM $MgCl_2$ (final concentration) were added to the mixture to decrease the viscosity. The lysate was centrifuged at 13,000 rpm for 30 min. The OmpG-containing pellet was washed once with 50 mM Tris·HCl, pH 8.0, 1.5 M urea (30 mL). The pellet was then dissolved in denaturation buffer (50 mL, 50 mM Tris·HCl, pH 8.0, 8 M urea) and passed through a 0.22 μm filter. The filtered extract was loaded onto a Q-Sepharose FPLC column and eluted with a 0 to 0.5 M NaCl gradient over 30 min in denaturation buffer. Purified OmpG was refolded by dilution with refolding buffer (20 mM Tris·HCl, pH 9.0, 3.25% OG (n-octyl β-D-glucopyranoside)) until the final urea concentration reached 3.0 M. The refolding solution was incubated at room temperature overnight and the refolding efficiency was determined by SDS-PAGE analysis (Chen et al., 2008). The sample was sequentially concentrated and diluted with a Centricon size-exclusion filter

[6] Performed by Dr. Min Chen.

with a 10 kDa cutoff (Fisher Scientific, UK) to exchange the buffer to 50 mM Tris·HCl, pH 8.0, 1% OG. The protein was then concentrated to ~0.5 mg/ml and stored at -20°C.

3.3.6. *In Vitro* Transcription and Translation, and Purification of Kcv[7]

The WT Kcv gene in the pT7-SC1 vector with ampicillin resistance was a gift from Stephen Cheley.

Protein was expressed using a cell-free coupled in-vitro transcription and translation system (IVTT) by using an *E. coli* T7-S30 extract optimized for circular DNA (No. L1130, Promega Corporation, Madison, WI). The complete 1 mM amino acid mixture (5 µL) and premix solution (20 µL), provided with the kit, were mixed with [L-^{35}S] methionine (4 µL, 1175 Ci/ mmol, 10 mCi/ mL, MP Biomedicals), plasmid DNA (8 µL, 400 ng/µL) and T7-S30 extract (15 µL) supplemented with rifampicin (1 µg/mL final concentration), and incubated at 37°C for 1 hour. Expressed protein was analyzed by SDS PAGE and visualized by exposure to film (Kodak BioMax MR-1).

To purify protein for single channel recordings, a 50 µL IVTT reaction was loaded onto a 10% Tris-HCl SDS polyacrylamide gel. The gel was dried under vacuum at room temperature and then exposed to film. The band corresponding to the tetramer was cut from the gel and rehydrated in 300 µL 10 mM HEPES, pH 7.4. The paper backing of the gel was removed; the rehydrated gel piece was crushed with a small pestle (Bellco Glass Inc), transferred to a 0.2 µm cellulose acetate microfilter tube (Rainin) and centrifuged at 25,000g for 30 minutes. The eluted protein was stored at -80°C. A sample of the purified protein was re-run on a polyacrylamide gel to ensure the tetramers had not dissociated into monomers.

[7] Performed by Dr. Amy Mason.

Chapter 4

Double Bilayers for the Study of Dual-Membrane Spanning Proteins[8]

4.1. Introduction

4.1.1. Intercellular Gap Junctions: Social Networking for Cells

Important protein complexes that span two membranes are found in nature and include the secretory apparatus of gram negative bacteria (Piddock, 2006) and the nuclear pores of eukaryotes (Alber et al., 2007a; Alber et al., 2007b; Evans & Martin, 2002). Many cells in animal tissues communicate with each other via gap junctions, which mediate the passage of chemical or electrical signals from one cell to its partner (Alberts et al., 2002). Two cells connected by gap junctions will exhibit a uniform gap of 2-4 nm (Alberts et al., 2002). Each gap junction is formed by the linkage of a connexon (hemichannel) from each cell in the communicating pair (Fig. 4.1). Each connexon consists of a hexamer of connexins, which are four pass-transmembrane proteins. As of

[8] A description of this work is included in BAYLEY, H., CRONIN, B., HERON, A. J., HOLDEN, M. A., HWANG, W. L., SYEDA, R., THOMPSON, J. R. & WALLACE, M. I. (2008). Droplet interface bilayers. In prep.

2002, there is no X-ray diffraction crystal structure of either pre-docked or undocked connexons (Muller et al., 2002).

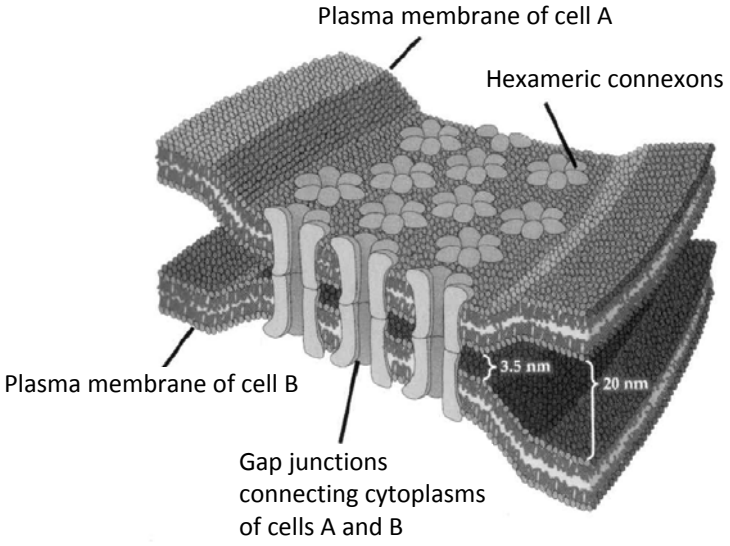

Figure 4.1 Model of gap-junction structure based on X-ray diffraction and electron microscopy. Adapted from (Evans & Martin, 2002).

In tissues that contain electrically excitable cells, e.g., nerve cells, gap junction coupling enables action potentials to spread rapidly from cell to cell, without the delay associated with chemical synapses. In vertebrates, electrical coupling through gap junctions synchronizes the contractions of heart muscle cells and smooth muscle cells in the intestine. In tissues without electrically excitable cells, gap junctions allow cells to share small metabolites and ions, thereby providing a mechanism for coordinating the activities of individual cells that make up the tissue and smoothing out random fluctuations in small molecule concentrations.

Connexins are known or suspected to be involved in a wide range of biological processes including cardiac development, hematopoiesis, regeneration, fertility, immune system function, protection from oxidative stress, and ocular lens transparency (Harris, 2001). Defects in molecular movement through connexin channels may induce

disease, as well as abnormal development and physiology (Peracchia, 2000). The prevalence of gap junctions and hemichannels in a wide range of tissues is well established. It is therefore not surprising that mutations in connexin genes are responsible for many diseases and pathological conditions—so called "connexinopathies."

Cell coupling via gap junctions is important for vertebrate embryogenesis (Alberts et al., 2002). From an early stage, most cells are electrically coupled to one another. As groups of cells begin to differentiate, they uncouple from surrounding tissue. However, cells within each group remain coupled with each other and thus tend to behave as a cooperative assembly, all following a similar development pathway. The normal development of ovarian follicles is also dependent on gap-junction mediated communication between the oocyte and the surrounding granulosa cells (Alberts et al., 2002). Mutations in the relevant connexin gene (Cx37) leads to infertility.

Different combinations of three connexins (Cx40, Cx43, and Cx45) are expressed in various subsets of cardiac cells (Alex et al., 2005). In a healthy heart, gap junctions created from these different connexin combinations form cellular communication pathways that enable precisely orchestrated patterns of current flow that govern the normal heart rhythm. Substantial remodelling of connexin expression and gap junction organization is a major feature of human heart disease in which there is associated arrhythmia (Severs et al., 2004). A decrease in ventricular Cx43 levels is linked to congestive heart failure (Severs et al., 2004). Cx43 is the predominant connexin in ventricular myocardium and plays a critical role in cardioprotection afforded by ischemic preconditioning (Boengler et al., 2006).

Gap junctions play an important role in hearing and mutations in connexin genes are linked with a high incidence of human deafness (Zhao et al., 2006). Pathogenesis is primarily located in the cochlea, where gap junctions provide extensive networks between non-sensory cells.

The strong correlation between a bone's architecture and the mechanical forces it experiences is most likely attributed to the osteocyte, which is posited to serve as a "mechanostat" by detecting mechanical load and structurally adapting the bone matrix to counter it. Nevertheless, osteocytes can neither form nor resorb bone, so it has been conjectured that they coordinate the actions of other cells such as osteoblasts. It was recently shown that this control is dependent on communication via gap junctions (Taylor et al., 2007).

4.1.2. Studying Gap Junctions

Understanding the properties and mechanisms of gap junction-mediated electrical and chemical signalling both under normal and pathological conditions remains an important basic science and medical challenge. However, the intercellular structure of gap junction channels makes them difficult to study and requires analytical techniques different from those applied to channels that only span a single bilayer.

4.1.2.1. Chemical Signaling

Several techniques have been applied to study the rate of intercellular secondary messenger signals through gap junctions. For example, injection of membrane-impermeable tracers such as Lucifer yellow or fluorescence recovery after photobleaching (FRAP) have been used to quantify rates of junctional molecular transfer (Wade et al., 1986). However, both methods have significant drawbacks. Microinjection disrupts intact cell membranes and FRAP requires a very strong laser light to rapidly

photobleach fluorophores, which may cause photo-damage to cells. Loss of cell membrane integrity can be a significant problem when studying the regulation of gap junction communication by cellular biochemical changes. Microfluidic devices that enable monitoring of junctional dye transfer between cell pairs have been demonstrated (Lee et al., 2005).

Recently, the permeability of gap junctions to secondary messengers cAMP and $InsP_3$ was quantified with fluorescence resonance energy transfer (FRET) microscopy (Hernandez et al., 2007; Ponsioen et al., 2007). Another group developed a new imaging technique called local activation of a molecular fluorescent probe (LAMP) for assaying molecular transfer rates across cellular gap junctions (Dakin et al., 2005). LAMP has many advantages over previous methods: it is non-invasive, provides good temporal resolution, requires minimal technical expertise, enables multiple quantitative rate measurements of the same cell pair, and allows multi-color imaging.

4.1.2.2. Electrical Signaling

Most investigations of the electrical conduction properties of gap junctions are performed using dual whole-cell patch clamping (Fig. 4.2). There are considerable limitations with this method, not the least of which is the fact one must computationally compensate for the error (underestimation of junctional conductance and voltage sensitivity) that arises from the uncompensated series resistances (Harris, 2001). This process requires accurate estimation or measurement of the series resistance and membrane resistance. The larger the ratio of series resistance to junctional resistance, the more significant the error (Harris, 2001).

Reconstitution of junctional channels in an artificial double bilayer platform would be extremely valuable for both quantification of molecular transfer rates and

electrophysiology at the single channel level. Such a tool would provide us with much greater control over the study of gap junctions with fewer lurking variables and confounding technical issues. Nevertheless, it is difficult to bring two bilayers close enough to enable connexons to dock and form gap junctions. There have been at least two previous attempts to create such a platform with limited success (Brewer, 1991; Fisher et al., 1986).

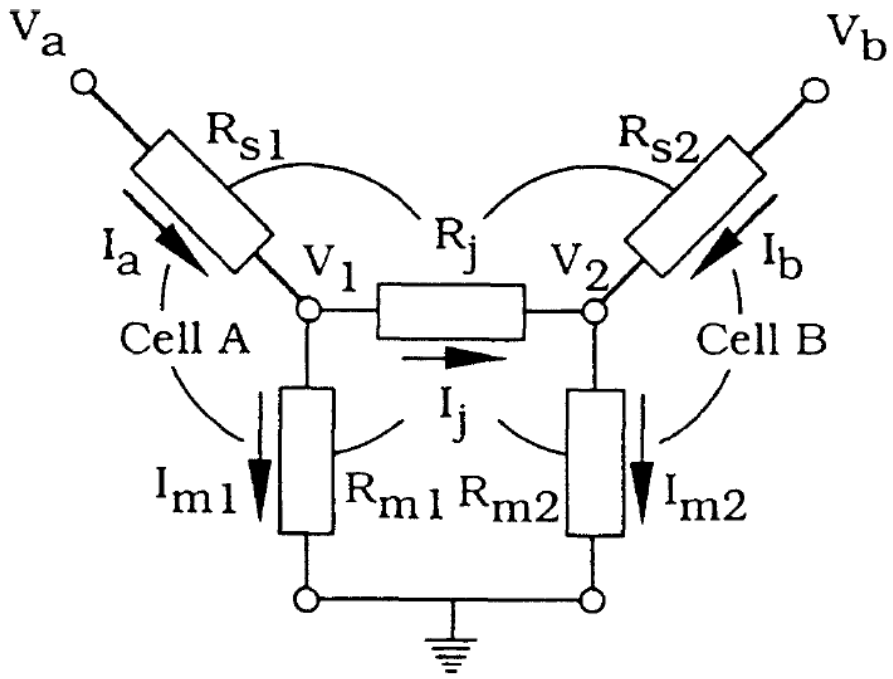

Figure 4.2 Equivalent circuit of dual whole-cell patch-clamp for recording junctional currents of two cells. R_s = series resistances including electrode resistances; R_m = resistances of non-junctional membranes, R_j = junctional resistance, and I_j = junctional current. Adapted from (Harris, 2001).

4.2. Results and Discussion

We have demonstrated an extension of DIB technology that enables the formation of two closely juxtaposed bilayers with the potential to study gap junctions and other dual-membrane spanning proteins. The double-bilayer platform consists of two aqueous droplets or agarose spheres (provides mechanical rigidity) brought into contact with opposite sides of a water film in a 10 mM DPhPC/hexadecane solution (Fig.

4.3 *A*). A stabilization period precedes assembly of the system to allow the droplets and each side of the water film to become coated with lipid monolayers.

The experimental chamber was designed such that an aqueous reservoir lies underneath the larger oil-lipid bath and is connected by a small slot (Fig. 4.3 *B*). A piece of 1.5-mm silver wire was pounded flat at one end and a large aperture (δ = 0.8 mm) was drilled on the flattened surface ("wand"). After treatment with NaClO, the wand was attached to a dipping mechanism that enabled the wand to slide through the slot into the aqueous reservoir (Fig. 4.3 *C*). When the wand was brought back through the slot into the oil-lipid bath, a thin water film remained across the aperture. Two additional Ag/AgCl electrodes within either an aqueous droplet or an agarose sphere were submerged in the oil-lipid bath and connected to micromanipulators. After sufficient stabilization, the droplets (or spheres) were carefully brought into contact with the water film forming a double bilayer. The water film is remarkably stable, lasting for hours to days. Moreover, each bilayer can be separated and reformed independently and repeatedly.

To verify the presence of two bilayers, we put αHL heptamers into the water reservoir (water film) and used a different non-covalent blocker (γ-cyclodextrin (γCD) or heptakis(2,3,6-tri-O-methyl)-β-cyclodextrin (TRIMEB)) in each droplet or sphere (Fig. 4.3 *A*). We observed both types of blocking events and the water film remained intact, which demonstrated that there were two bilayers (Fig. 4.3 *D*). As the two agarose spheres press into the water film from either side, the water moves radially away from the double bilayer region. Although we have not yet quantified the bilayer separation, we were able to bring the two agarose spheres so close to each other that they physically deflected without rupturing the water film and double bilayer.

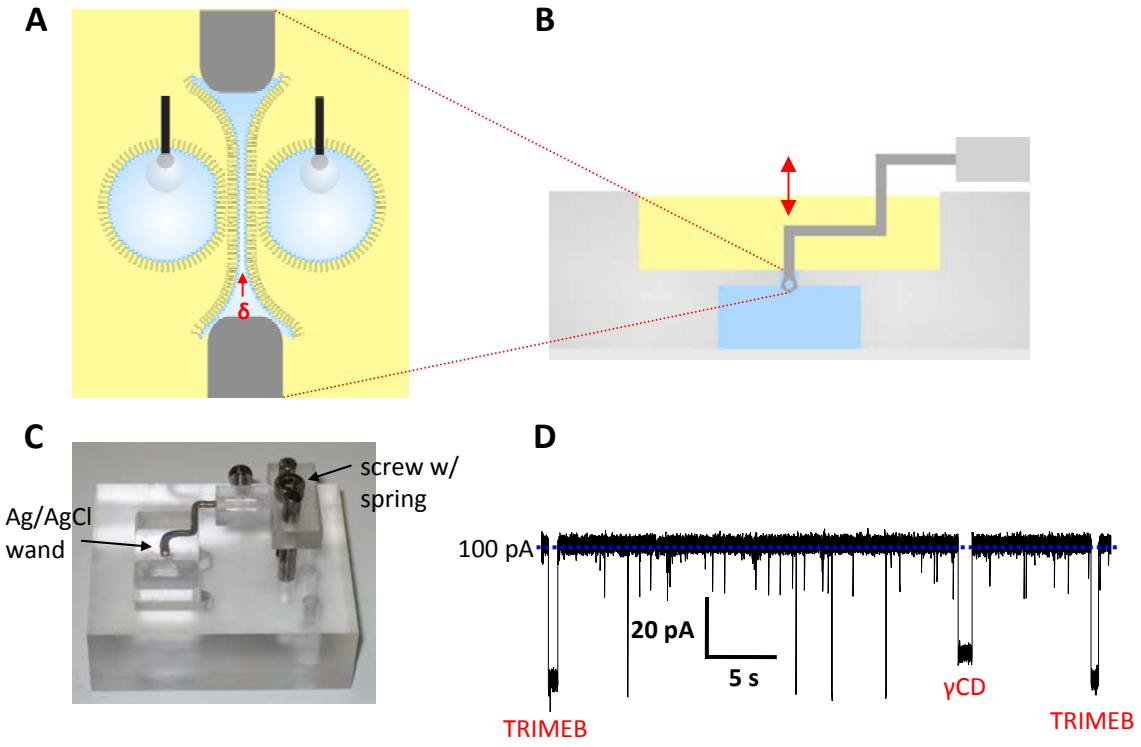

Figure 4.3 Double Bilayer to Study Dual-Membrane Spanning Proteins. (*A*) A cross-sectional enlargement of a water film stretched across the aperture of the wand, illustrating the formation of a double bilayer between two opposed aqueous droplets and an aqueous film. The two gray blocks at the top and bottom represent the surface of the Ag/AgCl wand. The droplets can be replaced with agarose spheres if some mechanical rigidity is desired. The bilayer separation is δ. (*B*) Schematic cross-section of chamber used to form double bilayers. A dipping mechanism moves the Ag/AgCl wand between the upper oil-lipid bath and the lower aqueous reservoir. The aperture of the wand becomes coated with a thin water film. (*C*) Dipping mechanism of the double bilayer platform. The wand is pressed down through the slot and into the aqueous chamber and held with a screw. To bring the water film-coated wand back into the oil-lipid bath, the screw is loosened and the spring provides the restoring force. (*D*) Double bilayer was formed with 5 μM TRIMEB and 5 μM γCD in 2.5% w/v agarose spheres, and a water film containing 2 ng/mL WTαHL. Current trace exhibits both TRIMEB (larger) and γCD (smaller) blocks and the water film remained intact. Applied potential is +50 mV.

We have begun the process of expressing and purifying human connexin 26 (Cx26).[9] We selected Cx26 because it is the smallest human connexin, associated with cochlear deafness and skin disease, and unlike larger connexins, there is no evidence for phosphorylation of the C-terminus tail (Diez et al., 1999; Harris, 2001; Zeilinger et al., 2005). Once purified Cx26 hexamer is obtained, we will attempt to reconstitute Cx26 gap

[9] This effort is being led by Dr. Stephen Cheley.

junctions in the double bilayer and perform both electrophysiological and molecular transfer studies.

How can we distinguish between two non-junctional hemichannels and a true gap junction (docked hemichannels)? The transfer of molecules less than 1 kDa in size is efficient through gap junctions but not through two undocked hemichannels. The ability to separate each bilayer in the double bilayer into monolayer components provides a powerful method for molecular transfer studies because the recipient droplet/agarose sphere can be taken out of the system and analyzed elsewhere. If we include connexins in both agarose spheres, and fluorescently-tagged, membrane impermeable molecules in only one agarose sphere (donor), we should only observe significant transfer of dye to the recipient agarose sphere if gap junctions are present (Fig. 4.4 *A*). In a system with undocked hemichannels (agarose spheres not pushed together so bilayer separation is large; Fig. 4.4 *B*) or without protein (Fig. 4.4 *C*), little to no transfer should be observed.

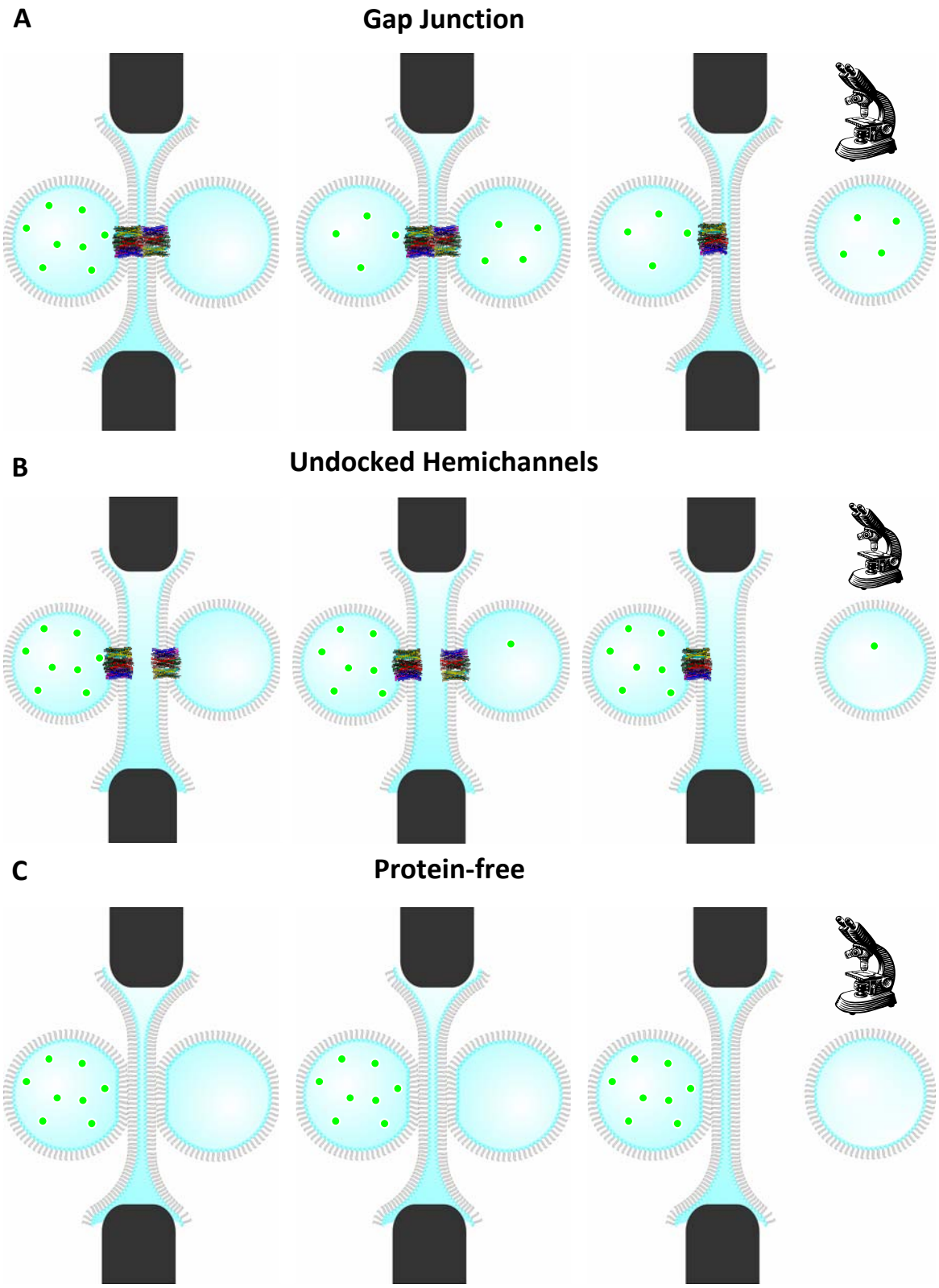

Figure 4.4 Gap Junction-Mediated Molecular Transfer. One agarose sphere contains fluorescently-tagged, membrane impermeable molecules. After a specified transfer period with the double bilayer intact, the recipient agarose sphere is removed from the system and its fluorescence is quantified. *(A)* Transfer should be efficient if hemichannels in each bilayer dock to form gap junctions. *(B)* Transfer should be inefficient if hemichannels are undocked. *(C)* Transfer should be inefficient if no connexins are present.

Chapter 5

Computing with Nanopores and Droplet Interface Bilayer Networks

5.1. Introduction

As the importance of electronics continues to increase, there is growing interest in the development of molecular systems that mimic the behavior of electronic logic gates and circuits (Balzani et al., 2003). The current evolution of technology is primarily characterized by a top-down approach as components are progressively miniaturized to make smaller devices. However, this approach is subject to intrinsic limitations for dimensions smaller than 0.1 μm (Muller et al., 1999). Information processing at the molecular scale may enable the design of "chemical computers" that are much smaller and more powerful than those currently in use. Development of molecular-scale chemical computers is appealing not only from the standpoint of continued size reduction and technological improvements, but also because interfacing a biochemical computer with biological systems may be better tolerated than traditional electronics.

The basic principle of molecular computing is to stimulate a molecule with an input and take its response as the output. Stimulation is often provided in optical,

electrical, or chemical form, and the output is also usually optical, electrical or chemical. Unlike semiconductor devices, which exhibit input-output homogeneity, the inputs and outputs of molecular computing devices are not usually of the same form, which becomes an issue when connectivity is desired (de Silva & Uchiyama, 2007). Many molecular devices that have been designed to date involve chemical inputs and a fluorescence output.

Any approach to molecular logic and computation must be able to handle numerical calculations. The basis for addition in semiconductor technology is the *half-adder*, which brings two binary input digits into a set of parallel AND and XOR gates, where the sum digit is the output of the XOR gate and the carry digit is the output of the AND gate (Fig. 5.1). The first molecular half-adder was demonstrated in 2000, driven by H^+ and Ca^{2+} inputs with an output based on fluorescence (de Silva & McClenaghan, 2000). More recently, it was demonstrated that a full-adder and full-subtractor can exist within one molecular entity by integrating OR, XOR, AND, and INH logic functions (Margulies et al., 2006).

Input		Output	
A	**B**	**SUM (XOR)**	**CARRY (AND)**
0	0	0	0
0	1	1	0
1	0	1	0
1	1	0	1

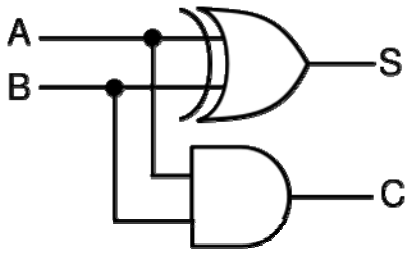

Figure 5.1 Half-Adder Truth Table and Schematic.

5.2. Results and Discussion

5.2.1. Nanopore Logic

Nanopores such as αHL are highly amenable to engineering (Bayley & Jayasinghe, 2004) for stochastic sensing applications. To show that it is possible to harness nanopore

stochastic sensing for molecular logic applications, imagine a MM planar bilayer system with perfusion capabilities (Fig. 5.2). A single wild-type αHL pore is inserted into the bilayer and the two chemical inputs are γ-cyclodextrin (γCD) and heptakis(2,3,6-tri-O-methyl)-β-cyclodextrin (TRIMEB). The chamber is rinsed with buffer (10 mM HEPES, 1 M KCl, pH 7.0) between successive inputs to the system.

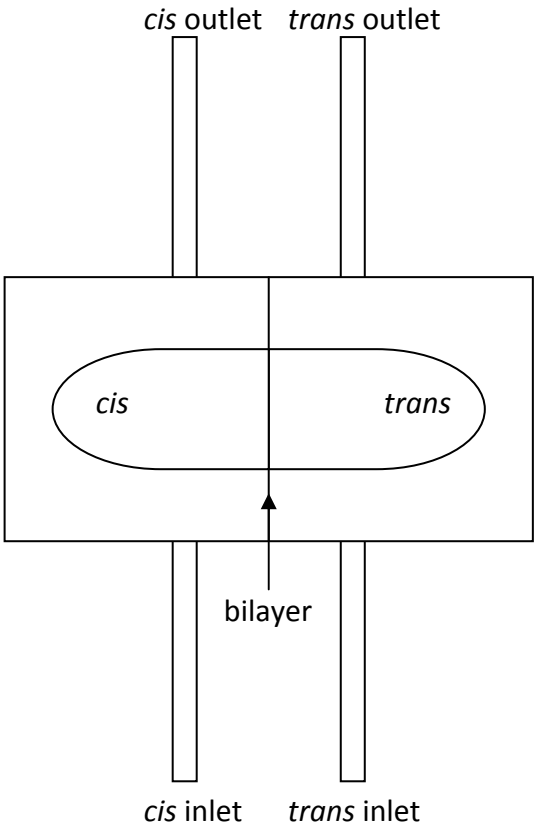

Figure 5.2 Perfusable Planar Bilayer Chamber. Protein is inserted from the *cis* side of the chamber and non-covalent pore blockers γCD and TRIMEB are introduced to the *trans* side.

The four possible input combinations are buffer (0,0), γCD only (0,1), TRIMEB only (1,0), and both γCD and TRIMEB (1,1). The all-points histograms that result from each of these input combinations are unique, and therefore differential interpretation of the output enables every logic gate to be realized, including universal gates NAND and NOR (Fig. 5.3). By performing logic functions in this way sequentially or in parallel, any logic circuit can be realized, including binary addition. Like other methods of molecular

logic, the major drawback of this method is that it is not self-sufficient. The requirement for external systems to control inputs, interpret and store outputs, and integrate results still exists.

A

Input		Output							
TRIMEB	γCD	Raw	AND	OR	XOR	NAND	NOR	INH	XNOR
0	0	P1	0	0	0	1	1	0	1
0	1	P1,P2	0	1	1	1	0	1	0
1	0	P1, P3	0	1	1	1	0	0	0
1	1	P1, P2, P3	1	1	0	0	0	0	1

B

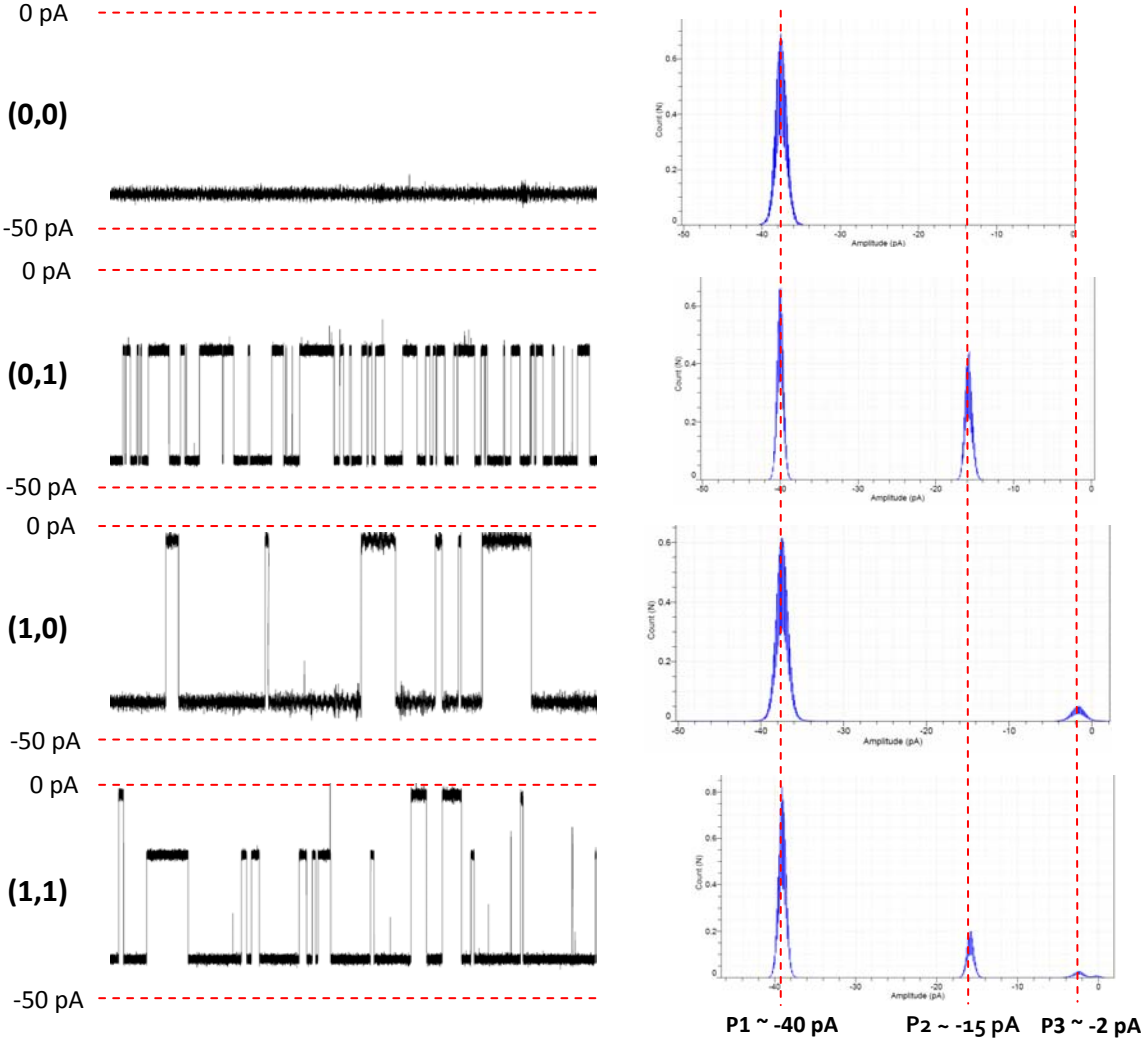

Figure 5.3 Nanopore Molecular Logic. (*A*) Raw and interpreted output corresponding to each input combination of TRIMEB and γCD for several logic gates. (*B*) *Left*: Electrical recordings of the interactions between each input combination and the WT αHL pore. *Right*: All-points histograms of corresponding electrical recordings. The histogram signature for each input combination is unique, which can be interpreted as desired to realize any logic gate.

5.2.2. Nanopore Keypad Lock

While binary logic enables a broad range of computational applications, the unique features of our nanopore-based system allow us to create other electronic devices based on more complex logic. For example, an important electronic device is the keypad lock, which protects an object or data. The user is required to enter an appropriate password before access is granted. What makes an electronic keypad circuit more complex than a simple logic gate is the fact that its output is dependent on the *ordered* combination of inputs. In other words, A-B-C is not equivalent to C-B-A. Recently, keypad locks at the molecular scale have been demonstrated using fluorescent biosensors (Margulies et al., 2007) and enzyme cascades (Strack et al., 2008). In the following, we demonstrate the first nanopore molecular keypad lock.

We exploit the recent development of an engineered α-hemolysin pore, $(M113F)_6(M113C\text{-}D8RL2)_1$, which covalently attaches a βCD adapter (Wu et al., 2007). Suppose we install a password protection scheme that consists of the letters "A," "B," and "C" (Fig. 5.4). Three solutions are employed, all in 25 mM TRIS, 1 M KCl, pH 8.0. Solution A contains 16 μM β-cyclodextrin pyridyldithiopropionate (βCD-PDP), solution B contains 200 μM β-estradiol-3-sulfate, and solution C contains $(M113F)_6(M113C\text{-}D8RL2)_1$ αHL, prepared as previously described (Cheley et al., 1999). A voltage of +80 mV is applied to the system.

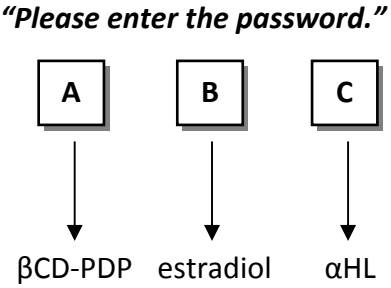

Figure 5.4 Nanopore Keypad Lock. The user is prompted to enter the password. Each key is wired to a unique solution that is injected into the perfusable bilayer chamber (Fig. 5.2) and then washed out with buffer prior to registration of the next keystroke.

The user is prompted to enter a three-letter password. When a key is pressed, the corresponding solution flows into the perfusable chamber (Figs. 5.2, 5.4). Between each key press, the previous solution is washed out with buffer. The password protection circuit only unlocks when it detects a peak near 0 pA in the all-points current histogram (Fig. 5.5). This only occurs for the input combination C-A-B, which yields two peaks—one near 20 pA corresponding to the open pore current level with the adapter, and the other near 0 pA corresponding to estradiol blockade. This combination is unique because the pore must be in the bilayer before the βCD-PDP is able to covalently bind to the pore, and the βCD adapter must attach to the pore before the estradiol so that the latter can interact with the pore. Estradiol does not interact significantly with the pore without the covalent adapter (Fig. 5.5).

The other input combinations produce varying outputs. When C and B both precede A (i.e., C-B-A or B-C-A), the βCD adapter attaches to the pore but the estradiol is washed away, leading to a single peak around 20 pA. On the other hand, when A precedes C (i.e., A-B-C, A-C-B, or B-A-C), the pore remains open and a single peak between 70 and 80 pA is observed.

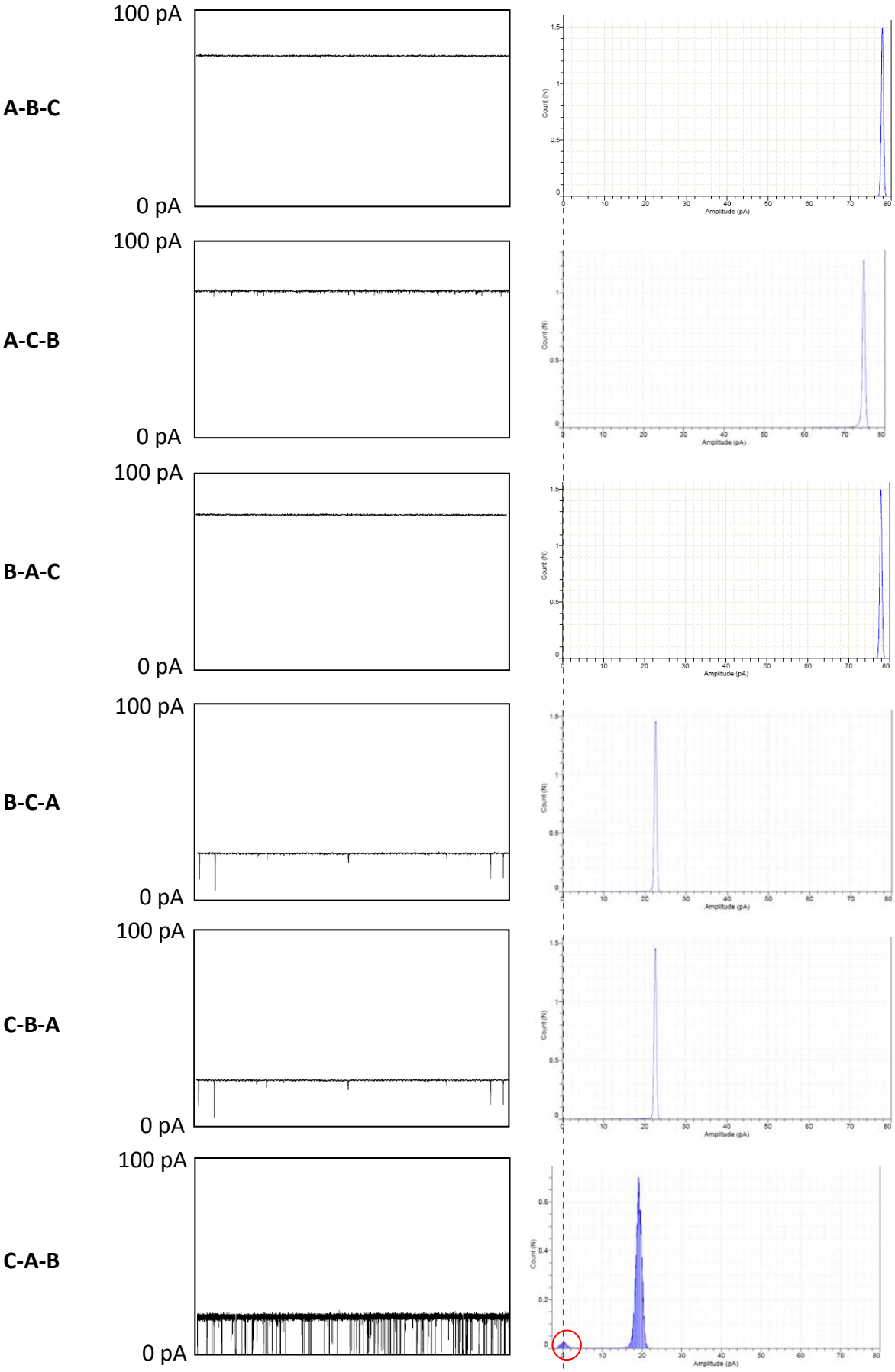

Figure 5.5 Nanopore Keypad Lock Inputs and Outputs. (*Left column*) Electrical recordings at +80 mV for each input combination. (*Right column*) All-points histograms of corresponding electrical recordings. A current peak near 0 pA is only present for input sequence C-A-B, which unlocks the system.

5.2.3. Nanopore Valve

An engineered αHL with seven arginine residues per monomer (7R-αHL; positions 113, 115, 117, 119, 121, 123, 125) was synthesized by *in vitro* transcription and translation (IVTT) and the homoheptamer was purified as described elsewhere (Cheley et al., 1997).[10] The 7R-αHL pore spontaneously reconstitutes in both planar bilayers and DIBs, and exhibits behavior similar to a valve or diode (Fig. 5.6).

The buffering conditions were 25 mM Tris, 1 M KCl, pH 8.0. Pores insert from the electrically grounded side of the bilayer. At positive potentials, the pore has a unitary conductance (900-950 pS at +50 mV; Fig. 5.6) comparable to the wild-type pore. However, at negative potentials, the pore closes and allows minimal current flow (0-100 pS at -50 mV; Fig. 5.6). Although the mechanism for this behavior is not presently understood, it is hypothesized that the β-barrel of the pore collapses at negative potentials. The reopening of the pore upon switching to a positive potential is immediate and complete. In this way, the 7R-αHL allows significant current flow in one direction only and could potentially find utility as a diode in DIB networks.

The rectification properties of the 7R-αHL were tested by applying a sinusoidal voltage waveform. The protein was produced by incubating the PURE system IVTT mixture (Syeda et al., 2008) with the 7R-αHL plasmid at 37°C for an hour. A DIB was formed from the unpurified IVTT mixture and many pores inserted into the bilayer. The 7R-αHL rectifies very well at frequencies below 100 mHz and its performance gradually degrades at higher frequencies (Fig. 5.7). At frequencies over 1 Hz, the mutant pore exhibits behavior increasingly similar to that of the wild-type pore. Because the IVTT

[10] Prepared by Ellina Mikhailova.

reaction produces monomers, the noisier trace (Fig. 5.7) is likely due to the presence of some improperly oligomerized pores in the bilayer.

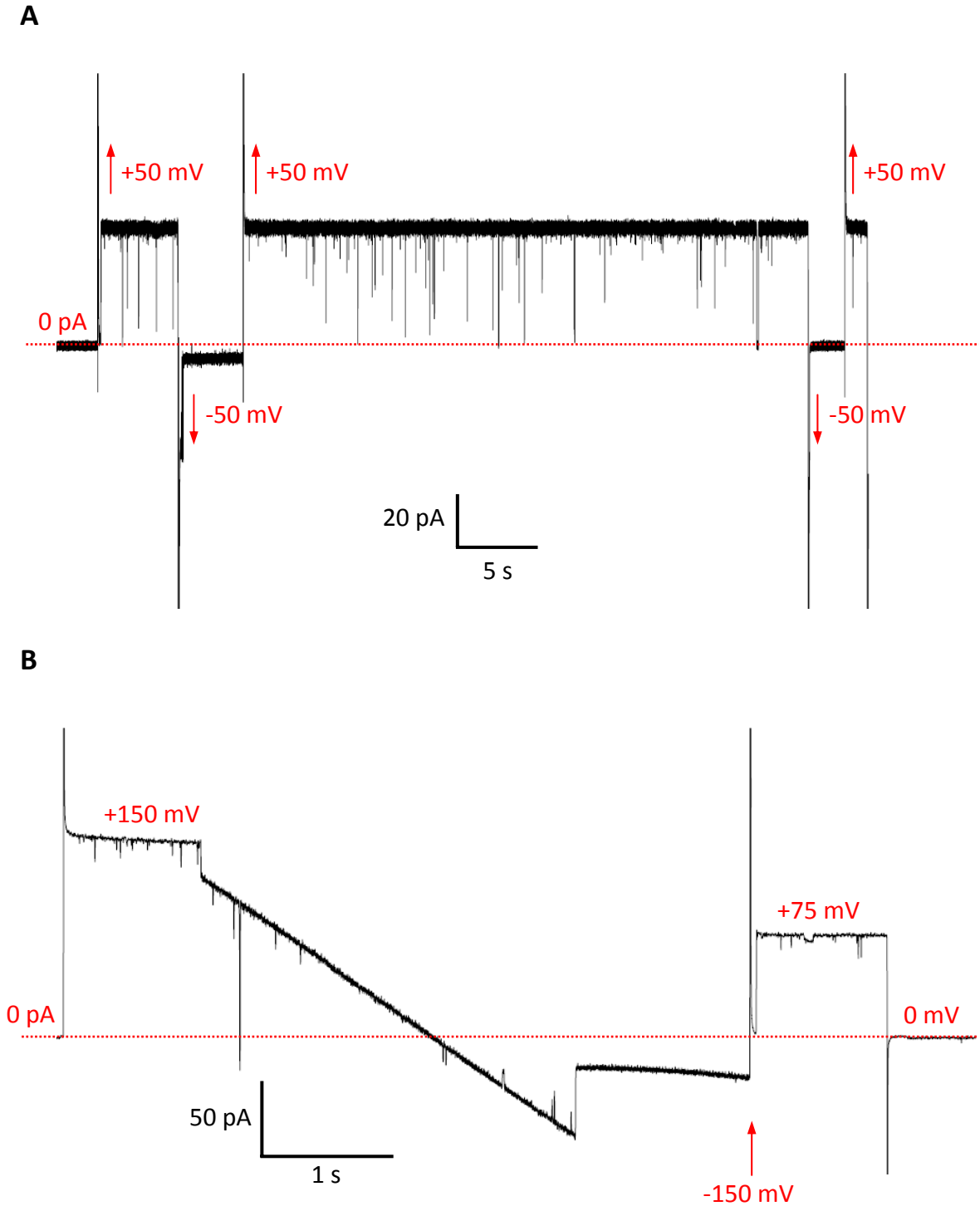

Figure 5.6 Electrical Behavior of the Nanopore Valve. A single 7R-αHL pore reconstituted in a DIB. Buffering conditions were 25 mM Tris, 1 M KCl, pH 8.0. *(A)* Alternating applications of +50 mV and -50 mV show that the pore opened at positive potentials and closed soon after a negative potential was applied. Switching from a negative to a positive potential induced immediate pore reopening. *(B)* A more complex voltage function was applied: +150 mV for one second, three second linear ramp to -150 mV, +75 mV for one second, and lastly, cessation of applied voltage (0 mV). When the linear ramp moves to negative

potentials, the pore closed at approximately -65 mV and exhibited a small leak current as the negative potential continued to increase in magnitude.

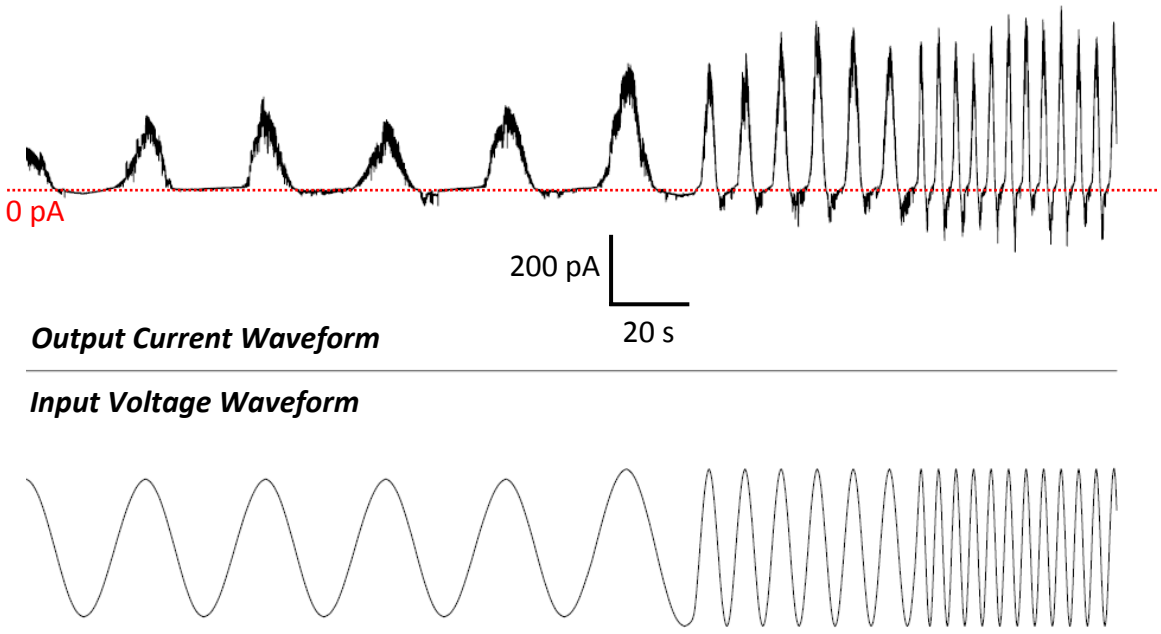

Figure 5.7 Nanopore Half-Wave Rectifier. Numerous 7R-αHL pores from an unpurified PURE system IVTT reaction inserted into a DIB. A sinusoidal input voltage waveform was applied and rectification in the output current waveform was dramatic especially at low frequencies (< 100 mV). As the frequency increased, the transient appearance of current at the beginning of the negative half-wave became more pronounced.

5.2.4. Droplet Interface Bilayer Computing Networks

The assembly of droplet interface bilayers into biochemical computing networks is an exciting prospect and has several potential advantages over extant methods. First, DIB networks are compartmental, which makes addressing simple unlike other molecular computing techniques that involve inputs, outputs, and intermediates mixed in the same solution. Second, DIB networks are modular, which means that different parts of the network can be performing distinct processes that can be integrated as desired. Third, the scalability of DIB networks enables development of complex computational devices. Finally, DIB networks are highly reconfigurable so that their functions can be changed easily. Furthermore, different sets of inputs can be applied

sequentially without cross-contamination and the need for cleaning and rebuilding after each use.

The discovery of an engineered membrane pore with diode-like properties represents an important addition to the DIB network toolkit (Chapter 2). In a three-droplet network, the orientation of the 7R-αHL in each bilayer can significantly change the overall network behavior (Fig. 5.8). When the 7R-αHL pores in each bilayer are oriented in opposite directions, the network behaves as a current limiter, with little current passing in either direction (Fig. 5.8 *D*). On the other hand, when the 7R-αHL pores in each bilayer are oriented in the same direction, current passes when the network is forward-biased and not when it is reverse-biased (Fig. 5.8 *C*). We are currently developing DIB networks with the 7R-αHL pore that perform a range of other functions such as diode-resistor logic gates (Fig. 5.9) and an AC-DC converter/full-wave rectifier (Fig. 5.10).

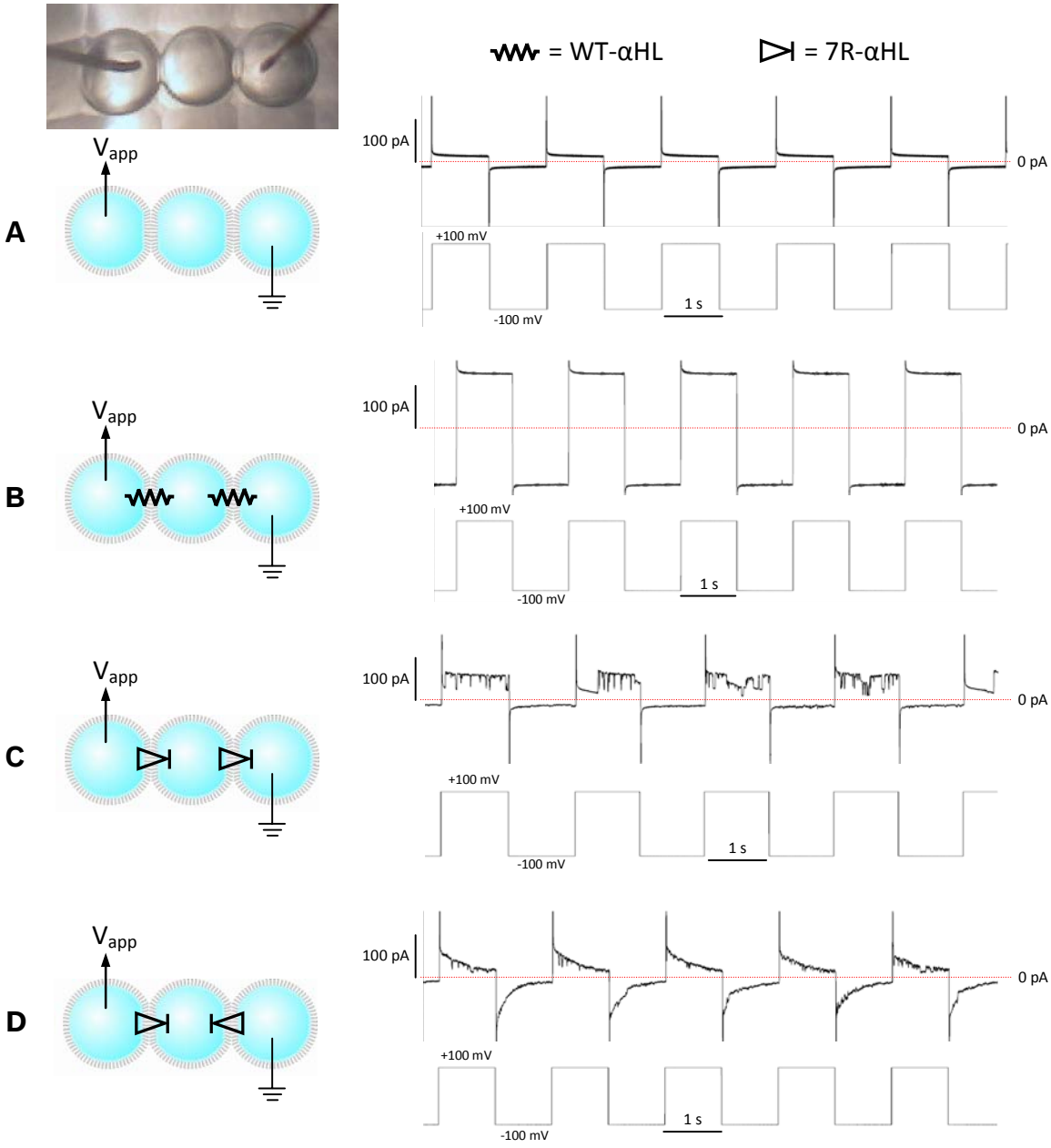

Figure 5.8 Three-droplet DIB Networks. DIBs were formed with 2 mM DPhPC vesicles inside droplets and 5 mM DPhPC in hexadecane outside droplets. In each part of the figure, output current trace (top) is shown in phase with input voltage square wave (bottom). *(A)* No proteins are included in the system. *(B)* WT-αHL inserts into both bilayers from the middle droplet. *(C)* 7R-αHL inserts into both bilayers with the same orientation. *(D)* 7R-αHL inserts into both bilayers with opposing orientations.

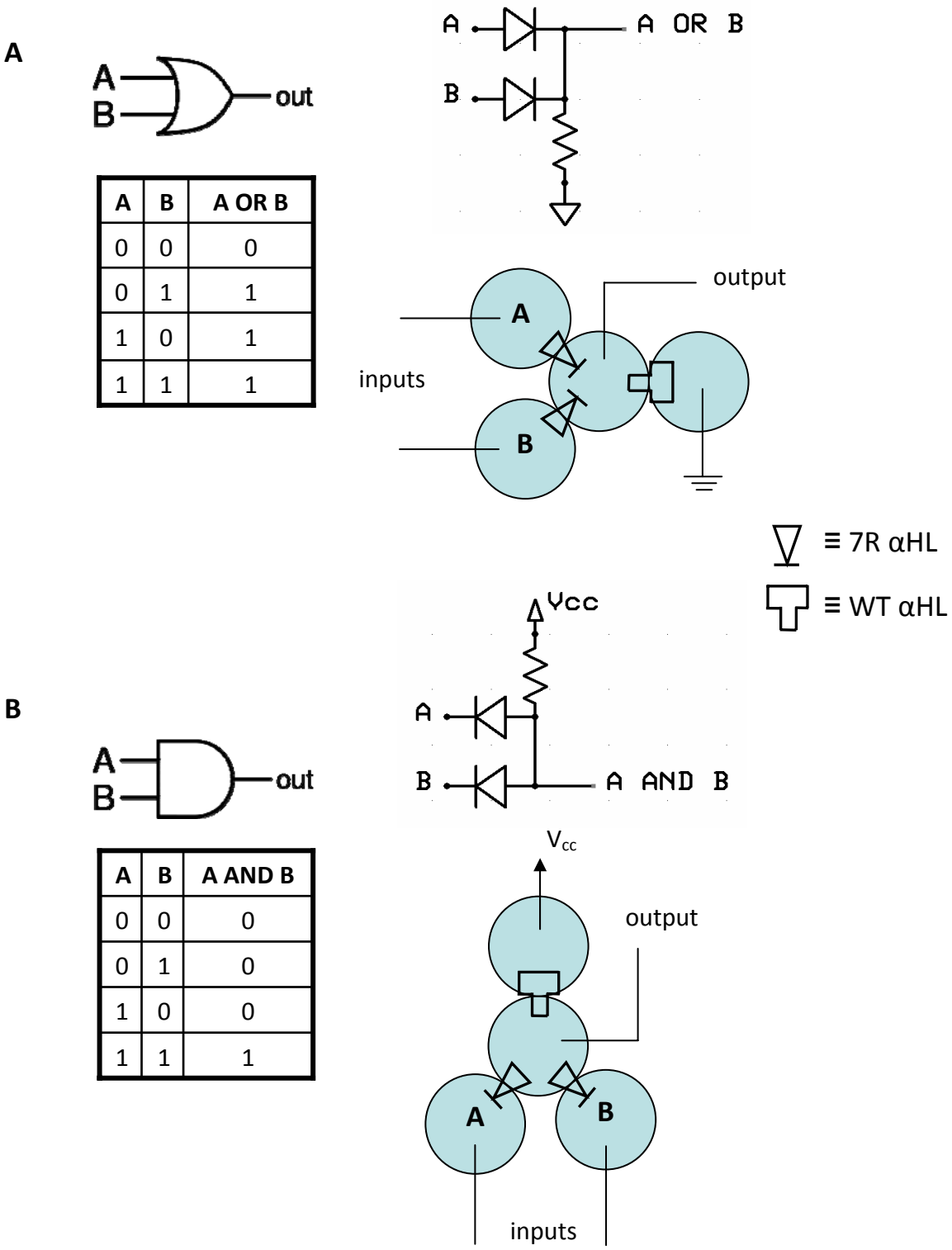

A	B	A OR B
0	0	0
0	1	1
1	0	1
1	1	1

A	B	A AND B
0	0	0
0	1	0
1	0	0
1	1	1

Figure 5.9 DIB Logic Gates. Logic symbol, truth table, diode-resistor circuit, and translation of circuit to DIB network for *(A)* two-input OR logic gate, and *(B)* two-input AND logic gate.

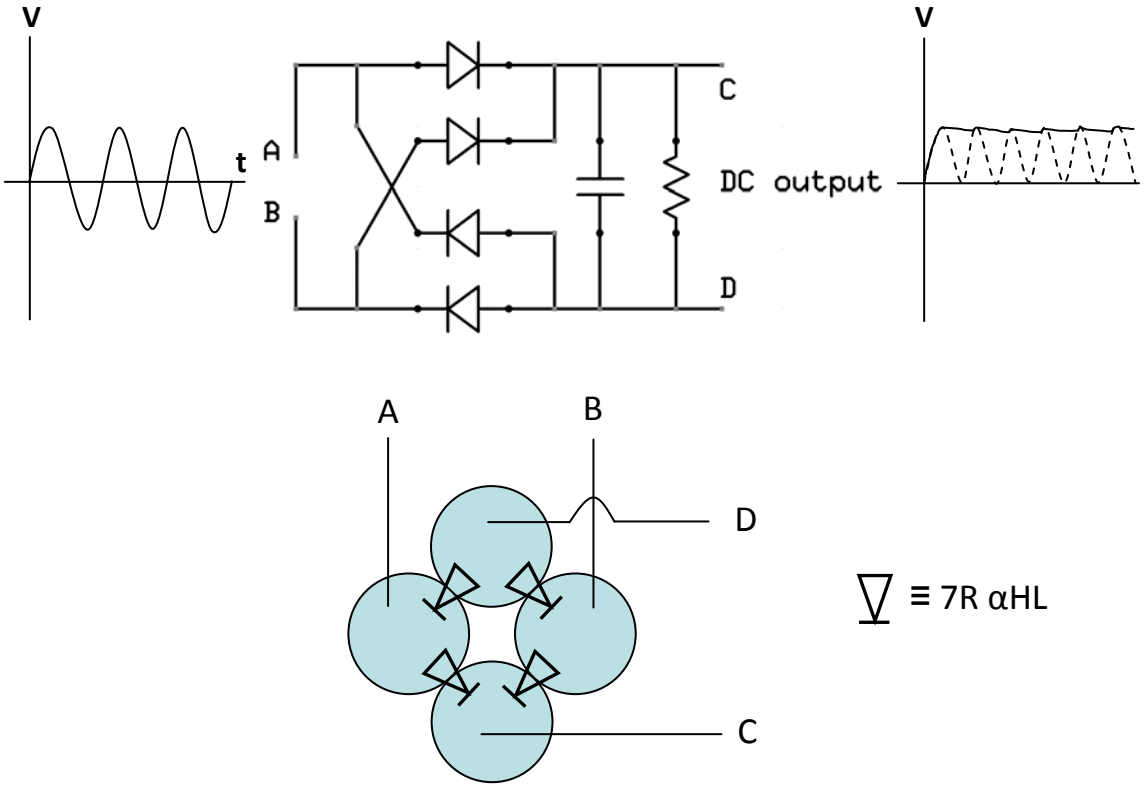

Figure 5.10 DIB AC-DC Converter. *(Top)* Full-wave bridge rectifier circuit with a smoothing capacitor. A sinusoidal input is converted to a DC output (dotted line illustrates the output when no smoothing capacitor is present). *(Bottom)* Translation of the rectifier circuit to a four-droplet DIB network. Each droplet corresponds to one of the four nodes in the circuit (A-D).

Chapter 6

Conclusion and Future Directions

The development and application of droplet interface bilayer technology is a nascent but promising area of research. In this thesis, we have extended the initial conception of DIBs as the formation of a bilayer between two lipid monolayer-encased aqueous droplets in an oil-lipid solution in several ways. First, we showed that moving the lipids inside the aqueous droplets in the form of vesicles created more stable DIBs with reduced experimental cost. These lipid-in DIBs also enable the formation of asymmetric bilayers, which we used to study the effects of charged asymmetric bilayers on the behavior of several protein pores and ion channels. Second, the use of a water film and agarose spheres instead of droplets enabled us to form two closely juxtaposed bilayers, which may enable the first single-channel studies of dual-membrane spanning proteins in an artificial bilayer platform. In additional to these scientific and technological advances, we have also provided a quantitative foundation for DIB networks by demonstrating that simple electrical modeling can explain and predict network behavior. Electrical circuit simulations will likely play a major role in the

continued development of increasingly complex DIB networks. Finally, we exploited nanopores and DIB networks for biochemical logic and computing applications.

Although the manual formation of DIBs is reliable, automation of the process through microfluidics would greatly increase throughput and experimental possibilities. The first generation of microfluidic biochips was based on the manipulation of continuous liquid flow through fabricated microchannels. Recently, a novel microfluidics technology has been developed to manipulate liquids as discrete droplets, referred to as *digital* microfluidics in an analogy to digital electronics (Pollack et al., 2002). Digital microfluidic biochips (DMBs) typically consist of two glass plates separated by a small gap that is filled with oil; droplets are dispensed and their position electrically controlled within the glass plate sandwich (Fig. 6.1). The bottom plate includes an array of control electrodes whereas the top plate is a continuous ground electrode (Fig. 6.1). Droplet movement is enabled by electrowetting, which refers to the modulation of the interfacial tension between a conductive fluid and a solid electrode coated with a dielectric layer by applying an electric field between them (Pollack et al., 2000). An imbalance of interfacial tension is created if an electric field is applied to only one side of the droplet; this tension gradient induces the droplet to move (Fig. 6.1) (Su et al., 2007). We could potentially move aqueous droplets containing lipid vesicles together in a DMB filled with an oil medium to form bilayers. Droplet dispensing, mixing, splitting, and optical detection of reactions/analytes in droplets have all been demonstrated on DMBs (Hwang et al., 2006; Xu et al., 2007), and could be seamlessly transferred to DIB technology.

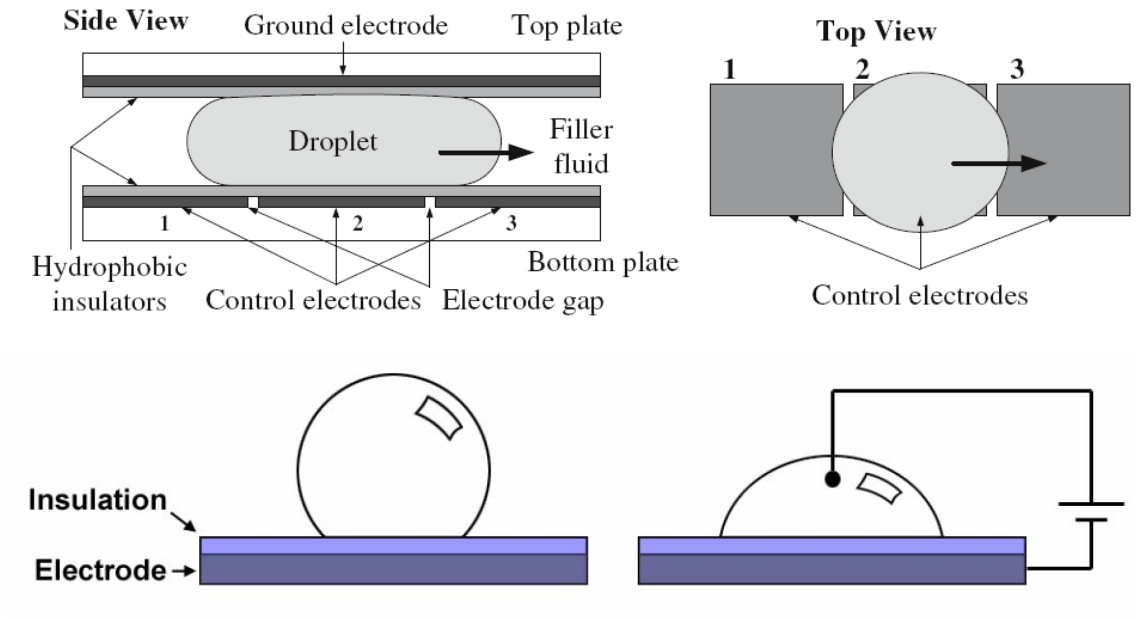

Figure 6.1 Operation of a Digital Microfluidic Biochip based on Electrowetting. *(A)* Schematic diagram of digital microfluidic biochip. A potential is applied to electrode 2 to hold droplet in place. To move droplet to position 3, electrode 3 is switched on and electrode 2 is turned off. Adapted from (Su et al., 2007). *(B) Left*: No potential applied. A droplet on a hydrophobic surface has a large contact angle; *Right*: Applied potential. The droplet's surface energy increases, which results in a reduced contact angle. The droplet now wets the surface. Adapted from (Hwang, 2006).

One current drawback of DIBs relative to planar bilayers is the inability to perfuse and control the contents of each droplet after the DIB is formed. It is possible to burst a fresh droplet into a droplet that is already part of a DIB network, but it is technically challenging. Although there are potential ways to circumvent this issue, such as caged/protected components in droplets that are light or temperature activated, a reliable method of perfusing droplets would be a considerable advance.

The use of artificial bilayer systems to study membrane proteins at the single-channel and ensemble levels is of great interest to both the scientific and biomedical communities. For both planar and droplet interface bilayers, membrane protein studies often depend on spontaneous protein assembly and insertion. However, many channels do not spontaneously reconstitute in bilayers. For example, while Kcv readily inserts into

DIBs (Hwang et al., 2008), Kcsa, a potassium channel from *Streptomyces lividans*, does not. Although it was recently shown that membrane proteins can be reconstituted in planar bilayers by direct transfer from a glass probe (Holden & Bayley, 2005; Holden et al., 2006), no equivalent method has been demonstrated for DIBs, although the tip of an electrode attached to a droplet can be brought into contact with the DIB without rupture. More effective techniques to promote the reconstitution of membrane proteins in bilayers would represent a significant breakthrough for electrophysiology research.

Manipulating the position of the droplets that form a DIB modulates the bilayer size, curvature, and stress. This feature of DIBs may enable detailed studies of mechanosensitive channels that are not possible with other bilayer systems.

It may be possible to design miniature biochemical machines from DIB networks. Macromolecules like proteins (Astier et al., 2005) and DNA (Yurke et al., 2000) have been used as components for nanomachines. DIB networks, on the other hand, can be viewed as groups of communicating protocells (Chapter 2), and might be developed into micromachines that mimic simple tissues or organisms. Future research in this area will likely begin by demonstrating an assortment of critical functions such as sensing, signal transmission, energy utilization, uptake, and movement.

References

ALBER, F., DOKUDOVSKAYA, S., VEENHOFF, L. M., ZHANG, W. H., KIPPER, J., DEVOS, D., SUPRAPTO, A., KARNI-SCHMIDT, O., WILLIAMS, R., CHAIT, B. T., SALI, A. & ROUT, M. P. (2007a). The molecular architecture of the nuclear pore complex. Nature, 450(7170), 695-701.

ALBER, F., DOKUDOVSKAYA, S., VEENHOFF, L. M., ZHANG, W. Z., KIPPER, J., DEVOS, D., SUPRAPTO, A., KARNI-SCHMIDT, O., WILLIAMS, R., CHAIT, B. T., ROUT, M. P. & SALI, A. (2007b). Determining the architectures of macromolecular assemblies. Nature, 450(7170), 683-694.

ALBERTS, B., JOHNSON, A., LEWIS, J., RAFF, M., ROBERTS, K. & WALTER, P. (2002). Molecular biology of the cell, 4th edition. New York: Garland Science.

ALEX, J., CALE, A. R. J., COWEN, M. E., GRIFFIN, S. C. & GUVENDIK, L. (2005). Connexins: the basis of functional coupling of myocytes. Journal of Clinical and Basic Cardiology, 8, 19-22.

ANGLIN, T. C., LIU, J. & CONBOY, J. C. (2007). Facile lipid flip-flop in a phospholipid bilayer induced by gramicidin A measured by sum-frequency vibrational spectroscopy. Biophysical Journal, 92(1), L1-L3.

ASHCROFT, F. M. (2000). Ion channels and disease: channelopathies. San Diego: Academic Press.

ASHLEY, R. H., ed. (1995). Ion channels: a practical approach. Oxford: Oxford University Press.

ASTIER, Y., BAYLEY, H. & HOWORKA, S. (2005). Protein components for nanodevices. Current Opinion in Chemical Biology, 9(6), 576-584.

BALASUBRAMANIAN, K. & SCHROIT, A. J. (2003). Aminophospholipid asymmetry: A matter of life and death. Annual Review of Physiology, 65, 701-734.

BALZANI, V., CREDI, A. & VENTURI, M. (2003). Molecular logic circuits. Chemphyschem, 4(1), 49-59.

BASU, S., MEHREJA, R., THIBERGE, S., CHEN, M. T. & WEISS, R. (2004). Spatiotemporal control of gene expression with pulse-generating networks. Proceedings of the National Academy of Sciences of the United States of America, 101(17), 6355-6360.

BAYLEY, H. & CREMER, P. S. (2001). Stochastic sensors inspired by biology. Nature, 413(6852), 226-230.

BAYLEY, H., CRONIN, B., HERON, A. J., HOLDEN, M. A., HWANG, W. L., SYEDA, R., THOMPSON, J. R. & WALLACE, M. I. (2008). Droplet interface bilayers. In prep.

BAYLEY, H. & JAYASINGHE, L. (2004). Functional engineered channels and pores - (Review). Molecular Membrane Biology, 21(4), 209-220.

BENNETT, I. M., FARFANO, H. M. V., BOGANI, F., PRIMAK, A., LIDDELL, P. A., OTERO, L., SERENO, L., SILBER, J. J., MOORE, A. L., MOORE, T. A. & GUST, D. (2002). Active transport of Ca2+ by an artificial photosynthetic membrane. Nature, 420(6914), 398-401.

BHAKDI, S., FUSSLE, R. & TRANUMJENSEN, J. (1981). Staphylococcal alpha-toxin - oligomerization of hydrophilic monomers to form amphiphilic hexamers induced through contact with deoxycholate detergent micelles. Proceedings of the National Academy of Sciences of the United States of America-Biological Sciences, 78(9), 5475-5479.

BHOSALE, S., SISSON, A. L., TALUKDAR, P., FURSTENBERG, A., BANERJI, N., VAUTHEY, E., BOLLOT, G., MAREDA, J., ROGER, C., WURTHNER, F., SAKAI, N. & MATILE, S. (2006). Photoproduction of proton gradients with pi-stacked fluorophore scaffolds in lipid bilayers. Science, 313(5783), 84-86.

BOENGLER, K., SCHULZ, R. & HEUSCH, G. (2006). Connexin 43 signalling and cardioprotection. Heart, 92(12), 1724-1727.

BOON, J. M. & SMITH, B. D. (2002). Chemical control of phospholipid distribution across bilayer membranes. Medicinal Research Reviews, 22(3), 251-281.

BREWER, G. J. (1991). Reconstitution of lens channels beween two membranes. In Biophysics of gap junction channels (ed. C. Peracchia). Boca Raton: CRC Press.

CHELEY, S., BRAHA, G., LU, X. F., CONLAN, S. & BAYLEY, H. (1999). A functional protein pore with a "retro" transmembrane domain. Protein Science, 8(6), 1257-1267.

CHELEY, S., MALGHANI, M. S., SONG, L. Z., HOBAUGH, M., GOUAUX, J. E., YANG, J. & BAYLEY, H. (1997). Spontaneous oligomerization of a staphylococcal alpha-hemolysin conformationally constrained by removal of residues that form the transmembrane beta-barrel. Protein Engineering, 10(12), 1433-1443.

CHEN, I. A., SALEHI-ASHTIANI, K. & SZOSTAK, J. W. (2005). RNA catalysis in model protocell vesicles. Journal of the American Chemical Society, 127(38), 13213-13219.

CHEN, M., KHALID, S., SANSOM, M. S. P. & BAYLEY, H. (2008). Outer membrane protein G: Engineering a quiet pore for biosensing. Proceedings of the National Academy of Sciences of the United States of America, 105, 6272-6277.

CONLAN, S. & BAYLEY, H. (2003). Folding of a monomeric porin, OmpG, in detergent solution. Biochemistry, 42(31), 9453-9465.

CONLAN, S., ZHANG, Y., CHELEY, S. & BAYLEY, H. (2000). Biochemical and biophysical characterization of OmpG: A monomeric porin. Biochemistry, 39(39), 11845-11854.

CRANE, J. M., KIESSLING, V. & TAMM, L. K. (2005). Measuring lipid asymmetry in planar supported bilayers by fluorescence interference contrast microscopy. Langmuir, 21(4), 1377-1388.

DAKIN, K., ZHAO, Y. R. & LI, W. H. (2005). LAMP, a new imaging assay of gap junctional communication unveils that Ca2+ influx inhibits cell coupling. Nature Methods, 2(1), 55-62.

DALEKE, D. L. (2007). Phospholipid flippases. Journal of Biological Chemistry, 282(2), 821-825.

DE SILVA, A. P. & MCCLENAGHAN, N. D. (2000). Proof-of-principle of molecular-scale arithmetic. Journal of the American Chemical Society, 122(16), 3965-3966.

DE SILVA, A. P. & UCHIYAMA, S. (2007). Molecular logic and computing. Nature Nanotechnology, 2(7), 399-410.

DEVAUX, P. F., FELLMANN, P. & HERVE, P. (2002). Investigation on lipid asymmetry using lipid probes - Comparison between spin-labeled lipids and fluorescent lipids. Chemistry and Physics of Lipids, 116(1-2), 115-134.

DEVAUX, P. F. & MORRIS, R. (2004). Transmembrane asymmetry and lateral domains in biological membranes. Traffic, 5(4), 241-246.

DIAZ, C., MORKOWSKI, J. & SCHROIT, A. J. (1996). Generation of phenotypically aged phosphatidylserine-expressing erythrocytes by dilauroylphosphatidylcholine-induced vesiculation. Blood, 87(7), 2956-2961.

DIEZ, J. A., AHMAD, S. & EVANS, W. H. (1999). Assembly of heteromeric connexons in guinea-pig liver en route to the Golgi apparatus, plasma membrane and gap junctions. European Journal of Biochemistry, 262(1), 142-148.

EVANS, W. H. & MARTIN, P. E. M. (2002). Gap junctions: structure and function (Review). Molecular Membrane Biology, 19(2), 121-136.

FADOK, V. A., SAVILL, J. S., HASLETT, C., BRATTON, D. L., DOHERTY, D. E., CAMPBELL, P. A. & HENSON, P. M. (1992). Different populations of macrophages use either the vitronectin receptor or the phosphatidylserine receptor to recognize and remove apoptotic cells. Journal of Immunology, 149(12), 4029-4035.

FETTIPLA, R., ANDREWS, D. M. & HAYDON, D. A. (1971). Thickness, composition and structure of some lipid bilayers and natural membranes. Journal of Membrane Biology, 5(3), 277-&.

FISCHER, A., FRANCO, A. & OBERHOLZER, T. (2002). Giant vesicles as microreactors for enzymatic mRNA synthesis. Chembiochem, 3(5), 409-417.

FISHER, L. R., PARKER, N. S. & HAYDON, D. A. (1986). Interferometric studies of lipid bilayer interactions. Faraday Discussions, 249-256.

FUNAKOSHI, K., SUZUKI, H. & TAKEUCHI, S. (2006). Lipid bilayer formation by contacting monolayers in a microfluidic device for membrane protein analysis. Analytical Chemistry, 78(24), 8169-8174.

GAZZARRINI, S., SEVERINO, M., LOMBARDI, M., MORANDI, M., DIFRANCESCO, D., VAN ETTEN, J. L., THIEL, G. & MORONI, A. (2003). The viral potassium channel Kcv: structural and functional features. Febs Letters, 552(1), 12-16.

GONZALEZ, J. E., OADES, K., LEYCHKIS, Y., HAROOTUNIAN, A. & NEGULESCU, P. A. (1999). Cell-based assays and instrumentation for screening ion-channel targets. Drug Discovery Today, 4(9), 431-439.

GOUAUX, E. (1998). Alpha-hemolysin from Staphylococcus aureus: an archetype of beta-barrel, channel-forming toxins. Journal of Structural Biology, 121(2), 110-122.

GU, L. Q., BRAHA, O., CONLAN, S., CHELEY, S. & BAYLEY, H. (1999). Stochastic sensing of organic analytes by a pore-forming protein containing a molecular adapter. Nature, 398(6729), 686-690.

GU, L. Q., CHELEY, S. & BAYLEY, H. (2001a). Capture of a single molecule in a nanocavity. Science, 291(5504), 636-640.

GU, L. Q., CHELEY, S. & BAYLEY, H. (2001b). Prolonged residence time of a noncovalent molecular adapter, beta-cyclodextrin, within the lumen of mutant alpha-hemolysin pores. Journal of General Physiology, 118(5), 481-493.

GU, L. Q., DALLA SERRA, M., VINCENT, J. B., VIGH, G., CHELEY, S., BRAHA, O. & BAYLEY, H. (2000). Reversal of charge selectivity in transmembrane protein pores by using noncovalent molecular adapters. Proceedings of the National Academy of Sciences of the United States of America, 97(8), 3959-3964.

HAGGE, S. O., DE COCK, H., GUTSMANN, T., BECKERS, F., SEYDEL, U. & WIESE, A. (2002). Pore formation and function of phosphoporin PhoE of Escherichia coli are determined by the core sugar moiety of lipopolysaccharide. Journal of Biological Chemistry, 277(37), 34247-34253.

HARRIS, A. L. (2001). Emerging issues of connexin channels: biophysics fills the gap. Quarterly Reviews of Biophysics, 34(3), 325-472.

HERNANDEZ, V. H., BORTOLOZZI, M., PERTEGATO, V., BELTRAMELLO, M., GIARIN, M., ZACCOLO, M., PANTANO, S. & MAMMANO, F. (2007). Unitary permeability of gap junction channels to second messengers measured by FRET microscopy. Nature Methods, 4(4), 353-358.

HERON, A. J., THOMPSON, J. R., MASON, A. E. & WALLACE, M. I. (2007). Direct detection of membrane channels from gels using water-in-oil droplet bilayers. Journal of the American Chemical Society, 129(51), 16042-16047.

HERTEL, B., TAYETEH, S., MEHMEL, M., KAST, S. M., VAN ETTEN, J. L., MORONI, A. & THIEL, G. (2006). Elongation of outer transmembrane domain alters function of miniature K+ channel Kcv. Journal of Membrane Biology, 210(1), 21-29.

HOLDEN, M. A. & BAYLEY, H. (2005). Direct introduction of single protein channels and pores into lipid bilayers. Journal of the American Chemical Society, 127(18), 6502-6503.

HOLDEN, M. A., JAYASINGHE, L., DALTROP, O., MASON, A. & BAYLEY, H. (2006). Direct transfer of membrane proteins from bacteria to planar bilayers for rapid screening by single-channel recording. Nature Chemical Biology, 2(6), 314-318.

HOLDEN, M. A., NEEDHAM, D. & BAYLEY, H. (2007). Functional bio-networks from nanoliter water droplets. Journal of the American Chemical Society, 129, 8650-8655.

HWANG, W. L. (2006). Design automation and test techniques for microfluidic biochips, Duke University.

HWANG, W. L., CHEN, M., CRONIN, B., HOLDEN, M. A. & BAYLEY, H. (2008). Asymmetric droplet interface bilayers. Journal of the American Chemical Society, 130(18), 5878-5879.

HWANG, W. L., HOLDEN, M. A., WHITE, S. & BAYLEY, H. (2007). Electrical behavior of droplet interface bilayer networks: experimental analysis and modeling. Journal of the American Chemical Society, 129, 11854-11864.

HWANG, W. L., SU, F. & CHAKRABARTY, K. (2006). Automated design of pin-constrained digital microfluidic arrays for lab-on-a-chip applications. In IEEE Design Automation Conference, pp. 925-930. ACM, San Francisco, California.

KATAGIRI, K., HASHIZUME, M., KIKUCHI, J., TAKETANI, Y. & MURAKAMI, M. (2004). Creation of asymmetric bilayer membrane on monodispersed colloidal silica particles. Colloids and Surfaces B-Biointerfaces, 38(3-4), 149-153.

KLEBER, A. G. & RUDY, Y. (2004). Basic mechanisms of cardiac impulse propagation and associated arrhythmias. Physiological Reviews, 84(2), 431-488.

KOL, M. A., DE KROON, A., KILLIAN, J. A. & DE KRUIJFF, B. (2004). Transbilayer movement of phospholipids in biogenic membranes. Biochemistry, 43(10), 2673-2681.

KOL, M. A., DE KROON, A., RIJKERS, D. T. S., KILLIAN, J. A. & DE KRUIJFF, B. (2002). The transmembrane domains of membrane-spanning proteins induce phospholipid flop. Biophysical Journal, 82(1), 147A-147A.

KRASILNIKOV, O. V., CAPISTRANO, M. F. P., YULDASHEVA, L. N. & NOGUEIRA, R. A. (1997). Influence of Cys-130 S-aureus alpha-toxin on planar lipid bilayer and erythrocyte membranes. Journal of Membrane Biology, 156(2), 157-172.

LEE, P. J., HUNG, P. J., SHAW, R., JAN, L. & LEE, L. P. (2005). Microfluidic application-specific integrated device for monitoring direct cell-cell communication via gap junctions between individual cell pairs. Applied Physics Letters, 86(22).

LIANG, B. & TAMM, L. K. (2007). Structure of outer membrane protein G by solution NMR spectroscopy. Proceedings of the National Academy of Sciences of the United States of America, 104, 16140-16145.

LIU, J. & CONBOY, J. C. (2005). 1,2-diacyl-phosphatidylcholine flip-flop measured directly by sum-frequency vibrational spectroscopy. Biophysical Journal, 89(4), 2522-2532.

LUISI, P. L., FERRI, F. & STANO, P. (2006). Approaches to semi-synthetic minimal cells: a review. Naturwissenschaften, 93(1), 1-13.

LUO, T. J. M., SOONG, R., LAN, E., DUNN, B. & MONTEMAGNO, C. (2005). Photo-induced proton gradients and ATP biosynthesis produced by vesicles encapsulated in a silica matrix. Nature Materials, 4(3), 220-224.

MARGULIES, D., FELDER, C. E., MELMAN, G. & SHANZER, A. (2007). A molecular keypad lock: A photochemical device capable of authorizing password entries. Journal of the American Chemical Society, 129(2), 347-354.

MARGULIES, D., MELMAN, G. & SHANZER, A. (2006). A molecular full-adder and full-subtractor, an additional step toward a moleculator. Journal of the American Chemical Society, 128(14), 4865-4871.

MCINTYRE, J. C. & SLEIGHT, R. G. (1991). Fluorescence assay for phospholipid membrane asymmetry. Biochemistry, 30(51), 11819-11827.

MILES, G., CHELEY, S., BRAHA, O. & BAYLEY, H. (2001). The staphylococcal leukocidin bicomponent toxin forms large ionic channels. Biochemistry, 40(29), 8514-8522.

MILLER, C., ed. (1986). Ion Channel Reconstitution. New York: Plenum Press.

MONTAL, M. & MUELLER, P. (1972). Formation of bimolecular membranes from lipid monolayers and a study of their electrical properties. Proceedings of the National Academy of Sciences of the United States of America, 69(12), 3561-3566.

MULLER, D. A., SORSCH, T., MOCCIO, S., BAUMANN, F. H., EVANS-LUTTERODT, K. & TIMP, G. (1999). The electronic structure at the atomic scale of ultrathin gate oxides. Nature, 399(6738), 758-761.

MULLER, D. J., HAND, G. M., ENGEL, A. & SOSINSKY, G. E. (2002). Conformational changes in surface structures of isolated connexin 26 gap junctions. Embo Journal, 21(14), 3598-3607.

MUSTERS, R. J. P., OTTEN, E., BIEGELMANN, E., BIJVELT, J., KEIJZER, J. J. H., POST, J. A., DENKAMP, J. & VERKLEIJ, A. J. (1993). Loss of asymmetric distribution of sarcolemmal phosphatidylethanolamine during simulated ischemia in the isolated neonatal rat cardiomyocyte. Circulation Research, 73(3), 514-523.

NOIREAUX, V., BAR-ZIV, R., GODEFROY, J., SALMAN, H. & LIBCHABER, A. (2005). Toward an artificial cell based on gene expression in vesicles. Physical Biology, 2(3), P1-P8.

NOLAN, J. P., MAGARGEE, S. F., POSNER, R. G. & HAMMERSTEDT, R. H. (1995). Flow cytometric analysis of transmembrane phospholipid movement in bull sperm. Biochemistry, 34(12), 3907-3915.

OPDENKAMP, J. A. F. (1979). Lipid asymmetry in membranes. Annual Review of Biochemistry, 48, 47-71.

PAUTOT, S., FRISKEN, B. J. & WEITZ, D. A. (2003). Engineering asymmetric vesicles. Proceedings of the National Academy of Sciences of the United States of America, 100(19), 10718-10721.

PERACCHIA, C., ed. (2000). Gap junctions: molecular basis of cell communication in health and disease. San Diego: Academic Press.

PIDDOCK, L. J. V. (2006). Multidrug-resistance efflux pumps - not just for resistance. Nature Reviews Microbiology, 4(8), 629-636.

PIETRINI, A. V. & LUISI, P. L. (2004). Cell-free protein synthesis through solubilisate exchange in water/oil emulsion compartments. Chembiochem, 5(8), 1055-1062.

POLLACK, M. G., FAIR, R. B. & SHENDEROV, A. D. (2000). Electrowetting-based actuation of liquid droplets for microfluidic applications. Applied Physics Letters, 77(11), 1725-1726.

POLLACK, M. G., SHENDEROV, A. D. & FAIR, R. B. (2002). Electrowetting-based actuation of droplets for integrated microfluidics. Lab on a Chip, 2, 96-101.

POMORSKI, T., HRAFNSDOTTIR, S., DEVAUX, P. F. & VAN MEER, G. (2001). Lipid distribution and transport across cellular membranes. Seminars in Cell & Developmental Biology, 12(2), 139-148.

POMORSKI, T. & MENON, A. K. (2006). Lipid flippases and their biological functions. Cellular and Molecular Life Sciences, 63(24), 2908-2921.

PONSIOEN, B., VAN ZEIJL, L., MOOLENAAR, W. H. & JALINK, K. (2007). Direct measurement of cyclic AMP diffusion and signaling through connexin43 gap junctional channels. Experimental Cell Research, 313(2), 415-423.

POST, J. A., CLAGUE, J. R. & LANGER, G. A. (1993). Sarcolemmal phospholipid asymmetry and Ca fluxes on metabolic inhibition of neonatal rat heart cells. American Journal of Physiology, 265(2), H461-H468.

SANGUINETTI, M. C. & TRISTANI-FIROUZI, M. (2006). hERG potassium channels and cardiac arrhythmia. Nature, 440(7083), 463-469.

SATO, H. & FELIX, J. B. (2006). Peptide-membrane interactions and mechanisms of membrane destruction by amphipathic alpha-helical antimicrobial peptides. Biochimica Et Biophysica Acta-Biomembranes, 1758(9), 1245-1256.

SCHROIT, A. J., MADSEN, J. W. & TANAKA, Y. (1985). In vivo recognition and clearance of red blood cells containing phosphatidylserine in their plasma membranes. Journal of Biological Chemistry, 260(8), 5131-5138.

SEVERS, N. J., DUPONT, E., COPPEN, S., HALLIDAY, D., INETT, E., BAYLIS, D. & ROTHERY, S. (2004). Remodelling of gap junctions and connexin expression in heart disease. Biochimica Et Biophysica Acta-Biomembranes, 1662(1-2), 138-148.

SHERWOOD, D. & MONTAL, M. (1975). TRANSMEMBRANE LIPID MIGRATION IN PLANAR ASYMMETRIC BILAYER MEMBRANES. Biophysical Journal, 15(5), 417-434.

SONG, L. Z., HOBAUGH, M. R., SHUSTAK, C., CHELEY, S., BAYLEY, H. & GOUAUX, J. E. (1996). Structure of staphylococcal alpha-hemolysin, a heptameric transmembrane pore. Science, 274(5294), 1859-1866.

STRACK, G., ORNATSKA, M., PITA, M. & KATZ, E. (2008). Biocomputing security system: Concatenated enzyme-based logic gates operating as a biomolecular keypad lock. Journal of the American Chemical Society, 130(13), 4234-+.

SU, F., HWANG, W. L., MUKHERJEE, A. & CHAKRABARTY, K. (2007). Testing and diagnosis of realistic defects in digital microfluidic biochips. Journal of Electronic Testing, 23, 219-233.

SUBBARAO, G. V. & VAN DEN BERG, B. (2006). Crystal structure of the monomeric porin OmpG. Journal of Molecular Biology, 360(4), 750-759.

SYEDA, R., HOLDEN, M. A., HWANG, W. L. & BAYLEY, H. (2008). Rapid screening of blockers against ion channels expressed in droplet interface bilayers. In prep.

TAYLOR, A. F., SAUNDERS, M. M., SHINGLE, D. L., CIMBALA, J. M., ZHOU, Z. & DONAHUE, H. J. (2007). Mechanically stimulated osteocytes regulate osteoblastic activity via gap junctions. American Journal of Physiology-Cell Physiology, 292(1), C545-C552.

UTSUGI, T., SCHROIT, A. J., CONNOR, J., BUCANA, C. D. & FIDLER, I. J. (1991). Elevated expression of phosphatidylserine in the outer membrane leaflet of human tumor cells and recognition by activated human blood monocytes. Cancer Research, 51(11), 3062-3066.

VALEVA, A., WALEV, I., PINKERNELL, M., WALKER, B., BAYLEY, H., PALMER, M. & BHAKDI, S. (1997). Transmembrane beta-barrel of staphylococcal alpha-toxin forms in sensitive but not in resistant cells. Proceedings of the National Academy of Sciences of the United States of America, 94(21), 11607-11611.

VEHRING, S., PAKKIRI, L., SCHROER, A., ALDER-BAERENS, N., HERRMANN, A., MENON, A. K. & POMORSKI, T. (2007). Flip-flop of fluorescently labeled phospholipids in proteoliposomes reconstituted with Saccharomyces cerevisiae microsomal proteins. Eukaryotic Cell, 6(9), 1625-1634.

VERKLEIJ, A. J. & POST, J. A. (2000). Membrane phospholipid asymmetry and signal transduction. Journal of Membrane Biology, 178(1), 1-10.

WACKLIN, H. P. & THOMAS, R. K. (2007). Spontaneous formation of asymmetric lipid bilayers by adsorption of vesicles. Langmuir, 23(14), 7644-7651.

WADE, M. H., TROSKO, J. E. & SCHINDLER, M. (1986). A fluorescence photobleaching assay of gap junction-mediated communication between human cells. Science, 232(4749), 525-528.

WHITE, S. H. (1972). Analysis of the torus surrounding planar lipid bilayer membranes. Biophysical Journal, 12(4), 432-445.

WIESE, A., REINERS, J. O., BRANDENBURG, K., KAWAHARA, K., ZAHRINGER, U. & SEYDEL, U. (1996). Planar asymmetric lipid bilayers of glycosphingolipid or lipopolysaccharide on one side and phospholipids on the other: Membrane potential, porin function, and complement activation. Biophysical Journal, 70(1), 321-329.

WU, H. C., ASTIER, Y., MAGLIA, G., MIKHAILOVA, E. & BAYLEY, H. (2007). Protein nanopores with covalently attached molecular adapters. Journal of the American Chemical Society, 129(51), 16142-16148.

XU, T., HWANG, W. L., SU, F. & CHAKRABARTY, K. (2007). Automated design of pin-constrained digital microfluidic biochips under droplet-interference constraints. Journal on Emerging Technologies in Computing Systems, 3(3), Article 14.

YILDIZ, O., VINOTHKUMAR, K. R., GOSWAMI, P. & KUHLBRANDT, W. (2006). Structure of the monomeric outer-membrane porin OmpG in the open and closed conformation (vol 25, pg 3702, 2006). Embo Journal, 25(21), 5240-5240.

YURKE, B., TURBERFIELD, A. J., MILLS, A. P., SIMMEL, F. C. & NEUMANN, J. L. (2000). A DNA-fuelled molecular machine made of DNA. Nature, 406(6796), 605-608.

ZEILINGER, C., STEFFENS, M. & KOLB, H. A. (2005). Length of C-terminus of rCx46 influences oligomerization and hemichannel properties. Biochimica Et Biophysica Acta-Biomembranes, 1720(1-2), 35-43.

ZHAO, H. B., KIKUCHI, T., NGEZAHAYO, A. & WHITE, T. W. (2006). Gap junctions and cochlear homeostasis. Journal of Membrane Biology, 209(2-3), 177-186.

ZWAAL, R. F. A., COMFURIUS, P. & BEVERS, E. M. (2005). Surface exposure of phosphatidylserine in pathological cells. Cellular and Molecular Life Sciences, 62(9), 971-988.